Technical Physics Letters, Vol. 30, No. 10, 2004, pp. 799–801. Translated from Pis'ma v Zhurnal Tekhnicheskoĭ Fiziki, Vol. 30, No. 19, 2004, pp. 1–6.

The Effect of Hydrogen on Crystallization of a $Ti_{50}Ni_{25}Cu_{25}$ Amorphous Alloy

L. V. Spivak[a,*], N. E. Skryabina[a], D. Fruchard[b], and A. V. Shelyakov[c]

[a] *Perm State University, Perm, Russia*

[b] *Laboratoire de Crystallographie, CNRS, BP 166, 38042 Grenoble, Cedex 09, France*

[c] *Moscow Physical Engineering Institute (State Technical University), Moscow, Russia*

** e-mail: levspivak@permonline.ru*

Received March 18, 2004

Abstract—Two effects not reported previously for the interaction of hydrogen with amorphous metal alloys were observed in a $Ti_{50}Ni_{25}Cu_{25}$ alloy: (i) hydrogen-induced increase in the crystallization temperature and (ii) suppression of the reverse martensitic transition B19 ⟶ B2 in the alloy samples hydrogenated upon crystallization. © *2004 MAIK "Nauka/Interperiodica".*

Introduction. Previously [1], we reported on a significant decrease in the shear modulus and an increase in the electric resistance of a $Ti_{50}Ni_{25}Cu_{25}$ amorphous alloy observed immediately in the course of hydrogenation. These results gave us grounds to expect that hydrogen might also influence the other basic properties of amorphous alloys, in particular, the temperature of the transition from amorphous to crystalline state. The observation of such phenomena must be facilitated by the fact that nickel titanium alloys, in particular, amorphous quasibinary alloys of the TiNi–TiCu system, are characterized by a rather high coefficient of hydrogen diffusion (~10^{11} m^2/s) and a large hydrogen sorption capacity (much greater than that of iron-based amorphous alloys). Moreover, nickel titanium alloys are capable of retaining hydrogen for a sufficiently long time at 300 K, while complete elimination of hydrogen from these alloys is observed only on heating above 900–1000 K [2].

Experimental. The experiments were performed with the samples of rapidly quenched $Ti_{50}Ni_{25}Cu_{25}$ alloy ribbons with a thickness of about 40 μm, obtained by melt spinning at a cooling rate of ~10^6 K/s. The results of X-ray diffraction measurements [3–5] confirmed that all samples in the initial (as-quenched) state possessed a fully amorphous structure.

The samples were hydrogenated as cathodes in a temperature-controlled electrochemical cell with a platinum wire anode. The process was conducted in an H_2SO_4 based electrolyte at a cathode current density of 50 A/m^2.

The samples were studied by differential thermal analysis (DTA) in a high-sensitivity Perkin-Elmer Model 404 S/3/F calorimeter. The DTA measurements were performed in an argon atmosphere at a heating rate of 20 K/s. The magnetic properties of the samples were studied on heating in vacuum using a BALMAG measuring system operating at a heating rate of 5 K /s.

The X-ray diffraction measurements were performed on Siemens D5000 and Bruker D8 ADVANCE diffractometers using monochromated Cu$K\alpha_1$ radiation. The sample surface topography was studied with a Jeol JSM-5600LV scanning electron microscope (SEM).

Results and discussion. Figure 1 shows the results of DTA measurements for a $Ti_{50}Ni_{25}Cu_{25}$ alloy in the initial state and upon saturation with hydrogen for various times. These curves reveal a phenomenon not reported previously in the solid state physics, whereby the crystallization temperature of an amorphous alloy

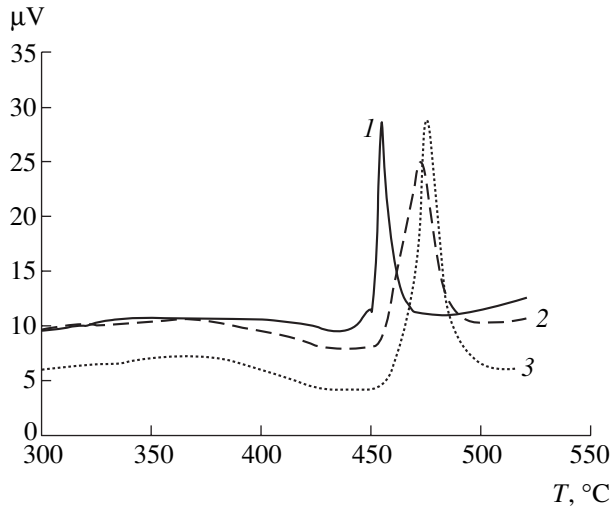

Fig. 1. DTA curves of a $Ti_{50}Ni_{25}Cu_{25}$ alloy measured (*1*) in the initial amorphous state and (*2*, *3*) upon the hydrogenation for 20 and 60 min, respectively.

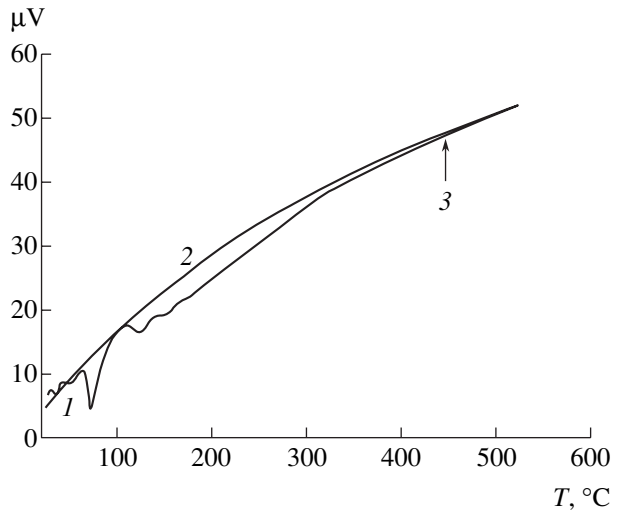

Fig. 2. DTA curves of a $Ti_{50}Ni_{25}Cu_{25}$ alloy observed in the course of repeated measurement of the samples preliminary heated above the crystallization temperature: (*1*) before hydrogenation; (*2*) after hydrogenation for 20 min. Arrow *3* indicates the position of the exothermal peak of crystallization observed during the first heating.

increases upon its saturation with hydrogen. As can be seen, the exothermal peak reflecting the transition from amorphous to crystalline state shifts toward higher temperatures. The introduction of hydrogen influences both the width of the crystallization peak (crystallization temperature interval) and the relative intensity of this peak. For all hydrogen saturation times studied, heating of the samples revealed enhanced endothermal processes in the X-ray-amorphous matrix prior to the exothermal peak. Analogous patterns were observed during hydrogen saturation and subsequent heating of the same alloy in an amorphous-crystalline state. Another peculiarity in crystallization of the amorphous alloy preliminarily saturated with hydrogen is that the onset of the exothermal process of crystallization is observed at a temperature close to that of the exothermal peak in the DTA curve of the initial (nonhydrogenated) sample. This may be evidence of the presence of local regions with different amorphous structures formed as a result of the phase separation in the initial, relatively homogeneous solid solution.

SEM micrographs of the surface of amorphous metal ribbons revealed a small number of crystalline formations having lateral dimensions within 300–500 μm and a clearly pronounced relief characteristic of the twinned martensite. The introduction of hydrogen under specified saturation conditions did not lead to an increase in the number and morphology of such precipitates.

The X-ray diffraction investigation gave usual results (see, e.g., [6]) showing that the hydrogenated material remained X-ray amorphous. The saturation with hydrogen only leads to a decrease in intensity of the main halo (at $2\Theta \approx 41°$) and in the general background level. The latter can be considered as evidence of the onset of phase separation in the solid solution and the appearance of the short-range order of a different type. This observation is consistent with our DTA results and the data on a hydrogen-induced decrease in the free volume of the amorphous alloy matrix [7].

Since the process of crystallization in amorphous alloys of the metal–metal type, as well as the processes preceding this transition, are studied to a much lower extent than the analogous phenomena in amorphous alloys of the metal–metalloid type, we can only make some general assumptions concerning the nature of the observed effects. In contrast to the case of iron-based amorphous alloys, hydrogen introduced into alloys based on the intermetallic compound TiNi is retained in the matrix even upon heating above 600°C. Therefore, we may suggest that hydrogen behaves in the latter case as a very strong amorphizing agent and shifts the alloy transition from amorphous to crystalline state toward higher temperatures. Evidence of this transition occurring on heating to a temperature above that of the exothermal peak is provided (i) by the X-ray data indicative of the appearance of a short-range order, (ii) by the appearance of new crystalline phases, and (iii) by the absence of any endothermal and exothermal peaks in the region of 520°C on the DTA curves measured in the course of repeated heating (Fig. 2).

A comparison of the DTA curves obtained in the course of repeated heating of the hydrogenated and nonhydrogenated alloy (Fig. 2) reveals another unusual phenomenon: repeatedly heated hydrogenated samples exhibit no endothermicity related to the reverse martensitic transition B19 $\longrightarrow$ B2. The structural state not susceptible to the reverse martensitic transition in this temperature interval is retained in the alloy repeatedly heated to a temperature of up to 700°C. This observation reveals a new aspect of the effect of hydrogenation on the phase transitions in the alloy upon crystallization. Indeed, in alloys obtained by the standard technology and featuring the shape memory effect, hydrogen only changes the intensity and order of the forward and reverse martensitic transitions [2, 6].

In contrast, we have observed suppression or, more probably, a significant shift of the interval of martensitic transition toward lower temperatures. It should be noted that the X-ray diffraction pattern of the alloy heated above the crystallization temperature is also somewhat different for the previously hydrogenated and nonhydrogenated samples with respect to both the intensity of reflections and the relative positions of some lines. At the same time, the results of magnetic measurements did not reveal any peculiarities for the samples heated in the indicated temperature interval. The magnetization significantly decreases on heating to ~200°C and rather slightly depends on the temperature above 360°C. This temperature is close to the Curie point of pure nickel, which suggests that nickel imparts

weak ferromagnetic properties to the alloy. The effect of hydrogen on this characteristic is undetermined.

Conclusions. We have observed two previously unreported physical phenomena caused by the introduction of hydrogen into a rapidly quenched amorphous alloy $Ti_{50}Ni_{25}Cu_{25}$ of the TiNi–TiCu system: (i) hydrogen-induced shift of the temperature of transition from amorphous to crystalline state and (ii) suppression of the reverse martensitic transition in the alloy samples hydrogenated upon crystallization.

Acknowledgments. The authors gratefully acknowledge support from the Russian Foundation for Basic Research, project no. 03-02-16561.

REFERENCES

1. N. E. Skryabina, L. V. Spivak, and A. V. Shelyakov, Pis'ma Zh. Tekh. Fiz. **30** (7), 27 (2004) [Tech. Phys. Lett. **30**, 270 (2004)].
2. L. V. Spivak, N. E. Skryabina, and V. N. Khachin, Fiz. Met. Metalloved. **79** (4), 138 (1995).
3. A. V. Shelyakov, N. M. Matveeva, and S. G. Larin, in *Fundamentals, Modeling and Industrial Applications*, Ed. by F. Trochu, V. Brailovski, and A. Galibois (Can. Inst. Mining, Metallurgy and Petroleum, 1999), pp. 295–303.
4. H. Rösner, P. Schlossmacher, A. V. Shelyakov, *et al.*, Acta Mater. **49**, 1541 (2001).
5. P. L. Potapov, A. V. Shelyakov, and D. Schryvers, Scr. Mater. **44**, 1 (2001).
6. N. E. Skryabina and L. V. Spivak, Izv. Ross. Akad. Nauk, Ser. Fiz. **67**, 1411 (2003).
7. N. Skryabina and L. Spivak, J. Alloys Compd. **356–357**, 630 (2003).

Translated by P. Pozdeev

Technical Physics Letters, Vol. 30, No. 10, 2004, pp. 802–803. Translated from Pis'ma v Zhurnal Tekhnicheskoĭ Fiziki, Vol. 30, No. 19, 2004, pp. 7–11.

The N3 Center Luminescence Quenched by Nitrogen Impurity in Natural Diamond

E. A. Vasil'ev*, V. I. Ivanov-Omskii, B. S. Pomazanskii, and I. N. Bogush

Yakutian Central Research and Geological Exploration Institute, ALROSA Joint-Stock Company, Mirnyĭ, Sakha Republic, 678170 Russia

Ioffe Physicotechnical Institute, Russian Academy of Sciences, St. Petersburg, 194021 Russia

** e-mail: vasilyev@cnigri.alrosa-mir.ru*

Received March 22, 2004

Abstract—N3 center luminescence quenching by the main types of defects (A and B1) related to nitrogen impurity in natural diamond was studied by monitoring the luminescence yield and using the Raman scattering intensity as a measure of the exciting radiation intensity. The luminescence yield from the N3 centers decreases by a factor of about 3000 when the concentration of nitrogen in the form of type A and B1 defects in natural diamond increases from 0.008 to 0.1 at. %. © *2004 MAIK "Nauka/Interperiodica".*

Previously, it was demonstrated that nitrogen impurity in the form of type A defects in natural diamond influences the intensity decay time and the halfwidth of the phononless lines of luminescence from N3 [1–3], H3 [4], and GR1 [5] type centers, although no quantitative experimental data on the luminescence quenching were reported for these centers. In the cited papers, it was assumed that luminescence quenching is related to dipole–quadrupole interaction. According to this model, the luminescence yield exhibits exponential dependence on the concentration of type A defects [4]. At the same time, it was reported [6] that the N3 center luminescence depends on the relative content of defects of the A, B1 and B2 types, rather than on their concentration.

In this context, we have studied the N3 center luminescence quenching by type A and B1 defects in natural diamond at room temperature.

Recently [7], it was established that the structure of type A defects can be modeled by two substitutional nitrogen atoms; the N3 center, by three substitutional nitrogen atoms and a vacancy; and a probable model structure of type B1 defects comprises four nitrogen atoms and a vacancy. A structural model of type B2 defects with dimensions ranging from several nanometers to several dozens of microns has not yet been unambiguously established. According to [7], these defects probably appear as interstitial carbon atoms accumulated in {100} planes, and the data of electron energy loss spectroscopy (EELS) indicate that nitrogen accounts for 6–60% of the total number of atoms in such defects [7]. No data on the spatial correlation between N3 centers and B2 defects were reported and, taking into account the large size of B2 defects, we may assume that their interaction with N3 centers is insignificant. Anyhow, we may assume that the contribution to this interaction is proportional to the total concentration of nitrogen in defects of the A and B1 types.

In determining the luminescence yield, we have used the intensity of Raman scattering as a measure of the exciting radiation intensity. The first-order Raman scattering from diamond is characterized by a frequency shift of 1332 cm^{-1} and a cross section of $\sigma = 6.5 \times 10^{-5}$ m^{-1} sr^{-1} [8]. The measurements were performed on a series of 42 natural diamonds of Ia type, having an octahedral shape with dimensions from 2 to 6 mm. All samples exhibited a homogeneous internal structure during luminescence observation in a binocular microscope. The concentration of the N3 centers was determined from the coefficient of absorption of a phononless line at 415.2 nm measured using a spectrometer based on an MDR-41 monochromator. The photoluminescence spectra with a Raman scattering line were measured at room temperature in the 345–600 nm wavelength range using a computer-controlled DMR-4 double-prism monochromator, an LGI-505 nitrogen laser as the excitation source, and a FEU-106 photomultiplier as the detector. The spectra were not corrected for the inhomogeneous spectral sensitivity of a photodetector and for the nonlinear dispersion of the monochromator. The Raman line was characterized only by the peak intensity; no evidence of induced Raman scattering was observed. The concentration of nitrogen in the form of type A and B1 defects was determined using absorption spectra measured in the 400–4000 cm^{-1} range on an FSM-1201 Fourier-transform IR spectrometer and the calibration data taken from [9–11].

The intensity of luminescence at the maximum of the phononless line of the N3 centers at 415.2 nm was normalized to the Raman line intensity. The ratio of the normalized intensity to the absorption coefficient was assumed to be proportional to the luminescence yield from the N3 centers. Depending on the sample orientation, the luminescence signal intensity exhibited ten-

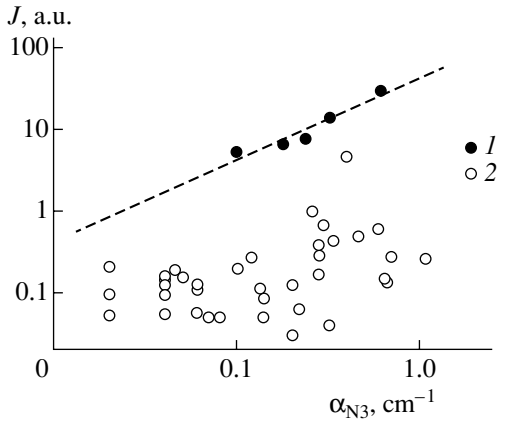

Fig. 1. A semilogarithmic plot of the normalized luminescence intensity versus absorption coefficient of the N3 centers (α_{N3}) for diamond crystals of the first group (*1*) and second group (*2*). Dashed line shows a linear approximation for the first group.

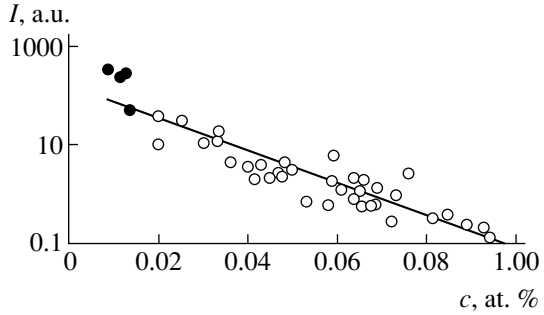

Fig. 2. A semilogarithmic plot of the luminescence yield from the N3 centers versus the total concentration of nitrogen *c* in the form of defects of both A and B1 types. Black and open symbols correspond to diamond crystals of the same two groups as in Fig. 1.

fold variation, while changes in the values normalized to the Raman line intensity did not exceed 10%. On the passage from one sample to another, the scatter of normalized intensities reached three orders of magnitude.

Figure 1 shows a semilogarithmic plot of the normalized luminescence intensity versus absorption coefficient of the N3 centers (α_{N3}). As can be seen from these data, the crystals can be conditionally divided into two groups. In the first group, the intensity of luminescence increases with the concentration of N3 centers; in the second group, the luminescence intensity is much lower and rather weakly depends on the concentration.

Figure 2 presents a semilogarithmic plot of the luminescence yield from the N3 centers versus the total concentration of nitrogen in the form of defects of both A and B1 types. These experimental results are well approximated by exponential dependence, which confirms the quenching action of impurity nitrogen [4] and provides a quantitative description of the luminescence quenching. Individual plots of the luminescence yield versus the concentration of nitrogen in the form of type A and type B1 defects exhibit a much greater scatter of experimental points and show that the ratios of A/B1 and A/B2 (determined as the ratio of the corresponding absorption coefficients) do not influence the luminescence yield.

Thus, the intensity of the phononless line of luminescence from the N3 centers, normalized to the Raman line intensity and divided by the concentration of N3 centers, may serve a measure of the total luminescence quenching in a given diamond crystal and can be used to decrease the influence of geometric factors on the experimental results. The luminescence is quenched not only by the defects of the A and B1 types: as the total concentration of these defects increases from 0.008 to 9.1 at. %, the luminescence yield from the N3 centers decreases by a factor of about 3000. Apparently, the obtained results are generally typical of the quenching of luminescence from centers featuring analogous behavior of the phononless lines and the luminescence kinetics depending on the nitrogen concentration, such as H3, H4 [3], and GR1 [5].

The possibilities of using diamond as an active element in laser technology is by no means completely exhausted even with respect to the N3 and H3 type centers. Very strong deactivation of the excited states by nitrogen impurity reduces the real gain on these centers and increases the lasing threshold, which probably explains the results obtained in [12]. Good prospects are offered by diamond crystals with a high content of N3 and H3 centers and a low concentration of nitrogen impurity.

REFERENCES

1. Z. V. Bartoshinskiĭ, S. N. Bekesha, V. V. Vasil'ev, *et al.*, Mineral. Zh. **12** (6), 85 (1990).
2. E. V. Sobolev and O. P. Yur'eva, Sverkhtverd. Mater., No. 2, 3 (1990).
3. M. F. Thomaz and G. Davies, Proc. R. Soc. London, Ser. A **362**, 405 (1978).
4. M. D. Crossfield, G. Davies, A. T. Collins, *et al.*, J. Phys. C **7**, 1909 (1974).
5. G. Davies, M. F. Thomaz, M. H. Nazare, *et al.*, J. Phys. C **20**, L13 (1987).
6. S. P. Plotnikova, in *Diamonds in Electronic Engineering* (Énergoatomizdat, Moscow, 1990), pp. 156–170 [in Russian].
7. J. P. Goss, B. J. Coomer, R. Jones, *et al.*, Phys. Rev. B **67**, 165208 (2003).
8. *Light Scattering in Solids*, Vol. 2: *Basic Concepts and Instrumentation*, Ed. by M. Cardona and G. Guntherodt (Springer, Heidelberg, 1982).
9. S. R. Boyd, I. Kiflawi, and G. S. Woods, Philos. Mag. B **69**, 1149 (1994).
10. S. R. Boyd, I. Kiflawi, and G. S. Woods, Philos. Mag. B **72**, 351 (1995).
11. G. S. Woods, Proc. R. Soc. London, Ser. A **407**, 219 (1986).
12. V. P. Mironov, Candidate's Dissertation (Irkutsk, 1995).

Translated by P. Pozdeev

Technical Physics Letters, Vol. 30, No. 10, 2004, pp. 804–805. Translated from Pis'ma v Zhurnal Tekhnicheskoĭ Fiziki, Vol. 30, No. 19, 2004, pp. 12–16.

Determination of the Hardness of Materials Featuring Phase Transitions

T. Yu. Sablina, A. G. Mel'nikov, and S. N. Kul'kov*

Institute of Strength Physics and Materials Science, Siberian Division, Russian Academy of Sciences, Tomsk, 634055 Russia

** e-mail: kulkov@ms.tsc.ru*

Received January 19, 2004; in final form, April 26, 2004

Abstract—The dependence of the Vickers hardness (*HV*) on the indenter load has been studied in a series of materials capable of featuring phase transitions under applied stress. The *HV* value in such materials increases with the load as a result of the phase transition. © *2004 MAIK "Nauka/Interperiodica".*

Hardness measurements offer the simplest, rapid, and highly sensitive means of testing the mechanical properties of materials [1]. These measurements are nondestructive, can be implemented using simple standard equipment, and provide information not only about hardness, but also about some other characteristics such as the fracture toughness and the Young modulus [2].

Hardness testing using indenters of various types in a broad range of loads revealed the so-called size effect of indentation, whereby the obtained hardness value depends on the load applied to the indenter [3, 4]. This phenomenon is especially clearly pronounced in the case of microindentation, where the value of microhardness sharply increases with decreasing load [5]. This effect is very important in the case of materials capable of featuring phase transitions during load application. In such materials, one can expect pronounced manifestations of the dependence of hardness and cracking resistance on the load applied to the indenter.

In this context, we have studied the effect of indenter load on the value of hardness in materials capable of featuring phase transitions under the action of applied stress.

The experiments were performed with the following ceramics and intermetallic compounds: 95 wt % ZrO_2 + 5 wt % Y_2O_3 (Z0) ceramics with the grain size 4.5, 2.2, and 0.6 μm; 80 wt % ZrO_2(Y) + 20 wt % Al_2O_3 (20A) ceramics; Al_2O_3 ceramics (A); nickel titanium alloys 50 at. % Ni + 50 at. % Ti (NiTi-1) and 50.5 at. % Ni + 49.5 at. % Ti (NiTi-2) in metastable and stable states, respectively. The reference sample was made of steel according to the State Standard GOST 9031–75 (Hardness Measure Standard MTR-1: Steel). The samples were ground on a diamond disk and then polished with diamond pastes of various grain size so as to remove the grinding effects. The hardness tests were performed using a Vickers hardness meter. The indenter load was varied from 10 to 150 N, with a 10-N step in the interval from 10 to 50 N and with a 50-N step from 50 to 150 N; five indentations were made at each load.

Figure 1 shows plots of the Vickers hardness (*HV*) versus the indenter load (*P*) for the materials studied. As can be seen from Fig. 1a, the hardness is independent of the applied load for the steel reference and for the samples of alumina (A), fine-grained (0.6 μm)

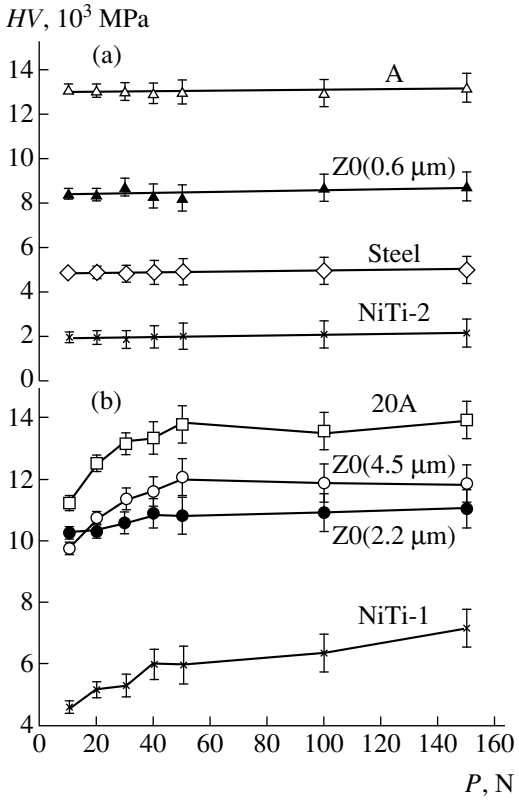

Fig. 1. Plots of the Vickers hardness versus indenter load for the materials (a) not exhibiting phase transitions and (b) exhibiting phase transitions under applied stress.

1063-7850/04/3010-0804$26.00 © 2004 MAIK "Nauka/Interperiodica"

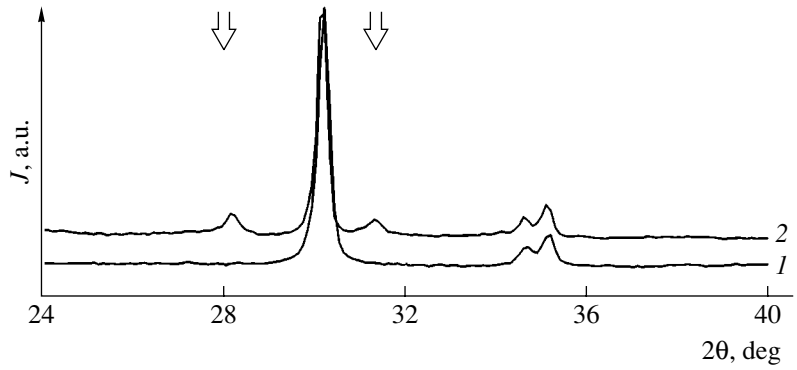

Fig. 2. X-ray diffraction patterns of Z0 ceramics (*1*) before indentation and (*2*) after repeated indentation at $P = 100$ N. Arrows indicate the peaks of a monoclinic phase.

ZrO_2-based ceramics (Z0), and stable nickel titanium alloy (NiTi-2). In contrast, Fig. 1b shows the plots of *HV* versus load for the materials where the hardness depends on the applied load. In the nickel titanium alloy NiTi-1 capable of martensitic transition under load, the *HV* value increases with *P.* In the ZrO_2-based ceramics (Z0) with medium and large grain size (2.2 and 4.5 μm) and with alumina additives (20A), the hardness increases with the load up to about 50 N and then remains approximately constant (Fig. 1b).

The observed growth in the *HV* of ceramics with increasing *P* in the region of small indenter loads is anomalous [3, 4]. The unusual behavior is most probably related to the phase transition under load taking place in the materials tested. Indeed, it is known [6] that peculiarities in the deformation and fracture of zirconia-based ceramics in the zone of Vickers indentation may lead to a transition from tetragonal to monoclinic phase under the action of stresses developed in the material.

In order to confirm that indentation is accompanied by the phase transition, we have studied the X-ray diffraction patterns from the surface of Z0 ceramics before and after multiply repeated indentation at a 100-N load. Figure 2 shows the fragments of X-ray diffraction patterns obtained before and after indentation, which reveal the presence of a monoclinic phase. The quantitative phase analysis performed using CuK_α radiation according to [7] showed that the content of this phase is $6 \pm 1\%$. This agrees with the area of deformed surface in the region of indentation, which amounts to approximately 5–7% of the total sample surface area. Since the X-ray data are obtained from a rather thin surface layer (the depth of penetration of the CuK_α radiation is about 100 μm), we can assume that the deformed sample surface area in the region of indentation corresponds to the volume of material converted into the monoclinic state. The observed saturation in the dependence of hardness on the indenter load is explained by the existence of a critical load *P* above which the resource of the phase transition is exhausted.

Thus, in determining the hardness of materials capable of featuring phase transitions under applied stress, it is necessary to take into account the load applied to the indenter of a testing device.

REFERENCES

1. V. K. Grigorovich, *Hardness and Microhardness of Metals* (Nauka, Moscow, 1976) [in Russian].
2. L. M. Keer, Th. N. Farris, and J. Ch. Lee, J. Am. Ceram. Soc. **69**, 392 (1986).
3. G. A. Gogotsi and V. I. Galenko, Probl. Prochn., No. 3, 104 (1997).
4. J. G. Swadenera, E. P. George, and G. M. Pharra, J. Mech. Phys. Solids **50**, 681 (2002).
5. A. Krell, J. Am. Ceram. Soc. **78**, 1417 (1995).
6. G. A. Gogotsi and E. E. Lomonova, Ogneupory Tekh. Keram., No. 6, 4 (2000).
7. R. C. Garvie and P. S. Nicholson, J. Am. Ceram. Soc. **55**, 303 (1972).

Translated by P. Pozdeev

Technical Physics Letters, Vol. 30, No. 10, 2004, pp. 806–809. Translated from Pis'ma v Zhurnal Tekhnicheskoĭ Fiziki, Vol. 30, No. 19, 2004, pp. 17–24.

Peculiarities in the Mechanism of Current Flow through an Ohmic Contact to Gallium Phosphide

T. V. Blank*, Yu. A. Goldberg, O. V. Konstantinov, V. G. Nikitin, and E. A. Posse

Ioffe Physicotechnical Institute, Russian Academy of Sciences, St. Petersburg, 194021 Russia

** e-mail: tblank@delfa.net*

Received April 9, 2004

Abstract—The temperature dependence of the electric resistance of the In–GaP ohmic contact has been studied in the range from 77 to 420 K. The resistance was measured in GaP plates of various thickness with two In ohmic contacts. The measured ohmic contact resistance increases with temperature in the interval from 230–420 K. It is suggested that the In–GaP ohmic contact is formed by metallic shunts appearing upon deposition of In atoms on dislocations and other imperfections present (with a density evaluated at $(4.5–8) \times 10^7$ cm^{-2}) in the subsurface region of the semiconductor. © *2004 MAIK "Nauka/Interperiodica".*

Introduction. The theory of electric current flow through an ohmic contact between a metal and a semiconductor has been developed for two charge transfer mechanisms: thermionic emission and tunneling [1]. According to the theory of thermionic emission, the forward current I_f varies exponentially with the applied voltage V and the temperature T as

$$I_f = I_s \exp\left(\frac{qV}{nkT} - 1\right); \quad (1)$$

$$I_s = A^* S T^2 \exp\left(\frac{-q\varphi_B}{kT}\right), \quad (2)$$

where I_s is the saturation current, q is the electron charge, n is the ideality coefficient, k is the Boltzmann constant, φ_B is the potential barrier height, S is the contact area, and A^* is the effective Richardson constant. The latter quantity is defined by the ratio

$$A^* = A\frac{m^*}{m_0}, \quad (3)$$

where $A = 120$ A/(cm^2 K^2) and m^*/m_0 is the effective mass of the majority charge carriers.

Defined as $R_c = dV/dI$ for $V \longrightarrow 0$, the contact resistance per unit area (the specific resistance) in the theory of thermionic emission is

$$R_c = \left(\frac{k}{qA^*T}\right)\exp\left(\frac{q\varphi_B}{kT}\right). \quad (4)$$

From this expression, it follows that the contact resistance decreases with temperature, the plot of R_cT versus $1/T$ in semilogarithmic coordinates must be linear, and the slope of this line characterizes the barrier height φ_B.

According to the tunneling theory [1], the contact resistance per unit area is

$$\frac{1}{R_c} = \frac{m^* q^2}{2\pi\hbar^3}\int_0^\infty \left(\frac{T(E)}{[\exp((E-\mu)/kT)]-1}\right)dE. \quad (5)$$

Here, $\hbar$ is the Planck constant, $T(E)$ is the probability for a charge carrier with the energy E to tunnel through a barrier with the height lower by dE than $q\varphi_B$, and μ is the Fermi energy in the semiconductor.

It was demonstrated [2] that

$$R_c \sim \exp\left[\left(\frac{2\sqrt{\varepsilon_{sc}\varepsilon_0 m^*}}{\hbar}\right)\left(\frac{\varphi_B}{N^{1/2}}\right)\right], \quad (6)$$

where ε_{sc} is the permittivity of the semiconductor, ε_0 is the permittivity of vacuum, and N is the uncompensated impurity concentration. In this case, the contact resistance must exponentially depend on $N^{-1/2}$ and is virtually independent of the temperature.

Based on the results of experimental investigations of the temperature and concentration dependences of the specific resistance of various metal–semiconductor ohmic contacts, it was established that the main mechanism of current flow in such contacts was as follows: thermionic emission in p-GaAs ($p = 5 \times 10^{18}$–1×10^{19} cm^{-3}) [3], p-InP [4], p-InGaAs ($p = 5 \times 10^{18}$ cm^{-3}) [5], p-GaN ($p = 1.8 \times 10^{17}$ cm^{-3}) [6], and p-AlGaN ($p =$

3×10^{18} cm^{-3}) [7]; and tunneling in *p*-GaAs ($p = 4 \times 10^{20}$ cm^{-3}) [8], *n*-GaN ($n = 10^{17}$–10^{19} cm^{-3}) [9, 10], and *p*-AlGaN ($p = 1 \times 10^{19}$ cm^{-3}) [7].

At the same time, the mechanism of current flow through the ohmic contacts to GaP was hardly studied, despite the wide use of this semiconductor in light-emitting diodes operating in the visible range [11] and in UV photodetectors [12].

This study was aimed at determining the temperature dependence of the electric resistance of the In–GaP ohmic contact and establishing the probable mechanism of current flow through this contact.

Experimental. The initial material was a Czochralski grown (100)-oriented single crystal of gallium phosphide. The electron density and mobility in this material determined from the conductivity and Hall effect measurements at 300 K were $n = (2–4) \times 10^{17}$ cm^{-3} and μ_n = 100–110 cm^2/(V s), respectively. The uncompensated (ionized) donor concentration determined by the mercury probe technique and by measuring the current–voltage characteristics of Schottky diodes was N_d = 2.5×10^{17} cm^{-3}, which agrees well with the measured *n* values.

The resistance measurements were performed on plates of lateral dimensions 2.5×2.5 mm and various thickness *d* in the range from 0.1 to 1 mm, cut from a single crystal ingot. The ohmic contacts were prepared by fusing 0.5-mm-diameter indium droplets for 5 min at 580°C into both (top and bottom) faces of each plate in a flow of purified hydrogen. The GaP plates with fused In droplets were cooled down to room temperature and then the current–voltage characteristics of these samples were measured in the temperature range from 77 to 420 K. The sample temperature in a thermostat was controlled to within 1 K.

All the samples exhibited linear current–voltage characteristics with the slope dependent on the GaP plate thickness. In order to separate contributions to the sample resistance due to the ohmic contact (R_{cont}) and the bulk semiconductor (R_{bulk}), we constructed plots of the measured resistance R_{meas} versus plate thickness *d* (Fig. 1) described by the equations

$$R_{meas} = 2R_{cont} + R_{bulk}, \quad (7)$$

$$R_{meas}S = 2R_c + \rho d. \quad (8)$$

Here, R_c is the ohmic contact resistance defined above and R_{bulk} is the bulk resistance expressed as a function of the semiconductor resistivity ρ, plate thickness *d*, and contact area *S*. Taking into account that $R_{bulk} = \rho d/S$ and $\rho = 1/(qn\mu_n)$ and using Eqs. (7) and (8), we obtain the relation

$$R_{meas}S = 2R_c + \frac{d}{qn\mu_n}, \quad (9)$$

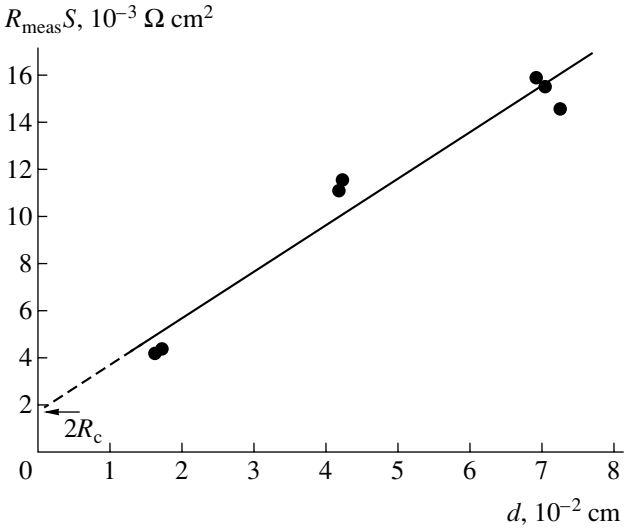

Fig. 1. Plot of the measured resistance $R_{meas}S$ versus thickness *d* of GaP plates with two ohmic contacts (In–GaP–In) at $T = 300$ K.

from which it follows that the plot of $R_{meas}S$ versus *d* has to be linear, with the ordinate intercept equal to a doubled specific contact resistance and the slope equal to the semiconductor bulk resistivity $\rho = 1/(qn\mu_n)$.

Results and discussion. Figure 1 shows the plot of $R_{meas}S$ versus *d* constructed using the results of measurements at room temperature (300 K). The experimental plot is linear and has a slope of 0.21 Ω cm, which is close to the bulk resistivity of the initial material (ρ = 0.25 Ω cm).

For all In–GaP–In samples comprising GaP plates with two ohmic contacts, the temperature dependence of R_{meas} exhibited the following behavior:

(i) At low temperatures (T = 77–125 K), the measured resistance, as well as the bulk resistivity ρ, strongly decreased with increasing temperature, which is probably explained by freezing of the impurities.

(ii) In the interval T = 125–230 K, both R_{meas} and ρ decreased with increasing temperature.

(iii) As the temperature increased from 230 to 420 K, the value of R_{meas} exhibited a growth, while ρ virtually remained constant, so that the growth was due to an increase in the ohmic contact resistance.

The specific ohmic contact resistance R_c increased in the temperature interval T = 230–420 K as depicted in Fig. 2. Since this behavior contradicts the theory of thermionic and field emission, it was suggested that the ohmic contact is determined by metallic shunts appearing upon deposition of In atoms onto imperfections (for example, dislocations) passing through a subsurface space charge region. To our knowledge, this mechanism of current flow in ohmic contacts was never considered in the literature, although the forma-

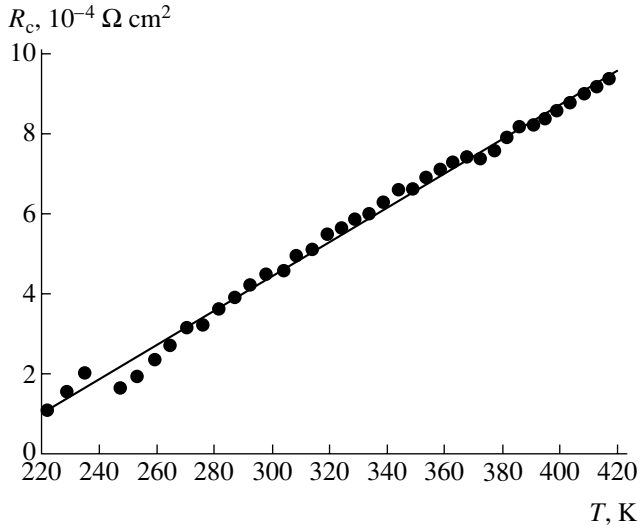

Fig. 2. Plot of the specific contact resistance R_c versus temperature T for the In–GaP ohmic contact in the temperature range T = 230–420 K.

tion of metallic shunts was observed during a study of the resistance of TiN-based epitaxial films [13]. Recently [14, 15] such shunts were assumed to contribute to the mechanism of reverse current flow in Ni–GaN Schottky diodes. The model of dislocational shunts was used to explain the temperature evolution of the current–voltage characteristics of GaP-based *p–n* junctions [16].

Let us calculate the resistance R_{shunt} of such a shunt and their number N per unit surface area. Assuming the shunt to consist of deposited In atoms (atomic radius r = 0.16 nm) and the shunt radius to be close to the GaP lattice period (a = 0.545 nm), we can express the shunt resistance as $R_{shunt} = \rho_{In}L/S$, where ρ_{In} is the resistivity of indium, L is the shunt length, and $S = \pi a^2$ is the shunt cross section area. The tabulated resistivity of indium at 0°C is $\rho_{In} = 8.2 \times 10^{-6}$ Ω cm and the temperature coefficient of resistivity is 49×10^{-4} K^{-1}. Let us take the shunt length equal to the space charge layer thickness W. At a zero bias voltage, this value is given by the formula

$$W = \sqrt{\frac{2\varepsilon_{sc}\varepsilon_0}{qN_d}\left(V_D - \frac{kT}{q}\right)}.$$

For ε_{sc} = 11.1 (the permittivity of GaP), $\varepsilon_0 = 8.85 \times 10^{-12}$ F/m, V_D = 1.1–1.2 (the diffusion potential at the In–GaP interface), and $N_d = 2.5 \times 10^{17}$ cm^{-3}, the shunt length amounts to $\sim 7 \times 10^{-6}$ cm and weakly varies in the temperature interval 230–420 K.

The results of calculations are summarized in the table. As can be seen from these data, the number density of shunts N varies rather slightly and the calculated specific contact resistance coincides with the experimental value, provided that there are (4.4–8) $\times 10^7$ metallic shunts per square centimeter of the contact surface. The density of dislocations in single crystal GaP usually falls within 5×10^5–10^6 cm^{-2}, which is one and a half to two orders of magnitude smaller than the above estimate. However, the process of In fusion into GaP is accompanied by the evaporation of phosphorus and by the development of mechanical stresses related to differences between the lattice period of GaP (0.545 nm), the atomic radius of In (0.16 nm), and the lattice period of In (0.587 nm) in the metallic phase probably formed upon fusion. These factors may increase the density of states in the contact region by one to two orders of magnitude.

Conclusions. The results of investigations of the temperature dependence of the electric resistance of the fused In–GaP ohmic contact showed that the specific contact resistance increases with the temperature in the temperature range from 230 to 420 K, which contradicts the existing theories of current flow in the ohmic contact. It is suggested that the In–GaP ohmic contact is due to conducting metallic shunts formed as a result of the deposition of In atoms on dislocations and other structural imperfections. The density of these shunts per unit contact surface area, evaluated at (4.5–8) $\times 10^7$ cm^{-2}, corresponds to the density of imperfections at the metal–semiconductor interface.

The bulk resistivity of indium (ρ_{In}), the shunt resistance (R_{shunt}), the specific contact resistance (R_c), and the number of conducting shunts per unit contact area (N) calculated for various temperatures T

T, K	ρ_{In}, Ω cm	R_{shunt}, Ω	R_c, Ω cm²	N, cm^{-2}
250	7.6×10^{-6}	2.2×10^4	2.4×10^{-4}	8×10^7
300	9.6×10^{-6}	2.8×10^4	4.8×10^{-4}	5.8×10^7
350	11.6×10^{-6}	3.4×10^4	7×10^{-4}	4.8×10^7
400	13.6×10^{-6}	4×10^4	9×10^{-4}	4.4×10^7

REFERENCES

1. E. H. Rhoderick, *Metal-Semiconductor Contacts* (Clarendon, Oxford, 1978; Radio i Svyaz', Moscow, 1982).
2. A. Y. C. Yu, Solid-State Electron. **13**, 239 (1970).
3. A. Katz, S. Nakahara, W. Savin, and B. E. Weir, J. Appl. Phys. **68**, 4133 (1990).
4. T. Clausen and O. Leistiko, Appl. Phys. Lett. **62**, 1108 (1993).
5. S. N. G. Chu, A. Katz, T. Boone, *et al.*, J. Appl. Phys. **67**, 3754 (1990).
6. J.-S. Jang and T.-Y. Seong, Appl. Phys. Lett. **76**, 2743 (2000).

7. T. V. Blank, Yu. A. Goldberg, E. V. Kalinina, *et al.*, Fiz. Tekh. Poluprovodn. (St. Petersburg) **35**, 550 (2001) [Semiconductors **35**, 529 (2001)].
8. H. Shimawaki, N. Furuhata, and K. Honjo, J. Appl. Phys. **69**, 7939 (1991).
9. Z. Fan, S. N. Mohammad, W. Kim, *et al.*, Appl. Phys. Lett. **68**, 1672 (1996).
10. J. D. Guo, C. I. Lin, M. S. Feng, *et al.*, Appl. Phys. Lett. **68**, 235 (1996).
11. A. A. Bergh and P. J. Dean, *Light Emitting Diodes* (Clarendon, Oxford, 1976; Mir, Moscow, 1979).
12. T. V. Blank and Yu. A. Goldberg, Fiz. Tekh. Poluprovodn. (St. Petersburg) **37**, 1025 (2003) [Semiconductors **37**, 999 (2003)].
13. J. Narayan, P. Tiwari, X. Chen, *et al.*, Appl. Phys. Lett. **61**, 1290 (1992).
14. E. J. Miller, D. M. Schaadt, E. T. Yu, *et al.*, J. Appl. Phys. **94**, 7611 (2003).
15. E. J. Miller, E. T. Yu, P. Waltereit, and J. S. Speck, Appl. Phys. Lett. **84**, 535 (2004).
16. V. V. Evstropov, M. Dzhumaeva, Yu. V. Zhilyaev, *et al.*, Fiz. Tekh. Poluprovodn. (St. Petersburg) **34**, 1357 (2000) [Semiconductors **34**, 1305 (2000)].

Translated by P. Pozdeev

Technical Physics Letters, Vol. 30, No. 10, 2004, pp. 810–812. Translated from Pis'ma v Zhurnal Tekhnicheskoĭ Fiziki, Vol. 30, No. 19, 2004, pp. 25–29.

Correlation between the Electrical and Luminescent Properties of High-Purity Gallium Arsenide

M. V. Botnaryuk, Yu. V. Zhilyaev, T. A. Orlova, N. K. Poletaev*, L. M. Fedorov, and Sh. A. Yusupova

Ioffe Physicotechnical Institute, Russian Academy of Sciences, St. Petersburg, 194021 Russia

** e-mail: poletaev@mail.ioffe.ru*

Received March 15, 2004

Abstract—Epitaxial *n*-GaAs layers with a background impurity concentration of $N_D - N_A < 10^{15}$ cm^{-3}, grown by chloride vapor phase epitaxy in an open system, exhibit correlation between the electrical properties and the long persistence of the edge photoluminescence lines D^0x and D^0h related to the hole trapping centers. An increase in the concentration of such trapping centers in *n*-GaAs leads to a decrease in the mobility of free charge carriers. © *2004 MAIK "Nauka/Interperiodica".*

Determination of the quality of high-purity GaAs ($N_D - N_A < 10^{15}$ cm^{-3}) by optical methods is a problem of interest for both basic science and practical applications. In many cases, optical methods of evaluation of the material characteristics are the only possible means of nondestructive quality control. One of the most important practical tasks is to evaluate the electrical properties of GaAs, which determine the characteristics of related semiconductor devices, by monitoring the optical properties of this material. Problems pertaining to the use of optical diagnostic methods for determining the electrical properties of GaAs were discussed in [1–3].

Recently [4], we reported on establishing a relationship between the electrical properties of *n*-GaAs and the relative intensities of spectral lines in the spectra of low-temperature exciton photoluminescence (PL) in this material. It was experimentally demonstrated that changes in the density and mobility of majority carriers are accompanied by transformations of the stationary low-temperature PL spectra. The free carrier density in *n*-GaAs is determined primarily by the concentration of shallow donors. However, it is known that the shape of the low-temperature exciton PL spectra of *n*-GaAs may be influenced by the hole trapping centers [5]. The presence of such centers gives rise to anomalously long ($\tau >$ 10 μs) persistence of the spectral lines D^0x and D^0h of low-temperature exciton PL related to the shallow donors [6].

We have studied the effect of hole trapping centers on the luminescent and electrical properties of *n*-GaAs. The experiments were performed on pure epitaxial GaAs layers with a thickness within several dozens of microns and a background impurity concentration of $N_D - N_A < 10^{15}$ cm^{-3}. The epitaxial layers were grown by chloride vapor phase epitaxy in an open system. The major carrier density and mobility were determined by the Hall effect measurements using the Van der Pauw method. The stationary low-temperature exciton PL spectra and the PL decay kinetics were measured at T = 2 K. The stationary PL was excited by a He–Ne laser operating at a wavelength of λ = 632.8 nm. Pulsed excitation was effected by a semiconductor laser operating at $\lambda \approx$ 760 nm. The stationary PL spectra were registered in the proton counting mode; the PL kinetics was studied using the time-correlated photon counting scheme.

An analysis of the results of measurements revealed correlation between the concentration N_Z of hole trapping centers in *n*-GaAs and the electrical properties of epitaxial layers, in particular, the density and mobility of free carriers. It was established that a growth in the concentration of hole trapping centers leads to an increase in the density of free carriers and a decrease in their mobility (Fig. 1).

In order to compare the concentrations of hole trapping centers in various samples, we used the ratio B of the areas under curves of the PL decay kinetics (see the inset in Fig. 1). The integration limits $t1$ and $t3$ were determined as the moments of termination of the excitation pulse and the photon counting period, respectively. The integration limit $t2$ corresponded to the moment of termination of the free exciton PL for the line exhibiting no long persistence [5]. The B value being a monotonic function of the concentration of the hole trapping centers, $B = F(N_Z)$, this ratio was used for

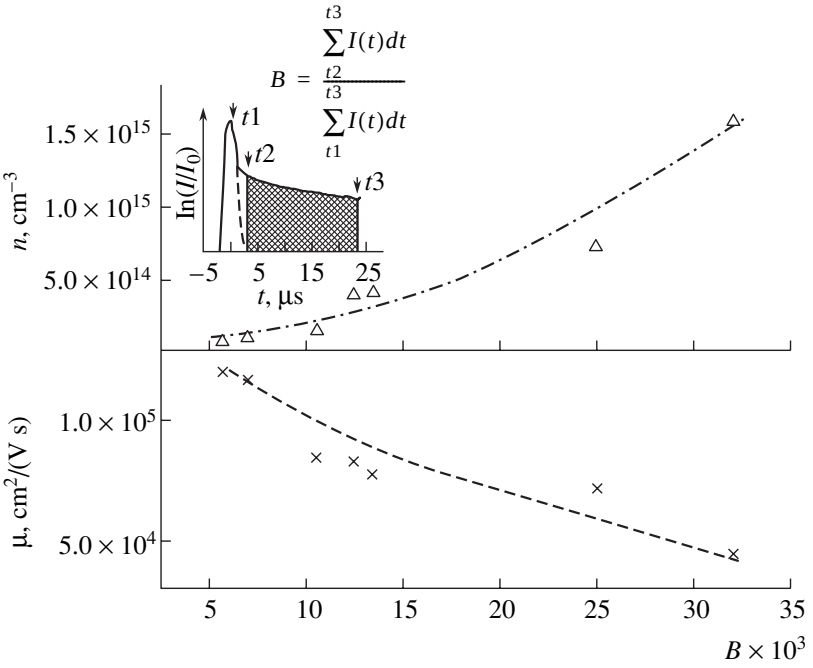

Fig. 1. Plots of the major carrier density n and mobility μ versus trap concentration N_Z in epitaxial n-GaAs. The inset illustrates the method of calculation of the concentration of trapping centers.

the quantitative comparison of the concentrations of such centers in the GaAs samples studied.

A change in the electrical properties of GaAs was accompanied by transformation of the low-temperature exciton PL spectra of the samples. Figure 2 shows such spectra for a series of samples with different concentrations N_Z of the hole trapping centers. The concentration of traps increased in the series of samples from S7 to S1. As can be seen in Fig. 2, the increase in N_Z is accompanied by broadening of the D^0x line and by an increase in its relative intensity.

Thus, the hole trapping centers responsible for the long persistence of D^0x and D^0h lines influence both electrical and optical properties of GaAs. An increase in the concentration of these centers leads to a significant decrease in the mobility of charge carriers and is accompanied by broadening of the D^0x line in the low-temperature exciton PL spectra and by an increase in the relative intensity of this line.

The relation between the full width at half maximum (FWHM) of the D^0x line and the long persistence was recently considered in [7], where an increase in the relative intensity of long persistence was also accompanied by broadening of the D^0x line. It should be noted that no long persistence is observed in GaAs with low carrier density ($n_e < 10^{13}$ cm^{-3}) and high mobility ($\mu_e > 100000$ cm^2/(V s) at $T = 77$ K). The low-temperature exciton PL spectra of such a material either contain no D^0x line or display this line with a very small halfwidth (FWHM < 0.15 meV). These facts are indicative of the complete absence of hole traps of this type in an ultrahigh-purity material. Thus, we may ascertain that the presence of this type of trap, in addition to shallow donors, may significantly influence the electrical and luminescent properties of pure GaAs.

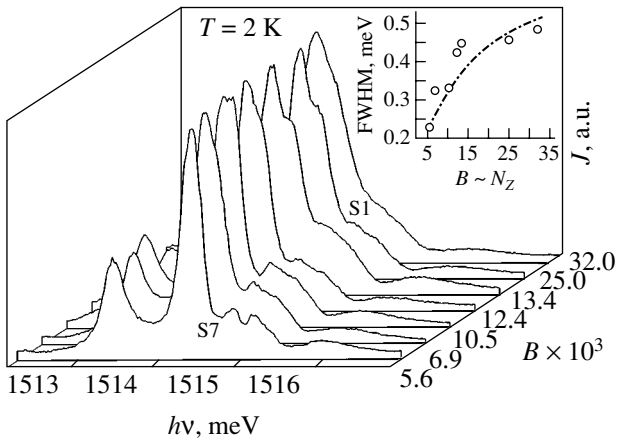

Fig. 2. Transformation of the low-temperature exciton PL spectra in GaAs with variable concentration N_Z of trapping centers (the spectra are normalized to the maximum intensity of the D^0x line). The inset shows a plot of the halfwidth (FWHM) of the D^0x line versus the concentration N_Z of trapping centers.

REFERENCES

1. K. D. Glinchuk and A. V. Prokhorovich, Fiz. Tekh. Poluprovodn. (St. Petersburg) **36**, 519 (2002) [Semiconductors **36**, 487 (2002)].
2. Z. H. Lu, M. C. Hanna, D. M. Szmyd, *et al.*, Appl. Phys. Lett. **56**, 177 (1990).
3. G. Oelgart, S. Gramlich, T. Bergunde, *et al.*, Mater. Sci. Eng., B **44**, 228 (1997).
4. Yu. V. Zhilyaev, N. A. Poletaev, V. M. Botnaryuk, *et al.*, Phys. Status Solidi C **0**, 1024 (2003).
5. A. V. Akimov, V. V. Krivolapchuk, N. K. Poletaev, and V. G. Shofman, Fiz. Tekh. Poluprovodn. (St. Petersburg) **27**, 310 (1993) [Semiconductors **27**, 171 (1993)].
6. A. V. Akimov, A. A. Kaplyanskiĭ, V. V. Krivolapchuk, and E. S. Moskalenko, Pis'ma Zh. Éksp. Teor. Fiz. **46**, 35 (1987) [JETP Lett. **46**, 42 (1987)].
7. V. V. Krivolapchuk, M. M. Mezdrogina, and N. K. Poletaev, Fiz. Tverd. Tela (St. Petersburg) **45**, 29 (2003) [Phys. Solid State **45**, 28 (2003)].

Translated by P. Pozdeev

Technical Physics Letters, Vol. 30, No. 10, 2004, pp. 813–816. Translated from Pis'ma v Zhurnal Tekhnicheskoĭ Fiziki, Vol. 30, No. 19, 2004, pp. 30–39.

Experimental Investigation of Graphite Explosive-Emission Cathodes Operating in a Periodic Pulse Regime

S. D. Korovin, E. A. Litvinov, G. A. Mesyats, A. M. Murzakaev, V. V. Rostov*, V. G. Shpak, S. A. Shunailov, and M. I. Yalandin**

Institute of High-Current Electronics, Siberian Division, Russian Academy of Sciences, Tomsk, Russia
Institute of Electrophysics, Ural Division, Russian Academy of Sciences, Yekaterinburg, Russia
*e-mail: * rostov@lfe.hcei.tsc.ru; ** yalandin@iep.uran.ru*

Received April 5, 2004

Abstract—We have studied the electron emission from graphite cathodes under the action of voltage pulses with an amplitude of up to 300 kV, a pulse duration of 10^{-9} s, and a pulse repetition frequency of 1–3.5 kHz. The magnetically insulated electron beam had a peak power of up to 600 MW at an average power of 1–3 kW. The dynamics of emission current delay was studied in relation to the charge transferred by the beam and to the state of the cathode surface (studied by scanning electron microscopy). It is established that smoothening of the microrelief leads to degradation of the cathode emissivity, which can be compensated by increasing the pulse repetition rate above a certain critical level. © *2004 MAIK "Nauka/Interperiodica".*

Previously [1] we have studied the characteristics of an original relativistic microwave backward wave oscillator (BWO) for a 38 GHz range, implementing a high-current hybrid modulator [2] and a magnetic system of electron beam focusing, which provided system operation in a periodic pulse regime with a pulse train width of 1 s at a pulse repetition rate of up to 3500 Hz. The coaxial magnetically insulated vacuum diode of the electron accelerator was equipped with an explosive-emission tubular sharp-edged cathode made of MPG-6 grade graphite with a diameter of 8.6 mm. The electron current density was 5×10^4 A/cm^2 for an emitting belt radial size of ~150 μm. The cathode was situated in the region of a homogeneous magnetic field with an induction of ~2 T. It was also of interest to study the peculiarities of operation of the accelerator cathode generating an electron beam with a high peak (~600 MW) and high average (up to 3 kW) power.

The accelerating voltage pulses had a trapezoidal shape with a leading front width of 200 ps, a pulse top width of ~900 ps and a full width at half maximum (FWHM) of 1500 ps at an amplitude (on the cathode) of up to –290 kV. The high amplitude stability (rms deviation not exceeding 1%) of these pulses allowed us to use a 6-GHz Tektronix TD820 digital sampling oscillograph forming each oscillogram by accumulating 512 sequential readings. Thus, at a sweep of 500 ps per division, the accuracy of measurements of the time characteristics was determined by a discretization period of 10 ps. The parameters of electron beam current pulses with an amplitude of ~2 kA (Fig. 1) were measured using a probe arranged in the drift chamber of the accelerator. The probe had the form of a Faraday cylinder mounted on the end of a 3-Ω coaxial line with an output matched to a strip line. The accuracy of calibration of the probes measuring the accelerating voltage and the electron beam current was ~5%; the transient time characteristics were not worse than 150–200 ps. The current measurements were performed using the ability of Tektronix TD820 to integrate oscillograms, thus providing measurement of the total electron beam charge Q.

The electron beam current pulses presented in Fig. 1 were measured in the course of cathode training. Figure 2 shows a plot of the charge Q versus number N of pulses for the cathode initially trained using N =

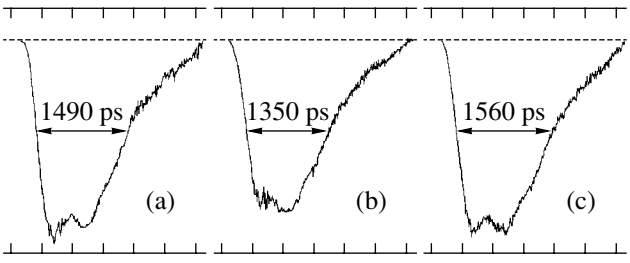

Fig. 1. Typical oscillograms of the electron beam current pulses with an amplitude of ~2 kA in 1000-pulse trains measured using a Faraday cylinder and digital sampling oscillograph accumulating 512 readings for each oscillogram: (a) untrained cathode (repetition rate, 1000 Hz); (b) cathode trained by 12000 pulses at the same repetition rate; (c) cathode additionally trained (to 17000 pulses) at a repetition rate of 3500 Hz.

1063-7850/04/3010-0813$26.00 © 2004 MAIK "Nauka/Interperiodica"

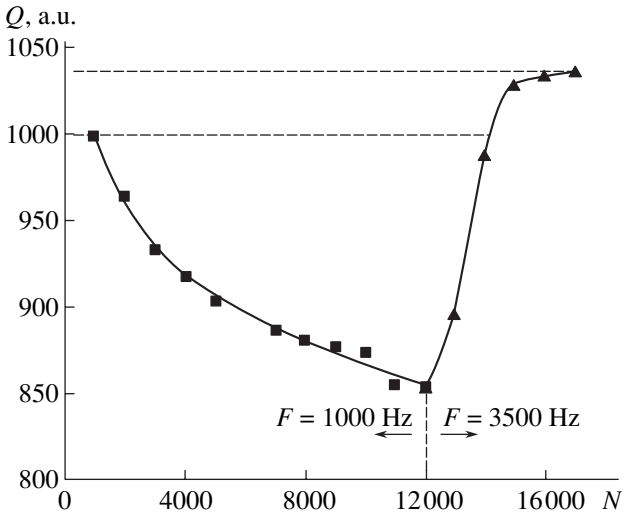

Fig. 2. A plot of the electron beam charge Q versus number N of pulses for the cathode trained using $N = (0–12) \times 10^3$ in the regime of 1000-pulse trains at a repetition rate of 1000 Hz, followed by additional training for $N = (12–17) \times 10^3$ in the same regime at a repetition rate of 3500 Hz.

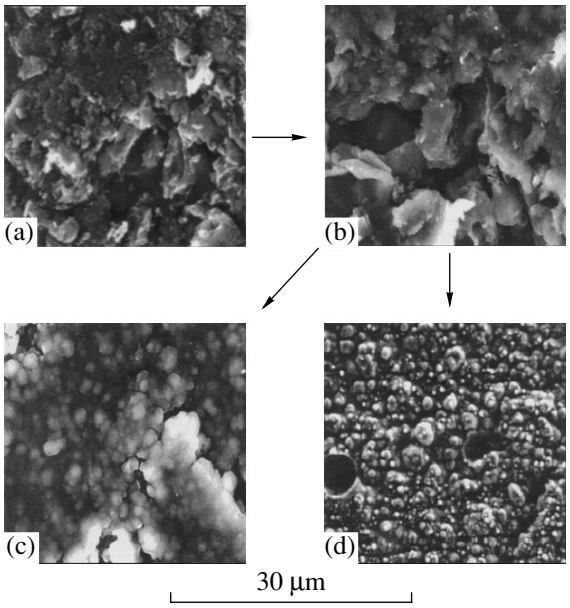

Fig. 3. Scanning electron micrographs of the surface of the emitting cathode edge: (a) before training; (b) after training using $N = 10^4$ at a repetition rate of 1000 Hz; (c) after training using $N = 3 \times 10^4$ in the same regime; (d) after training at a repetition rate of 1000 Hz and then at 3500 Hz according to Fig. 2.

$(0–12) \times 10^3$ in the regime of 1000-pulse trains at a repetition rate of 1000 Hz. The onset of the descending region (N = 1000) corresponds to the oscillogram in Fig. 1a; the oscillogram in Fig. 1b was obtained after 12×10^3 pulses. This training regime revealed decay in the characteristic beam current amplitude, a decrease in the pulse duration, and a slight extension of the pulse front. The passage to a regime with 1000-pulse trains at a repetition rate of 3500 Hz leads to changes manifested in the region of $N = (12–17) \times 10^3$ (Fig. 2). The maximum value of $N = 17 \times 10^3$ corresponds to the oscillogram in Fig. 1c. An analysis of these data showed that in this regime, in contrast to that with a repetition rate of 1000 Hz, a sharp decrease (from 1 ms to ~300 μs) in the interval between pulses led to a significant change in the emissive properties of the cathode, whereby the initial charge level was restored and even somewhat increased. It should be noted that the plot in Fig. 2 qualitatively repeats the shape of the curve of the beam current pulse duration versus the number of pulses. The pulse duration was measured on the level of half amplitude corresponding to the injection current from an untrained cathode.

Figure 3 presents micrographs of the cathode surface, which were obtained using a scanning electron microscope in the regime of electron beam induced current at various stages of cathode training (cf. Figs. 1 and 2).

In order to interpret the obtained body of data, we performed an analysis and determined the following characteristics.

(i) The emission current density sufficient for the Joule heating and destruction of a separate emission center on the cathode surface during a voltage pulse (~10^3 ps) was determined taking into account the thermal and electrical properties of massive graphite.

(ii) The electric field in the region of emitter was evaluated and its spatial scale was assessed proceeding from the "3/2" law and the measured emission current density.

(iii) The dynamics of heat removal from the emitter during the time interval between pulses was considered with allowance for graphite evaporation and thermal conductivity.

According to the concept of explosive electron emission [3], it was assumed that electrons are emitted, under the action of high voltage pulses, from separate microscopic regions characterized by the maximum electric field amplification coefficient. Taking into account the micrographs of the cathode surface (Fig. 3) and published data (see [3, 4] and references therein) such a microemitter was modeled by a protrusion with the shape close to a hemisphere or a truncated cone with a large apical angle. The process of energy evolution in such an emitter is described by the equation

$$\rho c(\partial T/\partial t) = j^2(r/r')^4 k, \qquad (1)$$

where the left-hand side is the change in the internal energy of the cathode and the right-hand side is the heat evolved due to the Joule heat dissipation. In this equation, ρ is the cathode material density, c is the heat capacity, T is the absolute temperature, t is the current

time, j is the emission current density, k is the resistivity, r is the linear size of the emission zone, and r' is the coordinate measured in depth of the cathode. In writing Eq. (1), we ignored thermal conductivity; this factor will be considered below. The thermal and electrical parameters of the cathode material were taken equal to those for massive graphite [5]. Based on the analysis of published data, we adopted the following approximations:

$$\rho c = 1.72 \ln T - 7.93, \quad (2)$$

$$k = k_0 T, \quad (3)$$

where (ρc) is expressed in [J cm^3/K]; T in kelvins; κ in [Ω cm] and $k_0 \approx 3.75 \times 10^{-8}$ Ω cm/K. The binding energy per atom is taken equal to $\varepsilon = 10$ eV [4].

In order to destroy the emitting region, it is necessary that the current density would provide for its heating up to ~10^5 K during the current pulse (~10^3 ps). Figure 4a shows a solution of Eq. (1) obtained under these conditions with allowance for relations (2) and (3). These calculations allow the necessary emission current density to be evaluated at ~10^9 A/cm^2.

Apparently, relations (2) and (3) are inapplicable at high temperatures. We should also take into account the presence of pores in graphite, since these pores are filled by the electron gas due to thermionic emission and, hence, significantly influence the thermal and electrical properties of the cathode material. The structure of Eq. (1) can be represented as

$$\int_0^t j^2 dt' = (\rho c)_0 / k_0 f(T),$$

where $(\rho c)_0$ is the value of this product at room temperature and $f(T)$ is a function weakly dependent on the temperature and the material properties. Therefore, it can be expected that the error in the determination of j is small. This conclusion was confirmed by the results of special numerical experiments. The magnitude of the integral of action is

$$\int_0^t j^2 dt' \approx 10^9 \text{ A}^2 \text{ cm}^{-4} \text{ s}.$$

In order to estimate the spatial scale of the emitting region, we proceed from the "3/2" law written in the following form:

$$j = AE^2/\sqrt{U}. \quad (4)$$

The geometry of the region of space charge formation is reflected by the electric field strength; U is the applied voltage; and $A = 2.33 \times 10^{-6}$ A/V$^{3/2}$. Estimates

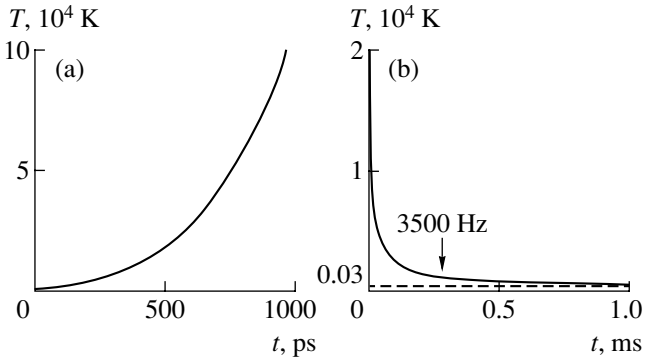

Fig. 4. The results of calculations of temperature kinetics for (a) the emitter at an emission current of $j = 10^9$ A/cm^2 and (b) the explosive-emission center after termination of the beam current pulse and the initial cooling due to evaporation.

obtained using relation (4) yield $E \approx (4–5) \times 10^8$ V/cm. The necessary current density is provided by thermionic and field emission at lower fields (for the work function $\varphi = 4.7$ eV), which implies limitation by the space charge (4). For $E \approx U/r$, the size of the emitting inhomogeneity is estimated as $r \approx 5 \times 10^{-4}$ cm. The current via such an explosive-emission center is $i \approx jr^2 \approx (2–3) \times 10^2$ A, and the number of such centers is $N \approx I/i \approx 5–10$. Taking the field strength in relation (4) to be equal to the average value $E_{av} \approx U/\sqrt{D_c h/2} \approx 4$ MV/cm (according to the exact calculation, the field average over the cathode edge area is 3–3.5 MV/cm), we obtain $j_{av} \approx 8 \times 10^4$ A/cm^2 (which is close to the experimental value of 5×10^4 A/cm^2). It should be noted that, in the case under the consideration (in the vacuum diode with a magnetic induction of 2 T), one must also take into account the possible influence of the cathode screening [6] on the discreteness of emitting centers.

Let us consider the dynamics of the emitter temperature relaxation process. The thermal conductivity coefficient of the cathode material can be approximated as follows [5]:

$$\lambda \approx 121.66 T^{-0.792}, \quad (5)$$

where λ is expressed in W/(cm K) and T in kelvins. The effect of the thermal conductivity and the boundary conditions (emission- and evaporation-induced cooling) during the pulse action spreads over a characteristic temperature diffusivity length $L_T \approx \sqrt{\lambda t/\rho c}$. Evaluation taking into account relations (2) and (5) shows that this length is small as compared to the characteristic scale r. For a pulse width of ~10^3 ps, the temperature relaxation processes are "switched" only after termination of the current injection; the process of cooling due to evaporation and thermal conductivity takes place only during the time interval between pulses.

The evaporation rate was estimated using the formula $V \approx V_\perp \exp(-\varepsilon/T)$, where $V_\perp$ is the transverse sound velocity in the cathode material. The evaporation process can be described by the equation

$$dr'/dt = V_\perp \exp(-\varepsilon/T). \quad (6)$$

Taking into account the coordinate dependence in Eq. (1), we obtain

$$t = r/V_\perp \int_1^{x1} \exp(\varepsilon/T(x))dx, \quad T(x) = T_0(\varepsilon/T_0)^{x^{-4}}, \quad x1 = r'/r. \quad (7)$$

The results of calculations using formulas (7) show that the process rapidly ceases after evaporation of a very thin layer. This is related to a sharp coordinate dependence of the temperature according to Eq. (1). The evaporation process prevails within a time period on the order of 10 ns, whereby the temperature decreases to $T \approx 2 \times 10^4$ K, after which thermal conductivity begins to dominate.

The process of cooling via thermal conductivity can be described as

$$\rho c(\partial T/\partial t) \approx -\lambda T/(r^2 + \lambda t/\rho c), \quad (8)$$

where the right-hand side is written taking into account the form of the temperature influence function [7].

The solution of Eq. (8) presented in Fig. 4b shows that the emitter cools down to 300 K during a time on the order of 1 ms, which corresponds to a pulse repetition rate of 1000 Hz. Experiments showed that the cathode surface geometry in this case changes (Figs. 3a ⟶ 3b ⟶ 3c) in accordance with the well-known effect of polishing of the surface of explosive-emission cathodes under the action of short voltage pulses [8]. The smoothening of microrelief leads to an increase in delay of the beam current emission and to a decrease in the charge transferred during each pulse (Fig. 2). It should be noted that the emission decreases not only as a result of this polishing, but also due to the graphite degassing and cleaning from various inclusions.

When the voltage pulses are applied at a repetition frequency of 3500 Hz, the emission center on the cathode surface does not cool before the arrival of the next pulse and the new center can be expected to form in the vicinity of the old one. This is favored by thermionic emission from the region with increased temperature. Therefore, there is increasing heating of the cathode surface near the emission center and, judging by the micrograph in Fig. 3d, this regime leads to melting of the cathode edge at a sufficiently large number of pulses in the train. This conclusion is confirmed not only by homogenization of the cathode surface and an apparent decrease in porosity, but also by the appearance of solidified craters as a result of the emergence of bubbles of the adsorbed gas. The sharp edges of such craters may be the sites of localization of the new centers of emission during the action of subsequent pulse trains. Therefore, an increase in the temperature in the emission zone and specific "regeneration" of the microrelief may well account for an increase in the electron beam charge (Fig. 2) observed for a higher pulse repetition rate.

In conclusion, the above considerations show the possible existence of a frequency-dependent threshold for the cathode polishing effect. Analogous estimates obtained for metals indicate that such a threshold occurs in the megahertz range of the pulse repetition rate.

Acknowledgments. The authors are grateful to S.N. Rukin, S.K. Lyubutin, and B.G. Slovikovsky for kindly providing the opportunity to use the experimental techniques.

This study was supported by the Russian Foundation for Basic Research, project no. 04-02-16576a.

REFERENCES

1. D. M. Grishin, V. P. Gubanov, S. D. Korovin, *et al.*, Pis'ma Zh. Tekh. Fiz. **28** (19), 24 (2002) [Tech. Phys. Lett. **28**, 806 (2002)].
2. S. K. Lyubutin, G. A. Mesyats, S. N. Rukin, *et al.*, Prib. Tekh. Éksp., No. 5, 80 (2001).
3. G. A. Mesyats, *Ektons in Vacuum Discharge: Breakdown, Spark, Arc* (Nauka, Moscow, 2000) [in Russian].
4. E. P. Sheshin, *Surface Structure and Field Emission Properties of Carbon Materials* (Mosk. Fiz.-Tekh. Inst., Moscow, 2001) [in Russian].
5. *Tables of Physical Data: Reference Book*, Ed. by I. K. Kikoin (Atomizdat, Moscow, 1976) [in Russian].
6. S. Ya. Belomyttsev, S. D. Korovin, and G. A. Mesyats, Pis'ma Zh. Tekh. Fiz. **6**, 1089 (1980) [Sov. Tech. Phys. Lett. **6**, 466 (1980)].
7. A. N. Tikhonov and A. A. Samarskii, *Equations of Mathematical Physics* (Nauka, Moscow, 1977; Pergamon Press, Oxford, 1964).
8. B. Juttner, V. F. Putchkarjov, and W. Rohrbech, in *Proceedings of the 7th International Symposium on Discharges and Electrical Insulation in Vacuum, Novosibirsk, 1976*, pp. 189–192.

Translated by P. Pozdeev

Technical Physics Letters, Vol. 30, No. 10, 2004, pp. 817–819. Translated from Pis'ma v Zhurnal Tekhnicheskoĭ Fiziki, Vol. 30, No. 19, 2004, pp. 40–45.

Energy Transfer in a Dielectric Medium with Allowance for the Relaxation Polarization

O. A. Emel'yanov

St. Petersburg State Technical University, St. Petersburg, Russia

e-mail: oae@mail.wplus.net

Received April 20, 2004

Abstract—Energy relations of the macroscopic electrodynamics of a dielectric medium are considered with allowance for the relaxation polarization. An expression for the dielectric loss power flux density is obtained in the case of an arbitrary time-dependent electric field. An energy characteristic of the efficiency of insulators for capacitive energy storages is proposed. © *2004 MAIK "Nauka/Interperiodica".*

For a comparative evaluation of insulators for the modern capacitive energy storages, it is a common practice to use an expression for the stored electric energy density

$$W_e = \frac{\varepsilon\varepsilon_0 E^2}{2}, \quad (1)$$

where ε_0 and ε are the absolute and relative permittivities, respectively, and E is the electric field strength. By ε is frequently implied the static permittivity ε_s corresponding to a dc electric field of zero frequency ($\omega = 0$). Most modern polymeric capacitor insulators are characterized by a frequency- and temperature-dependent $\varepsilon(\omega, T)$, which is caused by the relaxation polarization processes. The energy W_{eff} supplied by such a capacitor to a load is determined by the stored energy W_e minus the energy W_Q of relaxation losses, the latter being spent mostly for heating of the insulator. Under conditions of intense electrothermal loading, a capacitor insulator with relaxation losses may exhibit thermal switching and breakdown phenomena, as was previously demonstrated theoretically [1, 2] and experimentally [3].

In practical applications involving relatively small electrothermal loads, the effective energy W_{eff} is usually evaluated using the relation

$$W_{eff} = \frac{r}{r + r_{se}} W_e, \quad (2)$$

where r is the load resistance and r_{se} is the serial equivalent resistance of the given insulator. Formula (2) implies the active character of the load and a simple serial equivalent scheme of the insulator, which is rarely valid in practice. Moreover, r_{se} corresponds to the conditions of established sinusoidal field, whereas real loading frequently takes place in a single cycle regime.

It would be more correct to evaluate W_{eff} as

$$W_{eff} = W_e - W_Q, \quad (3)$$

but this requires the knowledge of W_Q or an expression for the loss power flux density Q, from which

$$W_Q = \int Q(t)dt. \quad (4)$$

However, the available treatises on electrodynamics [4, 5] and the physics of dielectrics [6, 7] give expressions only for the average power losses over the period T of a sinusoidal field E,

$$\overline{Q} = \frac{1}{T}\int_0^T jE dt, \quad (5)$$

where j is the total current density in the dielectric medium. In order to evaluate Q and W_{eff}, it is necessary to use additional considerations valid for arbitrary (not necessary periodic) fields. Then, using the concept of the loss power flux density Q for a periodic field, we obtain

$$\overline{Q} = \frac{1}{T}\int_0^T Q(t)dt. \quad (6)$$

Let us consider a nonmagnetic dielectric medium in which the polarization is established via a relaxation process,

$$P(t) = \varepsilon(\varepsilon_\infty - 1)E + \varepsilon_0 \int_{-\infty}^{t} \alpha(t-u)E(u)du, \quad (7)$$

where ε_∞ corresponds to the instantaneously established forms of polarization and $\alpha(t)$ is the dielectric

decay function [7]. The Poynting vector **S** corresponding to the stored (and released) electric field energy obeys the equation

$$-\mathrm{div}\mathbf{S} = \frac{\partial}{\partial t}\frac{\varepsilon_0\varepsilon_\infty E^2}{2} + E\frac{\partial P}{\partial t} = \frac{\partial W_e}{\partial t} + Q. \quad (8)$$

In the most general case of arbitrary fields and polarization mechanisms (7), $\frac{\partial W_e}{\partial t}$ and Q in the intermediate relation (8) cannot be separated. However, this separation is possible in some particular cases such as model plasma comprising a system of oscillators for which the expressions describing W_e and Q were obtained in [8]. Analogous expressions can be obtained in the case of the relaxation polarization, provided that relation (7) represents a differential equation explicitly dependent on the field E. A sufficient condition for this is that the kernel $\alpha(t)$ would be degenerate as, for example, in the case of Debye relaxation [7]:

$$\alpha(t) = \frac{\varepsilon_s - \varepsilon_\infty}{\tau}\exp\left(-\frac{t}{\tau}\right), \quad (9)$$

where ε_s is the static permittivity and τ is the relaxation time. In this case, the relaxation polarization component $P_r(t)$ obeys the linear differential equation

$$\frac{dP_r(t)}{dt} + \frac{P_r(t)}{\tau} = \frac{\varepsilon_0(\varepsilon_s - \varepsilon_\infty)}{\tau}E(t). \quad (10)$$

Accomplishing the necessary transformations, we eventually obtain the following expressions for the flux densities of the stored (released) electric field power and dielectric (heat) losses:

$$\frac{\partial W_e}{\partial t} = \frac{1}{\varepsilon_0(\varepsilon_s - \varepsilon_\infty)}P_r(t)\frac{dP_r(t)}{dt} + \frac{\partial}{\partial t}\frac{\varepsilon_0\varepsilon_\infty E^2}{2},$$
$$Q(t) = \frac{\tau}{\varepsilon_0(\varepsilon_s - \varepsilon_\infty)}\left[\frac{dP_r(t)}{dt}\right]^2. \quad (11)$$

In particular, for the monochromatic field $E = E_0\exp(i\omega t)$, the above relations yield the well-known expressions for the average loss power,

$$\bar{Q} = \frac{1}{T}\int_0^T Q(t)dt = \frac{\omega\tau(\varepsilon_s - \varepsilon_\infty)\varepsilon_0}{1+\omega^2\tau^2}\frac{E_0^2}{2} = \omega\varepsilon_0\varepsilon''\frac{E_0^2}{2}, \quad (12)$$

where ε'' is the imaginary part of the complex permittivity (loss factor). For an arbitrary field, the efficiency of capacitive energy storage should be determined using the expression for W_{eff} and a solution of Eq. (10) obtained with the aid of relations (11). For example, in the case of an exponentially decaying field $E = E_0\exp\left(-\frac{t}{\tau_E}\right)$, we use the relations $P_r(t) = P_r(E(t))$, $\frac{dP_r(t)}{dt} = \frac{dP_r}{dE}\frac{dE}{dt}$, and $t = -\tau_E\ln\left(\frac{E}{E_0}\right)$ to obtain a differential equation for $P_r(E)$,

$$\frac{dP_r}{dE} - \frac{\alpha}{E}P_r = -(\varepsilon_s - \varepsilon_\infty)\varepsilon_0\alpha, \quad (13)$$

where $\alpha = \frac{\tau_E}{\tau}$ is the ratio of characteristic times for the field variation and the relaxation polarization. The solution of this equation has the following form,

$$P_r(t) = \left(P_s + \frac{(\varepsilon_s - \varepsilon_\infty)\varepsilon_0\alpha}{1-\alpha}\right)\left[\frac{E}{E_0}\right]^\alpha - \frac{(\varepsilon_s - \varepsilon_\infty)\varepsilon_0\alpha}{1-\alpha}E, \quad (14)$$

where P_s is the initial polarization level at $t = 0$. Using the condition of passive discharge, $P_s = -\frac{(\varepsilon_s - \varepsilon_\infty)\varepsilon_0\alpha}{1-\alpha}$, we obtain

$$-\frac{\partial W_e}{\partial t} = -\frac{\partial}{\partial t}\frac{\varepsilon_0\varepsilon_\infty E^2}{2} + \frac{(\varepsilon_s - \varepsilon_\infty)\varepsilon_0\alpha^2}{(1-\alpha)^2\tau_E}E^2,$$
$$Q = \frac{(\varepsilon_s - \varepsilon_\infty)\varepsilon_0\alpha}{(1-\alpha)\tau_E}E^2. \quad (15)$$

Integrating relations (15) with respect to t from 0 to ∞ and taking $P_r(\infty) = 0$, we obtain

$$W_e = \frac{\varepsilon_0\varepsilon_\infty E_0^2}{2} + \frac{(\varepsilon_s - \varepsilon_\infty)\varepsilon_0\alpha^2}{(1-\alpha)^2}\frac{E_0^2}{2},$$
$$W_Q = \frac{(\varepsilon_s - \varepsilon_\infty)\varepsilon_0\alpha}{(1-\alpha)^2}\frac{E_0^2}{2} \quad (16)$$

and the total energy flux to the load

$$W_{eff} = \frac{(\varepsilon_s - \varepsilon_\infty)\varepsilon_0\alpha}{(1-\alpha)}\frac{E_0^2}{2} + \frac{\varepsilon_0\varepsilon_\infty E_0^2}{2}. \quad (17)$$

Evidently, W_Q is always positive (irrespective of α). For a passive discharge, we have $\alpha > 1$ and $W_{eff} > 0$, which corresponds to the positive direction of the Poynting vector outward from the insulator. In the case of $\alpha < 1$, the process is reversed and the energy is stored in the insulator at the expense of work performed by an external source. The case of $\alpha = 0$ corresponds to short circuit, whereby the entire stored energy is converted into heat $W_e = W_Q$.

Once the real insulator characteristics and the characteristic times of field variation (required discharge times) are known, it is possible to perform a comparative analysis of the efficiency of insulators in terms of the coefficient

$$\eta = \frac{W_{\text{eff}}}{W_{\text{e}}} = 1 - \frac{W_Q}{W_{\text{e}}}. \quad (18)$$

In particular, for an exponentially decaying field,

$$\eta = 1 - \frac{1}{\alpha - \dfrac{\varepsilon_\infty (1-\alpha)^2}{(\varepsilon_{\text{s}} - \varepsilon_\infty)\alpha}}, \quad (19)$$

which yields $\eta = 0$ for $\alpha = 1$ and $\eta \longrightarrow 1$ for $\alpha \gg 1$.

Using the parameters ε_∞, ε_{s}, and τ, and setting the discharge time τ_E, it is possible to select optimum insulators for a capacitive energy storage. For example, in the case of τ_E on the order of tens and hundreds of milliseconds (typical of the electromagnetic thermal systems [9]), it was suggested to use poly(propylene), although the use of poly(ethylene terephthalate) probably would be more effective. As is known, many real insulators are characterized by a spectrum of relaxation times τ. Allowance for this circumstance requires special consideration that goes outside the scope of this paper.

REFERENCES

1. O. A. Emel'yanov, Pis'ma Zh. Tekh. Fiz. **27** (16), 32 (2001) [Tech. Phys. Lett. **27**, 679 (2001)].
2. O. A. Emel'yanov, Pis'ma Zh. Tekh. Fiz. **28** (19), 76 (2002) [Tech. Phys. Lett. **28**, 830 (2002)]; **28** (22), 32 (2002) [**28**, 939 (2002)].
3. O. A. Emel'yanov, Élektrotekhnika, No. 4, 6 (2002).
4. L. D. Landau and E. M. Lifshitz, *Course of Theoretical Physics*, Vol. 8: *Electrodynamics of Continuous Media* (Nauka, Moscow, 1982; Pergamon, New York, 1984).
5. I. E. Tamm, *Principles of the Theory of Electricity* (Nauka, Moscow, 1966) [in Russian].
6. H. Frolich, *Theory of Dielectrics: Dielectric Constant and Dielectric Loss* (Clarendon, Oxford, 1986).
7. S. N. Koĭkov, *Physics of Dielectrics* (Leningrad. Politekh. Inst., Leningrad, 1967).
8. Yu. S. Barash and V. L. Ginzburg, Usp. Fiz. Nauk **118**, 523 (1976) [Sov. Phys. Usp. **19**, 263 (1976)].
9. H. G. Wisken and Th. H. G. Weise, IEEE Trans. Magn. **39**, 446 (2003).

Translated by P. Pozdeev

Technical Physics Letters, Vol. 30, No. 10, 2004, pp. 820–822. Translated from Pis'ma v Zhurnal Tekhnicheskoĭ Fiziki, Vol. 30, No. 19, 2004, pp. 46–52.

Thermomagnetic Data Writing and Erasing in DyCo/NiFe (TbFe/NiFe) Film Structures

V. A. Seredkin*, S. V. Stolyar, G. I. Frolov, and V. Yu. Yakovchuk

Kirensky Institute of Physics, Siberian Division, Russian Academy of Sciences, Krasnoyarsk, Russia

Krasnoyarsk State University, Krasnoyarsk, Russia

** e-mail: sva@iph.krasn.ru*

Received April 12, 2004

Abstract—A new principle of data writing and erasing is proposed based on the exchange coupling between magnetic layers with mutually orthogonal orientations of the effective magnetization. The new method provides for a significant decrease in energy consumption. The possibility of using bilayer magnetic films of the (rare earth metal–transition metal)/NiFe type possessing unidirectional anisotropy as the media for thermomagnetic writing and erasing of magnetooptical data is studied. © *2004 MAIK "Nauka/Interperiodica"*.

Uniaxial amorphous ferromagnetic films of rare earth and transition (REM–TM) metals with perpendicular magnetic anisotropy (TbFe, TbFeCo, DyCo, DyFeCo, etc.) are now most widely used as the media for thermomagnetic writing and erasing of magnetooptical data [1–4]. Thin films of these compounds with compositions in the compensation region are characterized by high values of perpendicular magnetic anisotropy ($K_\perp = 10^5$–10^6 erg/cm^3), sufficiently large magnetooptical parameters, and an acceptable range of temperatures and linear resolution for thermomagnetic writing and erasing of magnetooptical data. However, these media require application of a relatively large external write/erase magnetic field $H_w \sim (3–6) \times 10^4$ A/m, since lower values do not provide for the magnetic domain saturation in the zone of writing [5]. Another negative factor is a large time of transition from writing to erasing (determined by the coil inductance in the write/erase magnetic field source [4]), which limits the operating speed of devices using such data recording media. Therefore, the search for novel effective magnetooptical materials and new principles of data recording is a currently important task. One possible solution is based on the phenomenon of unidirectional anisotropy in exchange-coupled layers with different magnetic order.

We have obtained for the first time bilayer magnetic film TbFe/NiFe and DyCo/NiFe structures exhibiting unidirectional anisotropy in the sample plane and having mutually orthogonal magnetizations in the DyCo(TbFe) and NiFe layers [6, 7].

The very fact of formation of a unidirectional anisotropy, whereby orientations of the effective magnetization vectors of individual layers are mutually orthogonal and, hence, are not exchange-coupled ($J\mathbf{M}_1\mathbf{M}_2 = JM_1M_2\cos(M_1\hat{}M_2)$), is rather unusual. For this reason, the unidirectional anisotropy observed in the proposed bilayer film systems cannot be interpreted within the framework of existing notions [8], although it is clear that the observed effects are related only to the magnetic structure of the REM–TM layer.

The results of our investigations showed that the sign of displacement (ΔH) of the hysteresis loop of the NiFe layer relative to the zero magnetic field at room temperature is unambiguously determined by the direction of magnetization in the REM–TM layer. When the latter layer is demagnetized, the shift of the hysteresis loop of the NiFe layer vanishes, the coercive force (H_c) exhibits a severalfold increase, and the hysteresis loop becomes isotropic in the film plane.

In order to elucidate the nature of this effect, we have performed investigations using the methods of spin wave (SWR) and ferromagnetic (FMR) resonances [9]. It was established that the ferrimagnetic layer (DyCo or TbFe), characterized by the integral perpendicular magnetic anisotropy, represents a nanocrystalline heterophase system consisting of at least two magnetic phases. The magnetization vector of the 3*d* metal sublattice in one of these phases is parallel to the film plane. We believe that the exchange interaction between magnetizations of the NiFe layer and the in-plane component of the magnetization vector of the heterophase REM–TM layer is precisely what accounts for the appearance of unidirectional anisotropy in such systems. Thus, the unidirectional anisotropy in (REM–TM)/NiFe film structures has an exchange nature.

In addition, we have studied the temperature dependence of the coercive force H_c and the displacement field ΔH for the bilayer films. Figure 1 shows the typical curves for a film structure of the DyCo/NiFe type. For the structures with TbFe ferrimagnetic layer, the curves are analogous. As can be seen from these data,

the H_c and ΔH values sharply change in the temperature interval 350–370 K (Fig. 1, region II), where the coercive force exhibits a tenfold increase, while the shift of the hysteresis loop vanishes completely. This state is roughly retained in the adjacent temperature interval 370–430 K (region III). As the temperature grows further, the H_c of the NiFe layer decreases down to almost the initial level (region IV).

From the standpoint of practical applications of the (REM–TM)/NiFe films with unidirectional anisotropy, the most important temperature intervals correspond to regions I and III (Fig. 1). In the former region extending from 290 to 345 K (which is the working range of magnetooptical data storage), the values of static magnetic parameters H_c and ΔH exhibit no significant variation and the initial magnetic state of the REM–TM layer is not altered by remagnetization of the NiFe layer. The increase in H_c of the NiFe layer in region III is explained as follows. At temperatures in the interval ~370–430 K, the exchange interaction between REM–TM and NiFe layers is still retained, but the coercive force of the REM–TM layer decreases to such a level that the exchange interaction energy becomes sufficient to remagnetize this layer in the normal direction during remagnetization of the NiFe layer. This is reliably monitored by the polar magnetooptical Kerr effect. Obviously, this is not accompanied by a shift of the hysteresis loop, so that $\Delta H = 0$.

This phenomenon underlies the new principle of thermomagnetic data writing and erasing in bilayer (REM–TM)/NiFe film structures with unidirectional anisotropy. The recorded data are read from the REM–TM layer by means of the polar magnetooptical Kerr effect.

The above principle of writing data is illustrated in Fig. 2-I. In the initial state (Fig. 2-Ia), the REM–TM layer *2* occurs in the saturated state with the magnetization vector oriented, for example, downward (ground state). Due to the exchange coupling, the NiFe layer *3* also occurs in the saturated state with the magnetization vector oriented, for example, leftward. When an external writing magnetic field $H_w \geq H_c + \Delta H$ is applied antiparallel to the initial magnetization vector of layer *3* (Fig. 2-Ib), the magnetization direction in this layer changes to the opposite, while the magnetization state of layer *2* is not affected because H_w is much smaller than the anisotropic field ($H_u \geq 8 \times 10^5$ A/m) in this layer. Heating the local magnetized zone (Fig. 2-Ic) to any temperature within region III (Fig. 1) does not change the magnetic state of this zone in layer *3*, whose Curie temperature is much higher (~835 K). As was noted above, the energy of the exchange interaction between layers *2* and *3* changes the direction of magnetization in layer *2* to the opposite (upward). On cooling the given zone, this state is retained even upon removal of the external writing field H_w; the magnetization in layer *3* acquires a nonequilibrium helicoidal structure (Fig. 2-Id) [10]. This state corresponds to recording one bit of data in layer *2*. The domain formed in the magnetized zone will always occur in the saturated state, which is maintained by a mechanism different from that described in [5]. In our case, the exchange interaction between homogeneously magnetized layer *3* and layer *2* prevents the formation of a multidomain structure in the course of formation of the data-bearing domain.

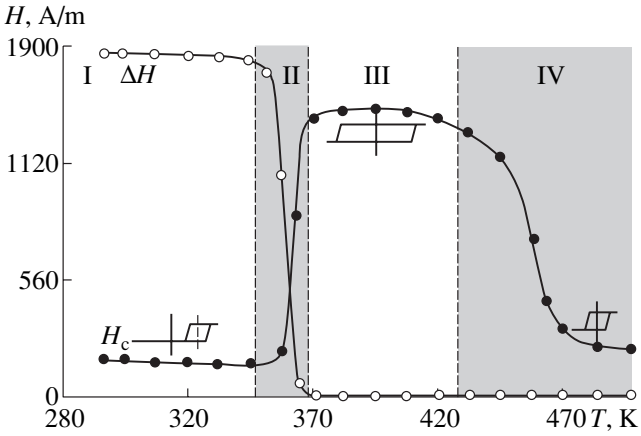

Fig. 1. Temperature dependences of the coercive force H_c and the displacement field ΔH in the NiFe layer of a bilayer DyCo/NiFe (TbFe/NiFe) film structure (see the text for explanations).

The principle of erasing data from the domains formed as described above is illustrated in Fig. 2-II. The erasing magnetic field (H_e) in this case is not used. When the zone with a data-bearing domain (see the initial state of the magnetic structure in Fig. 2-IIa) is heated to a temperature close to the Curie point T_c of layer *2* (Fig. 1, region IV), this zone passes to a paramagnetic state and the direction of magnetization in the given zone of layer *3* is reoriented (due to the direct exchange interaction in the NiFe layer) in accordance with the magnetization of the surrounding material (leftward), thus passing to the equilibrium state (Fig. 2-IIb). On cooling, the zone in layer *2* will change the direction of magnetization to the opposite (due to the energy of exchange interaction with layer *3*) and the data-bearing domain will disappear (Fig. 2-IIc).

Since the magnetic field required for writing data ($H_w \geq (H_c + \Delta H) \approx 2 \times 10^3$ A/m) is much smaller than that used in [5] and the data erasing needs no magnetic field at all, the total magnetic field energy consumed for data writing/erasing is significantly reduced. Relatively low values of the magnetic field used for writing data allow the pulses of magnetic field H_w to be very short (several nanoseconds), which provides for a very high operating speed. The operating speed additionally increases because there is no need for commutation of the magnetic field during write/erase cycles. It should be noted that all the aforementioned advantages of

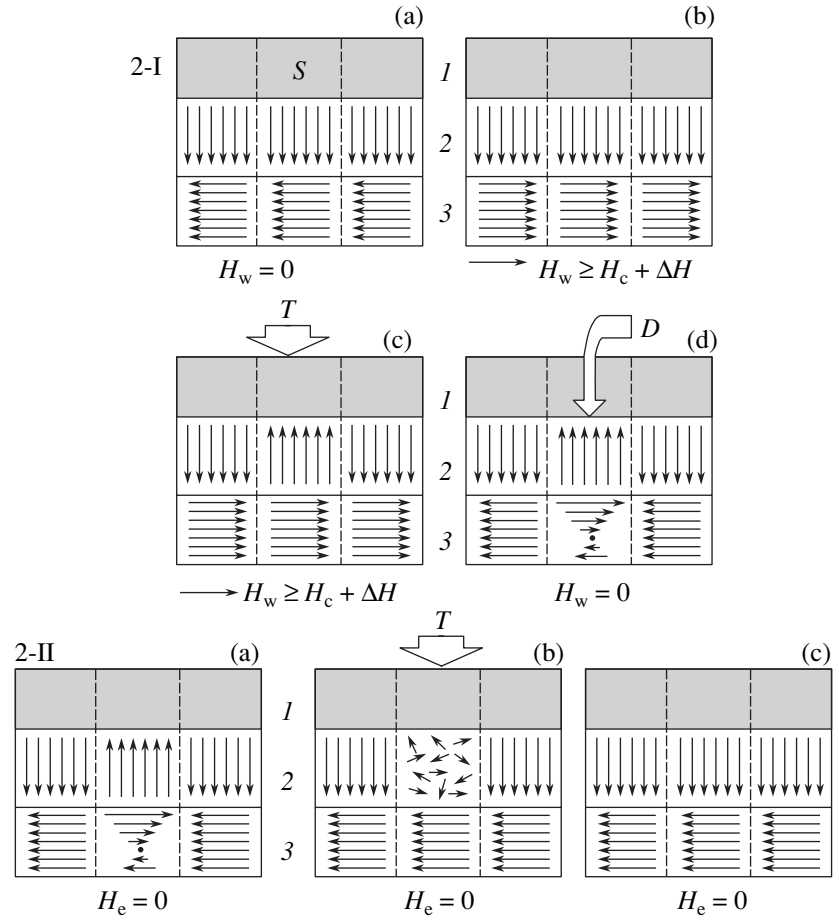

Fig. 2. Schematic diagrams illustrating the principles of writing (2-I) and erasing (2-II) of magnetooptical data in a bilayer DyCo/NiFe (TbFe/NiFe) film structure (see the text for explanations): (*S*) substrate; (*T*) heating; (*D*) domain.

REM–TM layers as the data recording media are retained.

In conclusion, the results of our investigations showed that the proposed (REM–TM)/NiFe film structures make possible the use of data writing and erasing principles different from the existing ones, which provides for a significant decrease in the energy consumed.

Acknowledgments. This study was supported in part by the Russian Foundation for Basic Research (project no. 04-02-16099a).

REFERENCES

1. V. A. Seredkin, G. I. Frolov, and V. Yu. Yakovchuk, Zh. Tekh. Fiz. **54**, 1183 (1984) [Sov. Phys. Tech. Phys. **29**, 674 (1984)].
2. S. Noboru, A. Yoshio, and M. Senri, *Int. Magn. Conf. INTERMAG-84, Hamburg, 1984*; IEEE Trans. Magn. **20** (5), Part 1, 1022 (1984).
3. W. H. Meiklejohn, Proc. IEEE **74**, 1570 (1986).
4. Xerox Corp. US Patent G11B13/04, No. 4,610,009 (1986).
5. S. N. Gadetskiĭ, N. V. Stupnov, M. V. Zyumkin, and E. N. Nikolev, Fiz. Tverd. Tela (St. Petersburg) **34**, 3019 (1992) [Sov. Phys. Solid State **34**, 1618 (1992)].
6. V. A. Seredkin, G. I. Frolov, and V. Yu. Yakovchuk, Pis'ma Zh. Tekh. Fiz. **9**, 1446 (1983) [Sov. Tech. Phys. Lett. **9**, 621 (1983)].
7. R. S. Iskhakov, V. Yu. Yakovchuk, S. V. Stolyar, *et al.*, Fiz. Tverd. Tela (St. Petersburg) **43**, 1462 (2001) [Phys. Solid State **43**, 1522 (2001)].
8. R. S. Iskhakov, V. A. Seredkin, S. V. Stolyar, *et al.*, Pis'ma Zh. Éksp. Teor. Fiz. **76**, 779 (2002) [JETP Lett. **76**, 656 (2002)].
9. V. A. Seredkin, R. S. Iskhakov, V. Yu. Yakovchuk, *et al.*, Fiz. Tverd. Tela (St. Petersburg) **45**, 882 (2003) [Phys. Solid State **45**, 927 (2003)].
10. B. P. Khrustalev and A. S. Mel'nik, Fiz. Met. Metalloved. **36**, 435 (1973).

Translated by P. Pozdeev

Technical Physics Letters, Vol. 30, No. 10, 2004, pp. 823–825. Translated from Pis'ma v Zhurnal Tekhnicheskoĭ Fiziki, Vol. 30, No. 19, 2004, pp. 53–58.

Radio-Frequency Properties of $La_{0.6}Sr_{0.2}Mn_{1.2}O_3$ and $La_{0.65}Sr_{0.28}Mn_{1.07}O_3$ Ceramics Near the Curie Temperature

A. N. Cherkasov*, A. I. Izotov, and V. Yu. Dmitrenko

Donetsk Physicotechnical Institute, National Academy of Sciences of Ukraine, Donetsk, Ukraine

** e-mail: cherkas@host.dipt.donetsk.ua*

Received April 2, 2004

Abstract—Radio-frequency magnetic and dissipative properties of $La_{0.6}Sr_{0.2}Mn_{1.2}O_3$ and $La_{0.65}Sr_{0.28}Mn_{1.07}O_3$ ceramics have been studied in the region of their Curie points. It is established that, despite relatively high conductivity in the frequency range f = 1–15 MHz, the screening of samples by the skin current is negligibly small and the ceramic samples behave like strong ferromagnets. This behavior is explained by significant differences in the propagation of electromagnetic field in inhomogeneous granular ferromagnetic media and normal metals. The field dependence of the effective magnetic susceptibility of both manganites has been studied at room temperature. © *2004 MAIK "Nauka/Interperiodica".*

Introduction. The interest in doped manganites of the $R_{1-x}A_xMnO_3$ system (where R is a rare earth element and A = Ba, Sr, Ca, etc.) is related to good prospects for practical application of these materials exhibiting a variety of unusual properties [1]. One of such remarkable properties of lanthanum manganites is the appearance of a metallic ferromagnetic phase in compositions in the region of x = 0.3, whereas the initial compound with x = 0 is a two-sublattice antiferromagnet. At the same time, the presence of excess manganese in undoped (x = 0) lanthanum manganites $La_{1-y}Mn_{1+y}O_3$ can also lead to the formation of a ferromagnetic phase [2].

This paper presents the results of our investigation of a series of strontium-doped lanthanum manganites in which the content of manganese was increased due to the La–Sr system: $(La_{1-x}Sr_x)_{1-y}Mn_{1+y}O_3$. The study was aimed mainly at determining the radio-frequency (RF) properties of compounds in a practically significant temperature range around room temperature. Interest was stimulated by the fact that ferromagnets can exhibit significantly different magnetic properties in the cases of remagnetization under quasi-static and dynamic conditions. Here, an important circumstance is the metallic type of conductivity of the ferromagnetic phase of manganites.

Experimental. The RF response of the manganite samples was studied using a setup employed previously for investigations of the surface impedance in metals [3]. We determined the oscillation frequency f and the losses introduced by samples into the circuit of the autodyne oscillator. The autodyne frequency was varied in the range f = 1–15 MHz. The external magnetic field **H** was directed along the axis of a cylindrical induction coil of the oscillator. The sample resistance was measured using the standard four-point-probe technique.

The manganites of $La_{0.6}Sr_{0.2}Mn_{1.2}O_3$ and $La_{0.65}Sr_{0.28}Mn_{1.07}O_3$ compositions were synthesized using standard ceramic technology and had densities of 5.67 g/cm^3 (porosity, ~12%) and 4.18 g/cm^3 (~34%), respectively. The measurements were performed on cylindrical samples with a diameter of 3.4 mm and a length of 12 mm. The reference samples of copper, iron, and nickel–zinc ferrite (400 NN) had the same dimensions. For the RF measurements, the samples were arranged on the axis of the induction coil.

Qualitative analysis. The induction L of a circuit with the current I is defined by the relation

$$\Phi = LI, \tag{1}$$

where Φ is the self-induction flux of the circuit. A sample placed into the circuit modifies the flux and, hence, changes the L value. In the case of alternating currents, the field penetrates into a conducting sample to within a skin layer with the thickness $\delta = (\rho/\pi\mu\mu_0 f)^{1/2}$, where ρ is the resistivity and μ is the relative magnetic permeability of the sample. Thus, the internal region of the sample behaves as the ideal diamagnet (μ = 0). As a result, the magnetic properties of the sample are characterized by an effective magnetic permeability μ_{eff}. Defining this effective characteristic by analogy with relation (1) as

$$L = L_0[1 + a(\mu_{eff} - 1)], \tag{2}$$

we obtain

$$a\chi_{eff} = f_0^2/f^2 - 1, \tag{3}$$

where $\chi_{eff} = \mu_{eff} - 1$ is the effective magnetic susceptibility of the sample; L_0 and f_0 are the induction and fre-

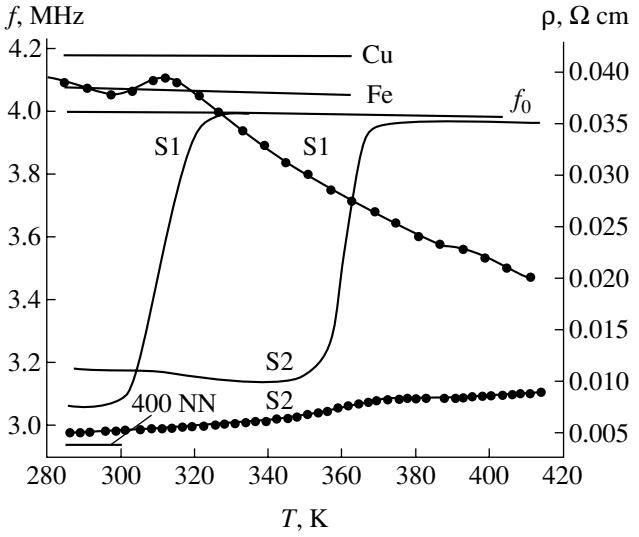

Fig. 1. Temperature dependences of the autodyne frequency f (thin solid curves for S1, S2, Fe, Cu, and 400 NN ferrite samples) and resistivity ρ (black circles for S1 and S2 samples); f_0 is the autodyne frequency in the absence of a sample.

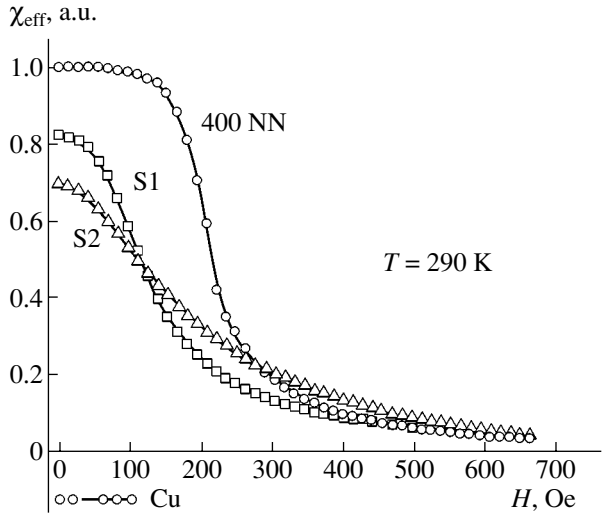

Fig. 2. The field dependence of the effective magnetic susceptibility χ_{eff} for strontium-doped lanthanum manganites (S1 and S2) and the reference (400 NN, Cu) samples.

quency of the autodyne circuit in the absence of the sample, respectively; and $a < 1$ is a parameter depending on the sample geometry and on the mutual arrangement of the sample and the induction coil.

In our experiments, the parameters μ_{eff} and χ_{eff} are differential characteristics describing remagnetization of the sample. The effective permeability was determined using the formula

$$\mu_{eff}\mu_0 \cong k(dB/dt), \quad (4)$$

where B is the magnetic induction on the internal surface of the sample, $k \cong \Delta S/S$ (if the skin layer thickness δ is much smaller than the sample diameter), S is the area of the sample cross section, and ΔS is the area of the skin layer. When δ increases, the coefficient k tends to zero ($k \longrightarrow 0$). Accordingly, introducing the effective magnetization M_{eff}, we have $\chi_{eff} = dM_{eff}/dH$. It should be noted that, in the case of $k \ll 1$, both k and μ_{eff} depend on frequency ($k \propto f^{-1/2}$).

Results and discussion. The results of the above qualitative analysis are illustrated in Fig. 1. As can be seen, ferrite ($\rho \sim 10^5$ Ω cm, $k \approx 1$) decreases the frequency of oscillations, while copper ($\rho \sim 10^{-6}$ Ω cm, $k \ll 1$) behaves as an almost ideal diamagnet ($\mu_{eff} \approx 0$) and increases the frequency; iron (despite being a ferromagnet) exhibits a competition of contributions from the core and skin layer and also behaves as a diamagnet ($\mu_{eff} < 1$). The value of μ_{eff} increases with decreasing frequency.

$La_{0.6}Sr_{0.2}Mn_{1.2}O_3$ (sample S1). As can be seen from Fig. 1, the $f(T)$ curve for this sample exhibits a clearly pronounced peculiarity at $T_c \approx 310$ K. At $T < T_c$, the sample behaves as a ferromagnet ($f < f_0$), while above T_c we have $f \longrightarrow f_0$. This peculiarity is also manifested in the $\rho(T)$ curve. The resistivity decreases with increasing temperature both below and above T_c, which is characteristic of dielectrics. Therefore, sample S1 at $T = T_c$ exhibits a phase transition from the ferromagnetic to a paramagnetic dielectric phase.

$La_{0.65}Sr_{0.28}Mn_{1.07}O_3$ (sample S2). In contrast to the analogous curves of $f(T)$, the curves of $\rho(T)$ for samples S1 and S2 are qualitatively different. For S2, the peculiarity observed at $T_c \approx 360$ K is manifested very slightly and the resistivity ρ slowly increases with the temperature T. Therefore, the phase transition in this sample can be identified as the transition from the ferromagnetic to a paramagnetic phase with the metallic type of conductivity in both phases.

Figure 2 shows the curves of $\chi_{eff}(H)$ determined according to relation (3). Assuming that copper has $\mu_{eff} \approx 0$, the absolute values of μ_{eff} at $T = 290$ K and $H = 0$ for the ferrite S1 and S2 samples can be evaluated as 14.5, 12.0, and 10.5, respectively. Therefore, the latter materials have χ on the order of 100 and above. It should be emphasized that μ_{eff} were virtually independent of the frequency f_0. The hysteresis observed during remagnetization in the external magnetic field was rather insignificant.

While the values of μ_{eff} and χ_{eff} of S1 and S2 are close to the corresponding parameters of the commercial ferrite, the dissipative characteristics of manganite ceramics are much worse. Figure 3 shows the temperature dependences of the effective losses $R_{eff} = R(f/f_0) \propto Q^{-1}$ in the manganites and reference materials. Here, R is the effective (with allowance for the introduced losses) resistance and Q is the quality factor of the circuit. As

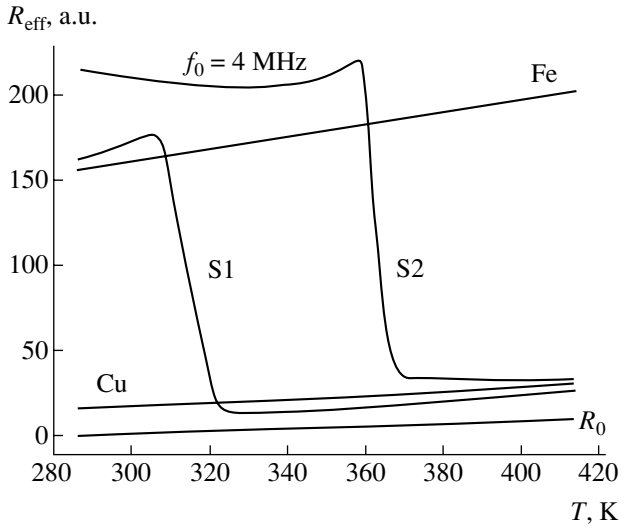

Fig. 3. Temperature dependences of the effective losses R_{eff} introduced into the oscillatory circuit by strontium-doped lanthanum manganites (S1 and S2) and the reference (Fe, Cu) samples; R_0 is the level of losses in the absence of a sample.

can be seen, both S1 and S2 reduce Q, while ferrite is characterized by $R_{eff} < R_0$.

Summarizing the obtained results, we can draw the following conclusions:

(i) In the RF range studied, the strontium-doped lanthanum manganites S1 and S2 behave as relatively strong magnetically soft ferromagnets.

(ii) At first glance, the absence of the dependence of μ_{eff} on f_0 is rather unexpected. Indeed, the skin layer thickness in S2 estimated using the formula presented above is $\delta \approx 0.1$–0.2 mm and the condition $k \ll 1$ is valid. However, this formula was derived from the Maxwell equations, which fail to describe the electromagnetic field distribution in ferromagnets in the general case. Another important circumstance is that the ceramic samples represent inhomogeneous granular media. For these reasons, the aforementioned formula describing the normal skin effect in nonferromagnets is inapplicable to the materials studied.

(iii) The absence of the dependence of μ_{eff} on f_0 also indicates that the frequency interval studied is far from any resonance frequencies and from the frequencies characterizing the relaxation times of both the component magnetic moments and the magnetic moment of the whole sample.

(iv) In the ferromagnetic phase, the main contribution to the total losses are those related to the hysteresis, which vanish upon transition to the nonferromagnetic phase. Above T_c, the losses are related predominantly to the vortex currents (Fig. 3).

Acknowledgments. The authors are grateful to V.P. Pashchenko and N.P. Pilipenko for kindly providing samples for this investigation.

REFERENCES

1. J. M. D. Coey, M. Viret, and S. von Molnar, Adv. Phys. **48**, 167 (1999).
2. V. P. D'yakonov, V. P. Pashchenko, É. E. Zubov, *et al.*, Fiz. Tverd. Tela (St. Petersburg) **45**, 870 (2003) [Phys. Solid State **45**, 914 (2003)].
3. L. T. Tsymbal, Yu. D. Samokhin, A. N. Cherkasov, *et al.*, Fiz. Nizk. Temp. **5**, 461 (1979).

Translated by P. Pozdeev

Technical Physics Letters, Vol. 30, No. 10, 2004, pp. 826–828. Translated from Pis'ma v Zhurnal Tekhnicheskoĭ Fiziki, Vol. 30, No. 19, 2004, pp. 59–64.

Anomalous Behavior of Silver in Polycrystalline Magnesia

A. R. Buev

Mari State University, Ioshkar Ola, Mari Republic, Russia

e-mail: bar48@yandex.ru

Received April 13, 2004

Abstract—The distribution of silver admixture in the bulk of polycrystalline magnesia-based ceramics has been studied after sintering at 1690°C. Silver was introduced into the composite in the form of oxide. The residual silver content exhibits anomalous behavior: as the initial silver oxide fraction in the composite is increased, the residual silver content first grows and then drops, so that silver is almost completely lost from a sintered material with the initial silver oxide fraction of 35–40% and above. The observed effects are explained based on the results of percolation and thermogravimetric measurements. A thick film of Bi2212 superconducting ceramics deposited onto the magnesia-based composite substrate with a 10% admixture of silver exhibited a 20% increase in the superconducting current density. *© 2004 MAIK "Nauka/Interperiodica".*

It is well known that an adequate substrate for thick films of high-temperature superconductors (HTSCs) of the Y123, Bi2212, and Bi2223 systems is offered by magnesia-based ceramics (see, e.g., [1]). This study was aimed at the development of a polycrystalline magnesia with a silver-doped pore-free surface offering an optimum substrate for depositing thick films (coatings). Owing to the general positive influence of silver on the above HTSCs (see, e.g., [2, 3]), it was expected that the silver-doped substrates, while retaining the HTSC stoichiometry in the near-surface layer, will improve adhesion and increase the superconducting properties throughout the HTSC film thickness. Direct deposition of silver onto the surface of sintered magnesia-based ceramics does not ensure achievement of these goals. Experiments showed that molten silver (961°C) exhibits neither wetting nor adhesion to polycrystalline magnesia. Silver tends to coalesce into coarse drops and is virtually not retained on the substrate surface.

In order to obtain silver-doped surface, we have introduced silver into the bulk of substrate. For this purpose, silver oxide was added to the initial powdered magnesia in an amount of 5–55 wt %. Upon adding a binding agent, the charge was homogenized and pressed into tablets. The tablets were sintered in air according to the following regime: heating to 450°C at a rate of 2 K/min; keeping at 450°C for 2 h; heating to 1690°C at a rate of 5 K/min; keeping at 1690°C for 10 h; cooling with the furnace.

An analysis of the distribution of silver in the bulk of the composite, which is clearly manifested in the photographs of transverse sections of the samples (Fig. 1) revealed the following peculiarities:

(i) Silver vanishes from the surface layer.

(ii) Silver tends to concentrate inside the sample in the form of a layer whose width and contrast depend on the initial content of silver oxide (δ_{Ag_2O}): the layer width increases for $0 \le \delta_{Ag_2O} \le 15$–$20\%$ and decreases for 15–$20\% \le \delta_{Ag_2O} \le 55\%$.

(iii) Beginning at $\delta_{Ag_2O} = 35$–40%, silver is lost from the samples. The loss rate rapidly increases and, at $40\% \le \delta_{Ag_2O} \le 55\%$, silver is virtually not retained in the samples.

In order to elucidate this behavior, we performed the following investigations.

(1) Determination of silver weight loss. The samples were weighed before and after sintering and the experimental results were plotted as δ_{Ag} versus δ_{Ag_2O} (Fig. 2). The curve was constructed using the formula

$$\delta_{Ag} = (0.067 + 1.007\delta_{Ag_2O} + 1.074\Delta m/m)/\delta_{Ag_2O},$$

where $\delta_{Ag} = m'_{Ag}/m_{Ag}$ is the residual relative silver con-

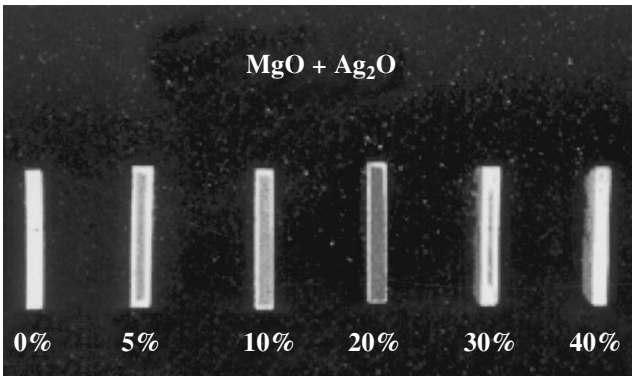

Fig. 1. Photographs of the transverse sections of ceramic samples with various δ_{Ag_2O} upon sintering.

1063-7850/04/3010-0826$26.00 © 2004 MAIK "Nauka/Interperiodica"

tent, $\delta_{Ag_2O} = m_{Ag_2O}/m$, $\Delta m = m - m'$, m'_{Ag} (m_{Ag}) is the silver mass after (before) sintering, m_{Ag_2O} is the mass of silver oxide in the sample before sintering, and m (m') is the sample mass before (after) sintering. This formula was derived with allowance for the oxygen release from silver oxide and the weight loss of magnesium oxide in the course of sintering (determined by weighing control samples of pure magnesia with $\delta_{Ag_2O} = 0$ before and after sintering). As can be seen from Fig. 2, silver is most completely retained (85–95% of the initial content) in the samples with δ_{Ag_2O} = 15–25%. For δ_{Ag_2O} = 30–55%, the fraction of retained silver rapidly drops from 50–60% to almost zero. The established dependence agrees well with the above conclusions (i)–(iii) drawn from the analysis of transverse sections.

(2) Differential thermal analysis (DTA) and thermogravimetric (TG) measurements. In the temperature range from 50 to 1600°C, DTA reveals no exo- or endothermal reactions between magnesium and silver. The results of TG measurements for the samples with various δ_{Ag_2O} are presented in Fig. 3.

(3) Measurement of the electric resistance R of the samples with various δ_{Ag_2O}. The samples with various δ_{Ag_2O} were annealed at 965°C in order to reduce and melt silver particles. The resistance was measured using columns of the same shape cut from each sample. These measurements showed that $R > 20$ MΩ for $0 \le \delta_{Ag_2O} \le 30\%$; $R \approx 10$ Ω for δ_{Ag_2O} = 35 and 40%; and $R \approx 1$ Ω for δ_{Ag_2O} = 45, 50, and 55%.

The results of weight loss, DTA–TG, and electric resistance measurements allow us to give the following interpretation of peculiarities (i)–(iii) in the distribution of silver. The particles of silver oxide heated to 1690°C lose oxygen and convert into molten metallic silver droplets. Sintering of the magnesia charge results in the formation of a ceramic matrix with pores partly filled with silver. For $\delta_{Ag_2O} < 35$–40%, separate silver particles are distributed over the matrix volume and sintering at 1690°C leads to their evaporation only from a near-surface layer. This explains the appearance of bright edges in the transverse sections of samples (Fig. 1). The near-surface layer of ceramics prevents silver evaporation from the bulk.

When δ_{Ag_2O} = 35–40% and percolation takes place, molten silver particles merge into continuous wires emerging at the sample surface, which is confirmed by the results of resistance measurements. Transferred along these wires, liquid silver can readily and almost completely escape from the bulk. According to Fig. 3, the temperature of 1270–1280°C corresponding to the onset of rapid weight loss (silver escape) is almost the same for the samples with different δ_{Ag_2O}. Calculations showed that the rate of weight loss for the samples with various silver contents in the linear (>1400°C) regions of TG curves are proportional to δ_{Ag_2O}. This result agrees well with the above explanation for the observed behavior. The fact of equal temperature corresponding to the onset of rapid silver escape from the ceramic matrix with various silver contents and the value of this temperature are worthy of thorough analysis. This temperature is apparently related to the viscosity of silver and the initial size of silver oxide and magnesia particles (i.e., with capillary effects). At temperatures below 1270–1280°C, silver is prevented from rapid evaporation by surface tension.

The results of our experiments do not offer an unambiguous explanation for the second peculiarity and the corresponding extremum in the curve of δ_{Ag} versus

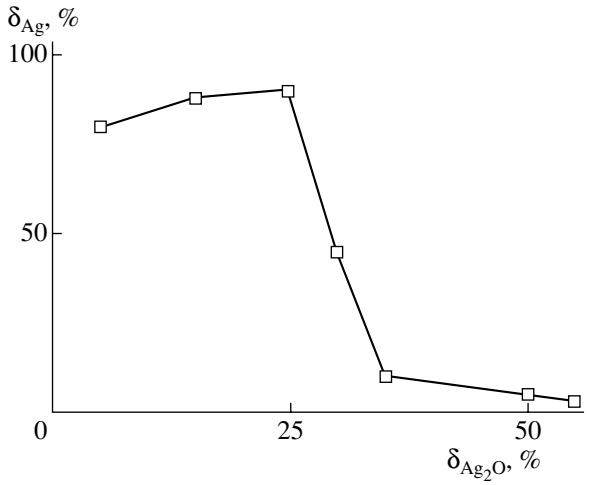

Fig. 2. Experimental plot of δ_{Ag} versus δ_{Ag_2O}.

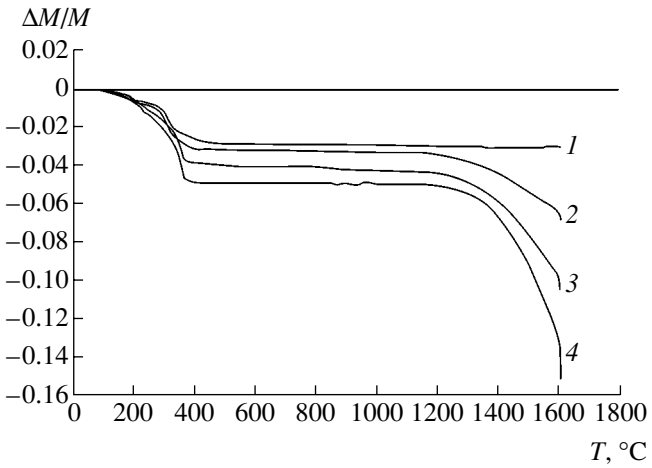

Fig. 3. TG curves of (*1*) silver-free and (*2–4*) silver-doped magnesia ceramics with δ_{Ag_2O} = 15 (*2*), 30 (*3*), and 40% (*4*).

δ_{Ag_2O} (Fig. 2), but there is reason to suggest that this behavior is also related to capillary effects.

The experiments showed that using pure silver powder instead of silver oxide leads to analogous results. The situation was generally the same for an alumina-based ceramics with copper oxide additives sintered at the same temperature.

The results of our experiments showed that ceramic substrates with silver-doped surface could not be obtained by directly introducing silver in the bulk because silver is lost from the surface during sintering (Fig. 1). The required substrate surface was obtained by grinding-off the surface layer, followed by etching and rapid (for several minutes) firing at 1690°C. As a result of this treatment, the samples with δ_{Ag_2O} = 10% exhibited a defectless homogeneous surface with pores filled by silver and a magnesia grain size of 100–150 μm. Superconducting Bi2212 coatings with a thickness of 50 μm deposited by the paste technique and sintered in a nearly standard regime [1] exhibited a critical current density of 2500 A/cm^2, which was 20% higher than the value in control samples formed on silver-free magnesia substrates.

REFERENCES

1. D. Buhl, T. Land, and L. J. Gaucker, Supercond. Sci. Technol. **10**, 32 (1997).
2. V. V. Sagaradze, Yu. A. Kotov, V. L. Arbuzov, *et al.*, Sverkhprovodimost **4**, 1964 (1991).
3. A. Y. Ilyushechkin, T. Yamashita, J. A. Alarco, and I. D. R. Mackinnon, Supercond. Sci. Technol. **10**, 330 (1997).

Translated by P. Pozdeev

Technical Physics Letters, Vol. 30, No. 10, 2004, pp. 829–831. Translated from Pis'ma v Zhurnal Tekhnicheskoĭ Fiziki, Vol. 30, No. 19, 2004, pp. 65–71.

The Equation of State for Magnesium at High Pressures

K. V. Khishchenko

Institute for High Energy Densities, Associated Institute for High Temperatures, Russian Academy of Sciences, Moscow, Russia

e-mail: konst@ihed.ras.ru

Received April 21, 2004

Abstract—A caloric model of the equation of state is presented, which allows the properties of substances to be described in a broad range of densities and pressures. A new method for determining the curve of cold compression at $T = 0$ K is proposed. The thermodynamic characteristics of magnesium calculated using the proposed model are compared to the experimental data available for high energy densities. © *2004 MAIK "Nauka/Interperiodica".*

Magnesium and related low-density alloys are widely used in modern technology as structural materials for the constructions and parts working under extremal conditions involving high mechanical and thermal loads. Magnesium is also frequently used in shock-wave experiments as a reference substance with low dynamic impedance (typical of dense polymeric materials such as Teflon).

This paper presents a caloric equation of state for magnesium, $E = E(P, V)$, which provides adequate description of the properties of its condensed phase in a broad range of densities and pressures. This equation is applicable to hydrodynamic calculations of the adiabatic processes at high energy densities. In contrast to the semiempirical equations of state derived for this metal previously [1–4], the proposed equation provides for a new method of determining the curve of cold compression at $T = 0$ K.

A caloric model of the equation of state adopted for description of the thermodynamic properties of substances is formulated in the general form as

$$P(V, E) = P_c(V) + \frac{\Gamma(V, E)}{V}[E - E_c(V)], \qquad (1)$$

where $E_c(V)$ and $P_c(V) = -dE_c/dV$ are the elastic components of energy and pressure at $T = 0$ K and $\Gamma(V, E)$ is a coefficient determining the contributions of thermal components to the equation of state.

The volume dependence of the elastic interaction energy under compression $\sigma_c \geq 1$ ($\sigma_c = V_{0c}/V$, V_{0c} is the specific volume at $P = 0$ and $T = 0$ K) is set by the relation

$$E_c(V) = a_0 V_{0c} \ln\sigma_c - 3V_{0c}\sum_{i=1}^{3}\frac{a_i}{i}(\sigma_c^{-i/3} - 1) + 3V_{0c}\sum_{i=1}^{2}\frac{b_i}{i}(\sigma_c^{i/3} - 1), \qquad (2)$$

with the normalization

$$E_c(V_{0c}) = 0. \qquad (3)$$

As can be readily seen, differentiation of the energy (2) with respect to volume yields an equation for the pressure $P_c(V)$, which is analogous to the relation proposed previously [5] as an expansion of the Thomas–Fermi model in powers of the atomic cell radius $r_c \sim \sigma_c^{-1/3}$.

The values of coefficients b_i in relation (2) are determined from the condition of coincidence with the Thomas–Fermi model (with both quantum and exchange corrections [6]) in the range of compressions above $\sigma_c \sim 10^3$–10^4:

$$b_1 = -\left[Z^2\frac{3}{10}(4\pi/3)^{1/3} + Z^{4/3}\frac{11}{36}(3/\pi)^{1/3}\right] \times a_B E_H (A m_u V_{0c})^{-4/3},$$

$$b_2 = Z^{5/3}\frac{1}{5}(3\pi^2)^{2/3} a_B^2 E_H (A m_u V_{0c})^{-5/3},$$

where E_H is the Hartree energy, a_B is the Bohr atomic radius, m_u is the atomic mass unit (amu), A is the atomic mass (in amu), and Z is the atomic number of an element.

The coefficients a_i are determined from the following conditions for the pressure, hydrostatic modulus and its first and second derivatives at $\sigma_c = 1$:

$$P_c(V_{0c}) = 0, \qquad (4)$$

$$B_c(V_{0c}) = -VdP_c/dV = B_{0c}, \qquad (5)$$

$$B_c'(V_{0c}) = dB_c/dP_c = B_{0c}', \qquad (6)$$

$$B_c''(V_{0c}) = -d(VdB_c/dV)/dB_c = B_{0c}''. \qquad (7)$$

1063-7850/04/3010-0829$26.00 © 2004 MAIK "Nauka/Interperiodica"

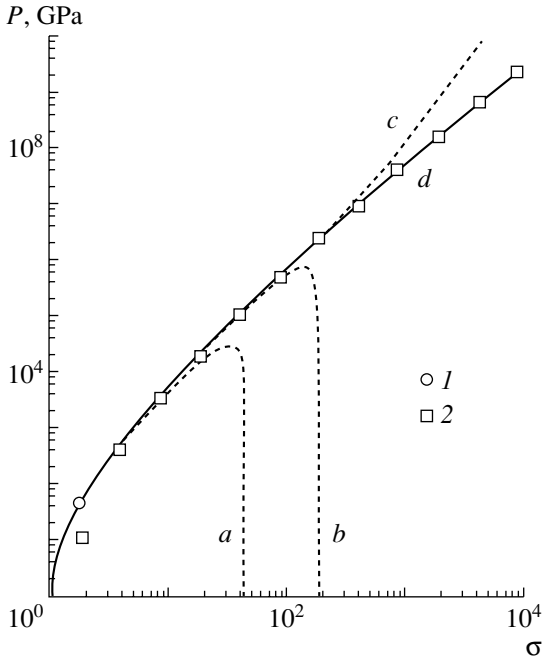

Fig. 1. The diagram of pressures on the elastic cold compression curve (T = 0 K) approximated by curves constructed according to (*a*) [1], (*b*) [2], (*c*) [3, 4, 11], and (*d*) this study; (*1*) experiment [12]; (*2*) calculation [6].

Here, the parameters V_{0c}, B_{0c}, and B'_{0c} are selected by iterations so as to obtain the tabulated specific volume V_0, the isoentropic compression modulus $B_S = -V(\partial P/\partial V)_S = B_{S0}$, and its pressure derivative $B'_S = (\partial B_S/\partial V)_S = B'_{S0}$ under normal conditions, as determined from the results of static and dynamic measurements. Condition (7) provides for a monotonic character of the pressure interpolation curve, which can be violated by alternating signs of a_i in the case of negative B''_{0c}.

The energy on the cold compression curve in the region of rarefaction ($\sigma_c < 1$) is set by the polynomial [7]

$$E_c(V) = V_{0c}[a_m(\sigma_c^m/m - \sigma_c^l/l) + a_n(\sigma_c^n/n - \sigma_c^l/l)] + E_{sub}, \quad (8)$$

which provides for a tabulated value [8] of the sublimation energy $E_c = E_{sub}$ at $V \longrightarrow \infty$ and for the equality (4). Note that conditions (3), (5), and (6) leave only two free parameters, l and n, in expression (8).

The dependence of the coefficient Γ on the volume and energy is defined (by analogy with the caloric model [3, 9]) in the following form:

$$\Gamma(V, E) = \gamma_i + \frac{\gamma_c(V) - \gamma_i}{1 + \sigma^{-2/3}[E - E_c(V)]/E_a}, \quad (9)$$

where $\sigma = V_0/V$, $\gamma_c(V)$ corresponds to the case of low thermal energies, and γ_i characterizes the region of strongly heated condensed substance. The anharmonicity energy E_a, which sets the thermal energy of a transition from one limiting case to another, is determined from the results of dynamic experiments at high pressures.

The volume dependence of the elastic component of the coefficient Γ is set as [10]

$$\gamma_c(V) = 2/3 + (\gamma_{0c} - 2/3)\frac{\sigma_n^2 + \ln^2\sigma_m}{\sigma_n^2 + \ln^2(\sigma/\sigma_m)}, \quad (10)$$

where

$$\gamma_{0c} = \gamma_i + (\gamma_0 - \gamma_i)\left[1 + \frac{E_0 - E_c(V_0)}{E_a}\right]^2,$$

and E_0 and γ_0 are the specific internal energy and the Grüneisen coefficient $\gamma = V(\partial P/\partial E)_V$ under normal conditions. As can be readily seen, the adopted form of $\gamma_c(V)$ ensures validity of the condition $\gamma(V_0, E_0) = \gamma_0$ and gives the asymptotic value $\gamma_c = 2/3$ in the limiting cases of low and high degrees of compression. The fitting parameters σ_n and σ_m in relation (10) are determined from the condition of optimum fitting to the experimental data on the dynamic compressibility of porous samples and the isoentropic unloading of a given substance.

The coefficients in the equation of state providing optimum generalization of the available thermodynamic data for magnesium within the framework of the caloric model described by Eqs. (1)–(10) are as follows: V_0 = 0.5747; V_{0c} = 0.5668; a_0 = 3785.043; a_1 = –2034.798; a_2 = –97.789; a_3 = 317.442; b_1 = –2766.977; b_2 = 797.079; a_m = 15.133; a_n = –0.904; m = 3.975; n = 12; l = 1; E_{sub} = 5.95; γ_{0c} = 1.45; σ_m = 0.5; σ_n = 1; γ_i = 0.5; and E_a = 20. The units of measure correspond to the initial units of P = 1 GPa; V = 1 cm^3/g; and E = 1 kJ/g.

The elastic compression curve presented in Fig. 1 characterizes the accuracy of calculations of the thermodynamic characteristics of magnesium at T = 0 K. As can be seen from these data, the approximation relations proposed previously for $P_c(\sigma)$ [1–4, 11] are applicable in the region of compressions $\sigma \lesssim 200$ and lead to large errors or nonphysical results at higher densities. It should be noted that the applicability of relation (2) is restricted to the range of energies in which the motion of electrons can be considered as nonrelativistic [13]: $5Am_uE_c/(3Z) \ll m_ec^2$ (m_e is the electron mass and c is the speed of light). This condition can be rewritten as $\sigma^{2/3} \ll 2Zm_ec^2/(5Am_uV_{0c}b_2)$, which yields the following limit of applicability with respect to the degree of compression for the cold compression curve of magnesium obtained in this study: $\sigma \ll 3 \times 10^6$.

The diagram in Fig. 2 shows the entire range of the high-energy-density states of magnesium, which was

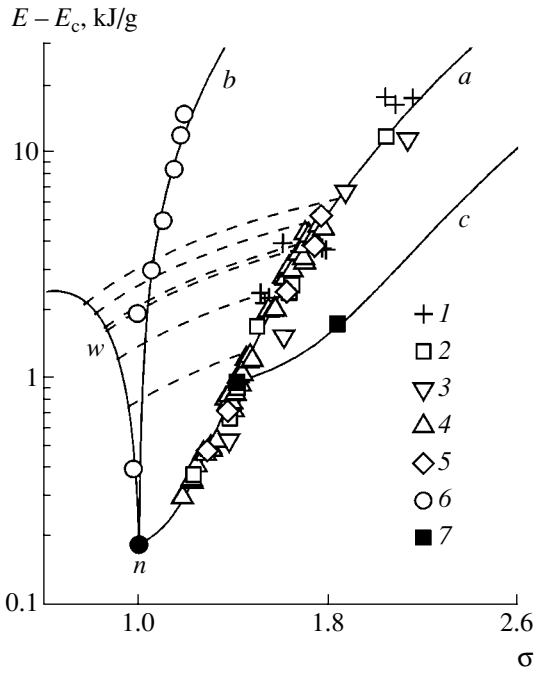

Fig. 2. The diagram of state for magnesium at high specific thermal energies: (*a*, *b*) shock adiabates for the samples with the initial porosity $m = \rho_0/\rho_{00} = 1$ and 2.096, respectively ($\rho_0 = 1/V_0$; ρ_{00} is the initial density); (*c*) the curve of repeated loading; (*w*) the line of final states upon adiabatic unloading into air for shock-compressed solid samples; (dashed curves) isoentropic expansion curves corresponding to experimental data [21]; (*n*) normal state. Experimental data: (*1*) [14]; (*2*) [15]; (*3*) [16]; (*4*) [17]; (*5*) [18]; (*6*) [19]; (*7*) [20].

studied under conditions of the shock compression of solid [14–18] and porous [19] samples, the oblique collision of shock waves [20], and the adiabatic unloading into air [21]. A comparison of the results of calculations and the experimental data [14–21] shows that the proposed equation of state ensures a reliable description of the metal parameters in the entire range of compressions ($0.7 \lesssim \sigma \lesssim 2.2$) and specific thermal energies ($E - E_c(\sigma) \lesssim 20$ kJ/g) studied in experiment.

Acknowledgments. The author is grateful to I.V. Lomonosov for his interest in this study, fruitful discussions, and valuable remarks.

This study was supported by a Presidential Grant of the Russian Federation (project no. MK-2103.2003), the Russian Foundation for Basic Research (project no. 03-02-16687), and the Foundation for Support of Russian Science.

REFERENCES

1. S. V. Kormer and V. D. Urlin, Dokl. Akad. Nauk SSSR **131**, 542 (1960) [Sov. Phys. Dokl. **5**, 317 (1960)].
2. S. B. Kormer, V. D. Urlin, and L. T. Popova, Fiz. Tverd. Tela (Leningrad) **3**, 2131 (1961) [Sov. Phys. Solid State **3**, 1547 (1961)].
3. A. V. Bushman, V. E. Fortov, and I. V. Lomonosov, in *High Pressure Equations of State: Theory and Applications*, Ed. by S. Eliezer and R. A. Ricci (North Holland, Amsterdam, 1991), pp. 249–262.
4. A. V. Bushman, I. V. Lomonosov, and V. E. Fortov, *Equations of State for Metals at High Energy Densities* (Institute of Chemical Physics, Chernogolovka, 1992) [in Russian].
5. N. N. Kalitkin and I. A. Govorukhina, Fiz. Tverd. Tela (Leningrad) **7**, 355 (1965) [Sov. Phys. Solid State **7**, 287 (1965)].
6. N. N. Kalitkin and L. V. Kuz'mina, IPM AN SSSR Preprint No. 35 (Keldysh Institute of Applied Mathematics, USSR Academy of Sciences, Moscow, 1975) [in Russian].
7. A. V. Bushman and V. E. Fortov, Sov. Technol. Rev. B: Thermal Physics **1**, 219 (1988).
8. R. Hultgren, P. D. Desai, D. T. Hawkins, M. Gleiser, *et al.*, *Selected Values of the Thermodynamic Properties of the Elements* (ASM, Metals Park, Ohio, 1973).
9. A. V. Bushman and I. V. Lomonosov, in *Studying the Properties of Substances under Extremal Conditions*, Ed. by V. E. Fortov and E. A. Kuz'menkov (IVTAN, Moscow, 1990), pp. 34–40 [in Russian].
10. A. V. Bushman, M. V. Zhernokletov, I. V. Lomonosov, *et al.*, Zh. Éksp. Teor. Fiz. **109**, 1662 (1996) [JETP **82**, 895 (1996)].
11. I. V. Lomonosov, Doctoral Dissertation (Institute of Problems of Chemical Physics, Russian Academy of Sciences, Chernogolovka, 1999).
12. H. Olijnyk and W. B. Holzapfel, Phys. Rev. B **31**, 4682 (1985).
13. D. A. Kirzhnits, Usp. Fiz. Nauk **104**, 489 (1971) [Sov. Phys. Usp. **14**, 512 (1971)].
14. I. C. Skidmore and E. Morris, in *Thermodynamics of Nuclear Materials* (IAEA, Vienna, 1962), pp. 173–216.
15. L. V. Al'tshuler, A. A. Bakanova, and I. P. Dudoladov, Zh. Éksp. Teor. Fiz. **53**, 1967 (1967) [Sov. Phys. JETP **26**, 1115 (1967)].
16. W. H. Isbell, F. H. Shipman, and A. H. Jones, Report No. MSL-68-13 (General Motors Corp., Mat. Sci. Lab., 1968).
17. *LASL Shock Hugoniot Data*, Ed. by S. P. Marsh (Univ. California, Berkeley, 1980).
18. L. V. Al'tshuler, A. A. Bakanova, I. P. Dudoladov, *et al.*, Prikl. Mekh. Tekh. Fiz., No. 2, 3 (1981).
19. R. F. Trunin, G. V. Simakov, Yu. N. Sutulov, *et al.*, Zh. Éksp. Teor. Fiz. **96**, 1024 (1989) [Sov. Phys. JETP **69**, 580 (1989)].
20. L. V. Al'tshuler and A. P. Petrunin, Zh. Tekh. Fiz. **31**, 717 (1961) [Sov. Phys. Tech. Phys. **6**, 516 (1961)].
21. A. A. Bakanova, I. P. Dudoladov, M. V. Zhernokletov, *et al.*, Prikl. Mekh. Tekh. Fiz., No. 2, 76 (1983).

Translated by P. Pozdeev

Technical Physics Letters, Vol. 30, No. 10, 2004, pp. 832–835. Translated from Pis'ma v Zhurnal Tekhnicheskoĭ Fiziki, Vol. 30, No. 19, 2004, pp. 72–79.

Coadsorption of Aluminum and Group IV (Si, C) Atoms on W(100) Surface

N. R. Gall*, E. V. Rut'kov, and A. Ya. Tontegode

Ioffe Physicotechnical Institute, Russian Academy of Sciences, St. Petersburg, 194021 Russia

** e-mail: gall@ms.ioffe.rssi.ru*

Received April 28, 2004

Abstract—Electropositive atoms of aluminum adsorbed on a W(100) surface exhibit competition with silicon adatoms for the adsorption sites at high temperatures (1200–1500 K). In this system, silicon displaces aluminum from the tungsten surface. No such competition is observed during the coadsorption of aluminum and carbon, where adatoms of both elements coexist on the tungsten surface (in contrast to the situation previously observed on rhenium, where aluminum atoms displaced carbon to the bulk of substrate). The nature of competition in the systems studied is apparently analogous to that observed previously for Si, C, and S atoms on W(100), despite the fact that aluminum atoms (in contrast to the nonmetals) in the adsorbed state possess a positive charge. © *2004 MAIK "Nauka/Interperiodica".*

Previously, repeated observations showed that nonmetal atoms of groups IV, V, and VI during high-temperature coadsorption on a refractory metal surface are capable of competing for adsorption sites [1–8]. This competition leads to various phenomena such as the displacement of one adsorbate by another from the surface to the bulk of substrate with the formation of a solid solution (e.g., in Si–C and C–S systems on W, Re, and Mo [1–4]) or the simultaneous removal of two adsorbates (e.g., of Si and S adatoms jointly desorbed from the same substrates in the form of SiS molecules [5, 6]). Aluminum atoms possess a low ionization potential and, in contrast to the aforementioned nonmetals, probably acquire a positive charge in the adsorbed state on refractory metals [9]. On the other hand, the properties of the bulk aluminides of tungsten, rhenium, molybdenum, and iridium have much in common with the properties of oxides, carbides, and especially silicides of these metals [10].

Previously [8], we demonstrated that aluminum atoms in fact entered into competition with silicon and carbon adatoms during coadsorption on a Re($10\bar{1}0$) surface. However, it remained unclear if the observed behavior had a general character and it was difficult to predict how aluminum atoms will behave during their joint adsorption with nonmetals on a much more chemically and catalytically active [11] W(100) surface at temperatures sufficiently high to ensure great mobility of adatoms and render them capable of entering into chemical reactions and penetrating into the bulk of substrate.

Experimental. The experiments were performed under ultrahigh vacuum (UHV) conditions ($p \sim 1 \times 10^{-10}$ Torr) in a high-resolution ($\Delta E/E < 0.1\%$) Auger electron spectrometer with a prism electron energy analyzer described elsewhere [12]. The instrument allowed the Auger electron spectra to be measured in situ on a sample heated to any temperature in the range from 300 to 2200 K. The substrates were thin tungsten ribbons with dimensions of $0.02 \times 1 \times 40$ mm, which were thoroughly cleaned from possible impurities by high-temperature annealing in an oxygen atmosphere and under UHV conditions. The ribbon surface texture for more than 99.5% represented a (100) single crystal face, the average grain size being ~30 μm. The sample surface was homogeneous with respect to the work function ($e\varphi = 4.65$ eV).

All adsorbates were deposited onto the substrate surface in situ under UHV conditions: Si atoms, by sublimation from a silicon ribbon; At atoms, by evaporation from a specially designed source [8]; and C atoms, by thermal decomposition of fullerenes (C_{60}) deposited onto a heater from a Knudsen cell. The absolute atomic flux densities of the three adsorbates were determined using the methods described earlier [12–14]. The measurements were performed for the following Auger electron peaks: C *KVV* (E = 272 eV); Si *LVV* (92 eV); Al *LVV* (63 eV); and a triplet of W lines (160–178 eV). Proximity of the kinetic energies of the Auger electrons emitted from of Si, W, and C implies that their mean free paths and, hence, the degrees of intensity attenuation for the same adlayer thickness are close.

Interaction of aluminum with a W(100) surface. We failed to find published data on the interaction of aluminum atoms with a tungsten surface. The deposition of aluminum onto W(100) at high temperatures (1150–1300 K) leads to the formation of a thermally stable adsorption state with the surface concentration of Al atoms independent of the flux density and the substrate temperature (in the indicated interval). We call

this state surface aluminide by analogy with the surface aluminide of rhenium [14, 15]. All aluminum atoms delivered to the substrate surface at $T > 1150$–1300 K at an amount below or equal to that necessary for the formation of surface aluminide are retained on the surface, while the atoms supplied in excess of this amount are dissolved in the bulk of substrate. The concentration of Al adatoms in the surface aluminide layer estimated using quantitative Auger electron spectroscopy (AES) data is $N_{Al} = (1.0 \pm 0.15) \times 10^{15}$ cm^{-2}. The relative composition of this layer determined with respect to metal atoms of the uppermost layer of the substrate is WAl. The surface aluminide layer decomposes only during thermal desorption at $T > 1400$ K.

Interaction of Si and C atoms with a W(100) surface. The deposition of silicon atoms onto tungsten at 1100–1400 K leads to the formation of surface silicide with a relative composition of WSi and a surface atomic density of $N_{Si} = 1.0 \times 10^{15}$ cm^{-2} [1, 4]. This surface silicide forms via the same mechanism as that mentioned above for surface aluminide: unless the surface compound is formed, all deposited Si atoms are retained on the surface of tungsten, while all atoms adsorbed after that are dissolved in the bulk of substrate.

The formation of surface carbides on tungsten is a more complicated process with participation of a segregation mechanism, whereby both a W–C solid solution phase and a surface coverage by carbon are formed simultaneously. Dissolution of approximately four monolayers (ML) of carbon in a ribbon sample with dimensions specified above leads to the formation of a surface carbide with the composition corresponding to WC [16, 17]. This carbide is thermally stable at temperatures up to $T = 1500$ K, independently of the amount of carbon dissolved in the bulk of substrate in excess of the above amount (4–200 ML). At $T > 1500$ K, surface carbide exhibits reversible dissolution in the bulk and emerges on the surface again upon cooling.

Thus, all three of the elements studied form high-temperature surface compounds of the same stoichiometry when adsorbed on tungsten: WC, WSi, and WAl. During the coadsorption of Si and C at 1300–1400 K, carbon is displaced by silicon from the surface into bulk, where C atoms occur in a dissolved state [1, 4].

Coadsorption of aluminum and silicon on W(100). Figure 1 shows evolution of the Auger signals from both adsorbates in the course of silicon deposition onto surface aluminide at 1200 K. Since both adsorbates occur in the form of surface compounds, the signal intensity is directly proportional to the surface concentration of the corresponding element. As can be seen, every sequential dose of adsorbed silicon leads to a decrease in intensity of the response from aluminum. When silicon is deposited in an amount corresponding to surface silicide, the Auger signal from aluminum almost completely vanishes. This cannot be explained by the screening effect: the same dose of silicon deposited onto the surface aluminide layer at room temperature attenuates the Auger signal from aluminum only by a factor of ~1.3. Therefore, the only possible explanation consists in that silicon deposited at 1200 K displaces aluminum from the tungsten surface by analogy with the effect observed previously for the same elements on rhenium [8].

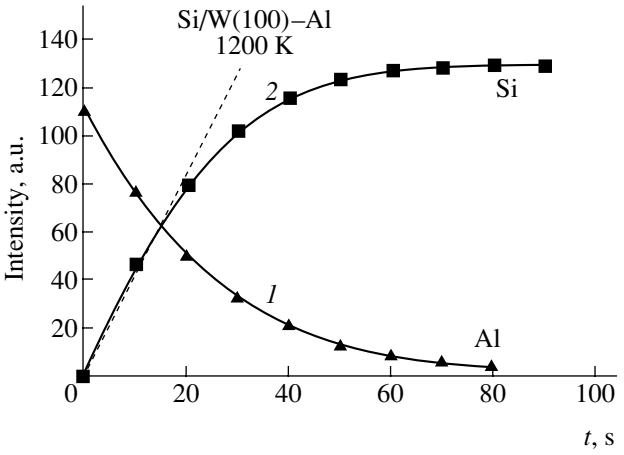

Fig. 1. Variation of the intensity of the Auger signal of (*1*) aluminum and (*2*) silicon during deposition of Si atoms onto surface aluminide WAl at 1200 K. The flux density of silicon $\nu_{Si} = (1.8 \pm 0.3) \times 10^{13}$ cm^{-2} s^{-1}. The AES measurements were performed at the temperature of adsorption.

It should also be noted that the curves of silicon deposition onto a clean tungsten surface and onto that with an aluminum adlayer coincide with very high accuracy, which implies that silicon atoms behave as if there were no adsorbed aluminum. Calculations showed that the total surface atomic density of both adsorbates remains virtually constant, so that the amount of displaced aluminum is exactly that required for providing the necessary adsorption sites for the deposited silicon atoms.

It was interesting to consider an intermediate situation, whereby silicon deposition is halted when Si atoms are accumulated on the surface in an amount corresponding to half of that in surface silicide. In this state, the total adsorbate concentration reaches $N_\Sigma = (1.0 \pm 0.15) \times 10^{15}$ cm^{-2} and the isothermal annealing at 1200–1300 K for many hours (and probably longer) does not show evidence of one adsorbate being displaced by another.

The reverse order of adsorption, whereby aluminum is deposited art 1200–1300 K onto tungsten covered with surface silicide, does not lead to the accumulation of aluminum even in small amounts on the metal substrate. Note that, in the absence of silicon, all Al atoms striking the substrate are retained in the adlayer until reaching a coverage corresponding to the formation of surface aluminide.

The experiments described above do not allow us to judge unambiguously on the way in which aluminum atoms are displaced by silicon, distinguishing between their desorption and dissolution in the bulk of tungsten.

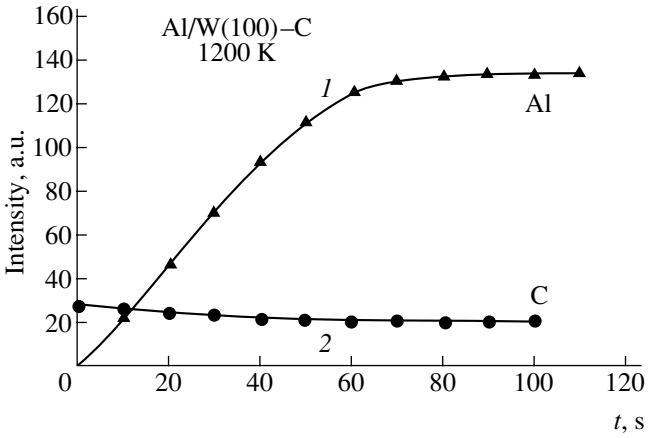

Fig. 2. Variation of the intensity of the Auger signal of (*1*) aluminum and (*2*) carbon during deposition of Al atoms onto surface carbide WC at 1200 K. The flux density of aluminum $\nu_{Al} = (1.8 \pm 0.3) \times 10^{13}$ cm^{-2} s^{-1}. The AES measurements were performed at the temperature of adsorption.

Both these outcomes are possible, but dissolution seems to be preferred because thermal desorption of aluminum from a clean tungsten surface takes place only at much higher temperatures (1400–1500 K).

Coadsorption of aluminum and carbon on W(100). In this experiment, Al atoms were deposited onto a tungsten substrate covered with a layer of surface carbide WC formed upon the adsorption of 2 ML of C_{60} (which corresponds to ~20 ML of carbon). The corresponding evolution of the Auger signals from aluminum and carbon is illustrated in Fig. 2. The deposition of Al atoms at 1200 K is accompanied by an increase in the Auger signal from aluminum until the formation of surface aluminide. This process was developed in the same way as in the absence of carbon. The adsorption of aluminum was accompanied by a very small (by approximately a factor of 1.25) decrease in intensity of the Auger signal from carbon. The Auger signal of tungsten exhibited a decrease to approximately the same extent. Apparently, carbon is not displaced from the substrate surface and the decrease in its Auger signal intensity is merely due to attenuation by the layer of deposited aluminum. Indeed, the same amount of Al atoms deposited onto the surface carbide at 300 K attenuated the response signal of carbon by ~15–20%, which was close (to within the experimental error) to the effect observed at elevated temperatures.

Discussion of results. Earlier [1–7], we observed the process of substitution of adatoms of one type for another in the course of the joint adsorption of nonmetal atoms such as Si, C, S, and P on refractory metals. The competition proceeded by two possible mechanisms, whereby one adsorbate displaces another to the bulk of substrate or both adatoms are removed as a result of desorption in the form of volatile diatomic molecules. All the above atoms adsorbed on refractory metals probably acquire a negative charge, as evidenced by an increase in the electron work function of tungsten (and the other studied substrates). The competition between such atoms can be adequately described using the well-known McLean–Guttmann theory [18].

Aluminum atoms adsorbed on tungsten bear a positive charge and also enter into competition for adsorption sites, displacing carbon and being displaced by silicon. Previously [8], it was suggested that this behavior is related to the limited adsorption capacity of the substrate surface, while the charged state of adatoms plays a secondary role. In other words, the main determining factor is the entropy, rather than the energetics of interactions on the substrate surface (playing the main role in the theory [18]). Apparently, these assumptions are fully valid with respect to the Si–Al system on W(100).

The situation with coadsorption of aluminum and carbon seems to be more complicated. Carbon atoms (much more negative than silicon [19]) in the adsorbed state possess a large negative charge and are more strongly (than silicon) attracted to positively charged aluminum adatoms with the formation of a binary surface compound. This factor opposes the competition for adsorption sites and the result of the interplay of these factors is unpredictable. If the attraction predominates, both adsorbates tend to coexist on the surface forming a mixed adlayer on W(100); should the competition for the adsorption sites predominate, one adsorbate displaces another to the bulk of substrate (to the state of solid solution as on Re($10\bar{1}0$) [8]). On the surface of tungsten, which is less electronegative and has a lower work function [9, 19], the former factor seems to be more pronounced than on rhenium.

In conclusion, aluminum atoms adsorbed on tungsten enters into competition with adsorbed nonmetals (silicon) for the adsorption sites at high temperatures (1200–1400 K), whereby silicon displaces aluminum from the substrate surface. At the same time, the joint adsorption of aluminum and carbon on tungsten leads to their coexistence with the formation of a mixed binary surface compound, rather than to displacement of one adsorbate by another.

Acknowledgments. This study was performed within the framework of the program "Surface Atomic Structures" (project no. 4G157) supported by the Ministry of Science and Technology of the Russian Federation.

REFERENCES

1. V. N. Ageev, E. Yu. Afanas'eva, N. R. Gall, *et al.*, Pis'ma Zh. Tekh. Fiz. **12**, 565 (1986) [Sov. Tech. Phys. Lett. **12**, 231 (1986)].
2. N. R. Gall, E. V. Rutkov, A. Ya. Tontegode, and M. M. Usufov, Phys. Low-Dimens. Semicond. Struct. **9**, 79 (1994).
3. N. R. Gall, E. V. Rut'kov, and A. Ya. Tontegode, Pis'ma Zh. Tekh. Fiz. **26** (12), 31 (2000) [Tech. Phys. Lett. **26**, 510 (2000)].

4. N. R. Gall, E. V. Rutkov, and A. Ya. Tontegode, Thin Solid Films **226**, 229 (1995).
5. N. R. Gall, E. V. Rut'kov, A. Ya. Tontegode, and M. M. Usufov, Fiz. Tverd. Tela (St. Petersburg) **38**, 2541 (1996) [Phys. Solid State **38**, 1394 (1996)].
6. N. R. Gall, E. V. Rut'kov, A. Ya. Tontegode, and M. M. Usufov, Pis'ma Zh. Tekh. Fiz. **20** (18), 65 (1994) [Tech. Phys. Lett. **20**, 752 (1994)].
7. N. R. Gall, E. V. Rut'kov, and A. Ya. Tontegode, Pis'ma Zh. Tekh. Fiz. **15**, 52 (1989) [Sov. Tech. Phys. Lett. **15**, 269 (1989)].
8. N. R. Gall, E. V. Rut'kov, and A. Ya. Tontegode, Pis'ma Zh. Tekh. Fiz. **29** (2), 55 (2003) [Tech. Phys. Lett. **29**, 66 (2003)].
9. V. S. Fomenko, *Emission Properties of Materials: A Handbook* (Naukova Dumka, Kiev, 1981) [in Russian].
10. V. G. Samsonov and I. M. Vinitskiĭ, *Refractory Compounds: A Handbook* (Metallurgiya, Moscow, 1976), pp. 232–240 [in Russian].
11. G. K. Boreskov, *Heterogeneous Analysis* (Nauka, Moscow, 1988) [in Russian].
12. N. R. Gall, S. N. Mikhailov, E. V. Rut'kov, and A. Ya. Tontegode, Surf. Sci. **191**, 185 (1987).
13. N. R. Gall, E. V. Rut'kov, and A. Ya. Tontegode, Zh. Tekh. Fiz. **60** (4), 125 (1990) [Sov. Phys. Tech. Phys. **35**, 475 (1990)].
14. N. R. Gall, E. V. Rut'kov, and A. Ya. Tontegode, Fiz. Tverd. Tela (St. Petersburg) **44**, 179 (2002) [Phys. Solid State **44**, 1394 (2002)].
15. M. Parschan and K. Cristmann, Surf. Sci. **347**, 63 (1996).
16. N. R. Gall, E. V. Rut'kov, and A. Ya. Tontegode, Izv. Ross. Akad. Nauk, Ser. Fiz. **62**, 1980 (1998).
17. N. D. Potekhina, N. R. Gall, E. V. Rut'kov, and A. Ya. Tontegode, Fiz. Tverd. Tela (St. Petersburg) **45**, 742 (2003) [Phys. Solid State **45**, 782 (2003)].
18. M. Guttmann and D. McLean, in *Interfacial Segregation*, Ed. by W. C. Johnson and J. M. Blakely (American Society for Metals, Metal Park, 1979), pp. 261–347.
19. H. B. Gray, *Electrons and Chemical Bonding* (Benjamin, New York, 1964).

Translated by P. Pozdeev

Technical Physics Letters, Vol. 30, No. 10, 2004, pp. 836–838. Translated from Pis'ma v Zhurnal Tekhnicheskoĭ Fiziki, Vol. 30, No. 19, 2004, pp. 80–86.

SIMS Profiling of GaAs/δ-AlAs/GaAs/… Heterostructures Using Polyatomic Ionized Oxygen Clusters

B. Ya. Ber*, A. P. Kovarsky, D. Yu. Kazantsev, Yu. V. Trushin, E. E. Zhurkin, A. A. Schmidt, and S. F. Belykh

Ioffe Physicotechnical Institute, Russian Academy of Sciences, St. Petersburg, 194021 Russia
St. Petersburg State Technical University, St. Petersburg, 195251 Russia
Department of Chemistry, University of Antwerp (UIA), B-2610 Antwerp (Wilrijk), Belgium
** e-mail: boris.ber@mail.ioffe.ru*

Received April 20, 2004

Abstract—We have studied the possibility of using polyatomic ions as the primary projectile particles for the depth profiling of solid heterostructures by means of secondary ion mass spectrometry (SIMS) in combination with ion etching. Bombardment of a target by ionized oxygen clusters of the O_n^+ ($n = 3, 4$) type allows the specific impact energy per primary atom to be reduced, which significantly improves the depth resolution. It is shown that a beam of primary O_n^+ ($n = 3, 4$) clusters with the specific impact energy as low as 1 keV per oxygen atom can be obtained using a standard ion source with a magnetic mass separator. High-resolution depth profiles of a test heterostructure of the GaAs/δ-AlAs/GaAs/… type were obtained using a magnetic sector mass spectrometer and a primary beam of O_3^+ ions with a specific energy of 1 keV per oxygen atom. The experimental data are compared with the results of computer simulation of the ion sputtering process performed using the DITRIRS code. © *2004 MAIK "Nauka/Interperiodica".*

Secondary ion mass spectrometry (SIMS) has proved to be one of the most powerful surface analytical techniques. An important advantage of SIMS is the combination of a low impurity detection limit (10^{14} cm^{-3}) with a high surface sensitivity, which is related to a very small probed depth (on the order of 2 atomic monolayers). For this reason, SIMS in combination with layer-by-layer ion etching (called dynamic SIMS depth profiling) has become the main method used for the investigation of impurity distribution in depth of various solid structures [1, 2]. A serious physical limitation of this method is related to the radiation damage introduced into the near-surface region of a target by particles of the primary ion beam. Fast atomic particles with a typical kinetic impact energy on the order of 3–10 keV produce, besides sputtering of the target surface and emission of the secondary ions, a significant ion-beam-induced mixing. This is manifested by the smearing of sharp changes in atomic concentrations existing in the initial structure.

The degree of the ion beam mixing can be reduced by increasing the mass of the primary beam particles, by optimizing the beam incidence angle, and, most effectively, by decreasing the impact energy down to 0.2–1.0 keV. Unfortunately, a decrease in the primary ion beam energy below 7–10 keV in magnetic sector SIMS instruments leads to a drastic decrease in the ion beam current and impairs the conditions of focusing. Moreover, the analyzed target in such systems is one of the elements of the secondary ion beam optics and is kept at a high potential (on the order of 4.5 kV). It is this optics that provides for a high mass resolution in combination with a high efficiency of collection of secondary ions. However, in the case when the primary and secondary ion charges are of the same sign, a high target potential leads to repulsion of the primary ions from the target, thus changing the impact energy and the angle of incidence. For these reasons, the possibility of reducing the impact energy is restricted to a level of about 3 keV.

In this study, we have tried an alternative approach providing for a significant decrease in the effective kinetic impact energy. This approach consists in replacing the traditional primary molecular oxygen ions O_2^+ by the polyatomic O_n^+ clusters of higher masses [3]. Impinging on a target, such a cluster (accelerated to the same primary energy on the order of 10 keV corresponding to a total impact energy of about 5.5 keV) exhibits dissociation into monoatomic components sharing kinetic energy. Each component atom, possessing a much lower kinetic energy (1 keV and below), initiates an atomic mixing cascade of a significantly smaller size with the resulting ion sputtering and secondary ion emission. It is important to note that this approach provides for the necessary conditions of

1063-7850/04/3010-0836$26.00 © 2004 MAIK "Nauka/Interperiodica"

focusing of the primary ions and optimizes their angle of incidence onto the target in a system with the standard ion optics intended for the formation of medium-energy charged particle beams.

A model target used in this study was prepared by means of molecular beam epitaxy (MBE). The target comprised an epitaxial layer of GaAs periodically delta-doped with AlAs marker monolayers. According to the transmission electron microscopy data, the distance between δ-AlAs layers, as well as the depth of the uppermost layer, were 32 nm. The dynamic depth profiling of this structure was performed using a magnetic sector SIMS system of a Cameca IMS4f microprobe equipped with the standard source of O_n^+ ions (duoplasmatron) and a magnetic mass separator of the primary ion beam. The mass separator was used for extracting oxygen clusters of required composition from the duoplasmatron. The target (sample) potential was +4.5 kV. The calculated optimum angles of incidence of the primary oxygen clusters (measured from the normal to the sample surface) were within 35°–40°. The current of the primary O_n^+ ions extracted from the duoplasmatron at a given accelerating voltage was optimized by controlling the oxygen pressure in the ion source, the magnetic field compressing the oxygen plasma, the plasma discharge current, and the mutual arrangement of an intermediate electrode and anode.

By controlling the duoplasmatron, the magnetic separator, and the primary ion beam optics in this way, it was possible to obtain the beams of ionized oxygen clusters O_n^+ with n = 1, 2, 3, and 4. At an accelerating voltage of 12.5 keV, the currents of O_1^+, O_2^+, O_3^+, and O_4^+ ion beams were 500, 3000, 70, and 20 nA, respectively, while the currents of greater clusters did not exceed 1 pA. The primary beam was focused into a spot with a diameter of 20 μm and scanned over a 250 × 250-μm area on the target surface. In this regime, the beam current for O_3^+ and O_4^+ ions was 5–7 and 2–3 nA, respectively. The depth profiles were obtained for the positive secondary ions $^{16}O^+$ and $^{27}Al^+$ emitted from the central region of the crater bottom with a diameter of 60 μm. The mass resolution was $M/\Delta M$ = 300. The depth resolution was characterized by the length of the decay region corresponding to the thickness of a sputtered layer in which the intensity of $^{27}Al^+$ secondary ions in the profile of the δ-AlAs marker layer decreases e times.

In the first series of experiments, the GaAs/δ-AlAs/GaAs/…GaAs(001) target was bombarded by O_3^+ oxygen clusters at various accelerating voltages. The results of SIMS profiling in this regime are presented in Figs. 1 and 2 and in the table. The minimum specific impact energy of 1 keV per oxygen atom achieved at an accelerating voltage of 7.5 kV provided for the best depth resolution corresponding to a decay length of 1.8 nm at a quite satisfactory etching rate of 4 nm/min.

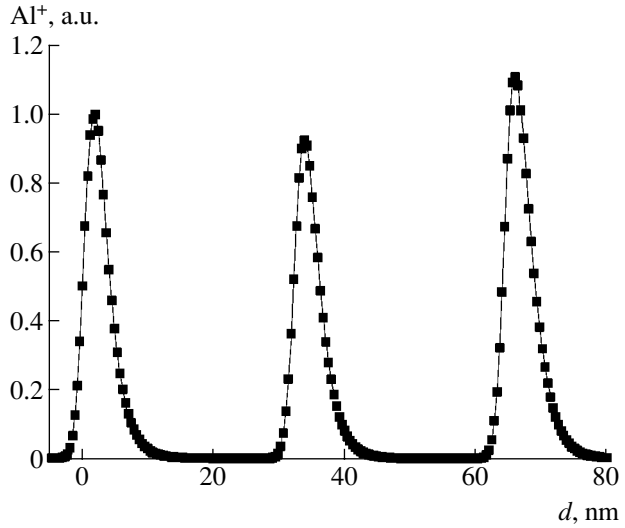

Fig. 1. SIMS profile of a model GaAs/δ-AlAs/GaAs/… GaAs(001) structure bombarded with O_3^+ primary ions at a specific impact energy of 1 keV per oxygen atom (d is the distance measured relative to the first buried δ-AlAs layer).

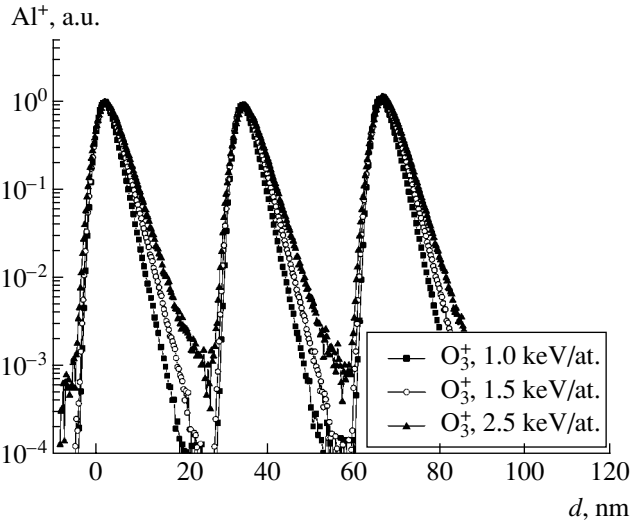

Fig. 2. SIMS profiles of a model GaAs/δ-AlAs/GaAs/… GaAs(001) structure measured with O_3^+ primary ions at various specific impact energies (logarithmic intensity scale).

In the second series of experiments, the target was bombarded by O_n^+ charged oxygen clusters with n = 1, 2, 3, and 4 at a fixed accelerating voltage of 12.5 keV (and, hence, at a fixed cluster impact energy of 8 keV). The results of SIMS profiling in this case are presented in the table. Despite a decrease in the primary ion beam current with increasing mass of the oxygen cluster, the

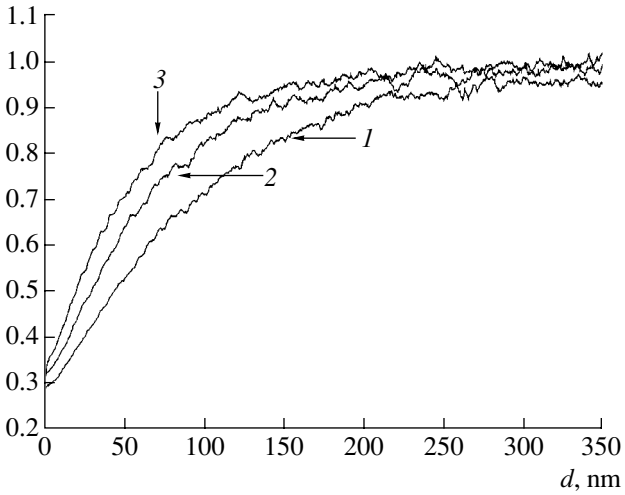

Fig. 3. Plots of the partial yield of secondary oxygen ions in the course of ion etching of a GaAs target with oxygen ions at various specific impact energies (keV per oxygen atom): (*1*) 2.5; (*2*) 1.5; (*3*) 1.0.

rate of target etching with O_4^+ clusters was 0.7 nm/min, which is sufficient for the profiling of shallow *p*–*n* junctions and quantum-sized structures.

An important characteristic of the SIMS profiling process is the depth of ion etching at which the regime of sputtering of a homogeneous target becomes stationary. For studying shallow buried structures, this depth should be minimal because the methods of quantitative SIMS analysis have been developed only for the stationary sputtering regime. In order to determine the effect of the primary particle energy on the depth of stationary sputtering, we have performed computer simulation of the ion etching of GaAs by oxygen ions under the conditions of various impact energies. The results of simulation of the ion etching process using the DITRIRS program package [4, 5] are presented in Fig. 3. Attaining the stage of stationary etching implies, in particular, that the partial yield of primary particles is unity. As can be seen from Fig. 3, a decrease in the specific impact energy significantly decreases the depth of attaining the stationary sputtering regime.

Characteristics of the dynamic SIMS profiling using polyatomic ionized oxygen clusters

Primary particles	Accelerating voltage, kV	Specific impact energy per oxygen atom, keV	Profile decay length, nm
O_3^+	12.0	2.5	2.8
O_3^+	9.0	1.5	2.3
O_3^+	7.5	1.0	1.8
O_1^+	12.5	8.0	3.8
O_2^+	12.5	4.0	3.0
O_3^+	12.5	2.7	2.7
O_4^+	12.5	2.0	2.6

Thus, we have demonstrated that using polyatomic oxygen ions O_n^+ (n = 3, 4) for SIMS profiling provides for a several-fold decrease in the specific impact energy, while retaining the angle of incidence and the conditions of focusing of the primary ion beam. The results of profiling of a model GaAs/δ-AlAs/GaAs/…GaAs(001) structure by SIMS using O_3^+ primary ions at a specific impact energy of 1 keV per oxygen atom showed that an analysis in this regime provides for a high depth resolution characterized by a decay length of 1.8 nm on the trailing edge of the marker δ-AlAs layer at an ion etching rate of 4 nm/min. This confirms the possibility of quantitative SIMS analysis of shallow buried structures using magnetic sector SIMS instruments with the standard primary ion beam optics.

Acknowledgments. This study was supported in part by the Russian Foundation for Basic Research (project no. 02-02-17605), the Ministry of Industry, Science, and Technology of the Russian Federation (within the framework of the "Physics of Solid-State Nanostructures" program), the Department of Physical Sciences of the Russian Academy of Sciences (within the framework of the "New Materials and Structures" Basic Research Program), and the International Scientific-Technological Center (grant no. 2630).

REFERENCES

1. P. C. Zalm, Rep. Prog. Phys. **58**, 1321 (1995).
2. P. C. Zalm, in *Proceedings of the 6th Workshop of the European Microbeam Analysis Society (EMAS-99) on Modern Developments and Applications in Microbeam Analysis, Konzilgebäude, 1999*, Ed. by C. T. Walker, P. Karduck, and A. Armigliato; Microchimica Acta **132**, 243 (2000).
3. H. Yamazaki and Y. Mitani, Nucl. Instrum. Methods Phys. Res. B **124**, 91 (1997).
4. B. J. Ber, V. S. Kharlamov, Yu. A. Kudrjavtsev, *et al.*, Nucl. Instrum. Methods Phys. Res. B **127**–**128**, 286 (1997).
5. Yu. V. Trushin, B. J. Ber, V. S. Kharlamov, *et al.*, J. Nucl. Mater. **237**, Part 2, 991 (1996).

Translated by P. Pozdeev

Technical Physics Letters, Vol. 30, No. 10, 2004, pp. 839–842. Translated from Pis'ma v Zhurnal Tekhnicheskoĭ Fiziki, Vol. 30, No. 19, 2004, pp. 87–94.

Fullerene C_{60} Diffusion in Thin Layers of Amorphous Polymers: Polystyrene and Poly(α-methylstyrene)

A. O. Pozdnyakov*, B. L. Baskin, and O. F. Pozdnyakov

Ioffe Physicotechnical Institute, Russian Academy of Sciences, St. Petersburg, 194021 Russia

** e-mail: ao.pozd@mail.ioffe.ru*

Received April 14, 2004

Abstract—The outdiffusion of fullerene C_{60} from submicron films of polymer–fullerene blends has been studied by thermodesorption mass spectrometry (TDMS). The energy parameters of C_{60} diffusion in polystyrene and poly(α-methylstyrene) were determined and compared to the parameters of desorption of C_{60} molecules from a multilayer film of pure fullerene deposited onto a substrate from toluene solution. © *2004 MAIK "Nauka/Interperiodica".*

Diffusion is among the key factors controlling the structural stability and physical properties of nanostructural materials [1, 2]. Allowance for the diffusion of components is especially important in nanometer-scale heterostructures, since the diffusion smearing of heteroboundaries even within several angströms may significantly modify the properties of such systems. For example, introduction of C_{60} molecules into a commercial photoresist, for example, poly(methyl methacrylate) (PMMA) based ZEP520 or SAL601, significantly improves the contrast of nanometer-scale patterns [3]. The thermal stability of thin films of amorphous polymers doped with C_{60} molecules frequently determines the possibility of using such materials in microelectronics. In condensed media, the diffusion process may limit both the kinetics of chemical reactions between macromolecules responsible for the thermal stability of the polymeric matrix and the kinetics of various photoinduced processes [5], thus determining the working life of various device structures.

We have used thermodesorption mass spectrometry (TDMS) for studying the state of fullerene C_{60} molecules in submicron layers of (chemically unbound) polymer–fullerene blends with a broad range of fullerene concentrations. The kinetics of C_{60} evolution from chemically bound C_{60}–polystyrene compositions were studied previously [6].

The composition of desorbed products and the kinetics of desorption were studied using an MX-1320 mass spectrometer [6]. The experiments were performed with polystyrene (PS) and poly(α-methylstyrene) (P-α-MS) synthesized by anionic polymerization with molecular masses 90000 and 43000, respectively. The sample films were obtained on a tantalum ribbon substrate by casting a solution of polymer and fullerene in toluene, dosed with the aid of a microsyringe. The rate of sample heating during TDMS measurements was 17 K/s. The concentration of C_{60} in the samples is conveniently characterized by the ratio of the number of monomer units (N_{mono}) to the number of C_{60} molecules ($N_{C_{60}}$) in the blend: $\varphi = N_{\text{mono}}/N_{C_{60}}$.

The results of our measurements showed that the outdiffusion of C_{60} molecules from a PS layer takes place in the temperature interval 200–400°C, which is higher than the glass transition temperature of PS (~100°C) but significantly lower than the temperature of thermal degradation of this polymer (~500°C) with the formation of monomers. Figure 1 shows the typical thermograms of fullerene desorption from PS films with thicknesses of δ = 45, 90, and 270 nm and the same initial concentration of C_{60} corresponding to

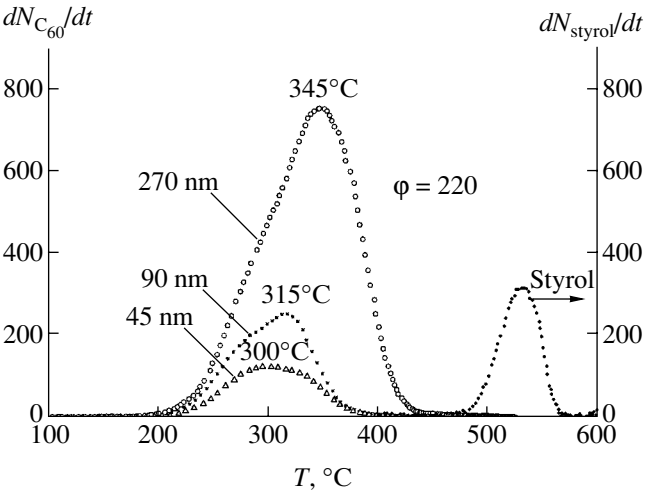

Fig. 1. Temperature dependence of the rate of C_{60} desorption from PS films of various thicknesses with the same initial content of fullerene (φ = 220) and the rate of styrene monomer formation in the course of thermal decomposition of the PS matrix.

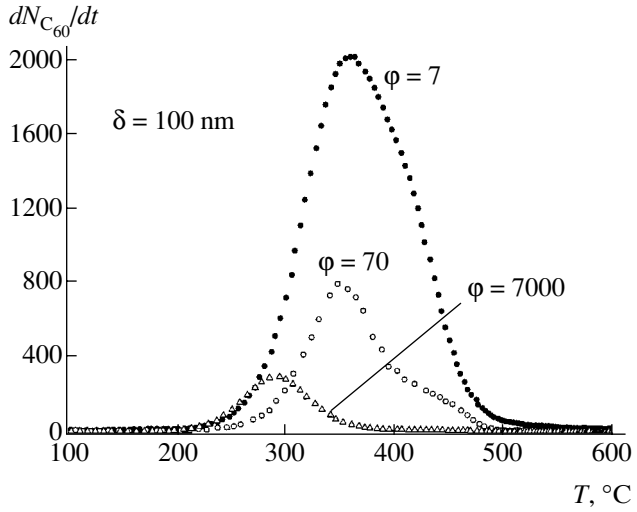

Fig. 2. Temperature dependence of the rate of C_{60} desorption from 100-nm-thick PS films with the various initial fullerene concentrations.

φ = 220. The thermogram also shows the kinetics of formation of the PS monomer (styrene). The positions of peaks of the fullerene desorption rate for the films studied were T^*_{max} = 300, 315, and 345°C. As can be seen from Fig. 1, the desorption curve for the PS layer with δ ≤ 45 nm is virtually monomodal (monochronous kinetics), while the peaks of fullerene desorption from thicker layers are nonmonochronous. It was found that the shape of the kinetic curve depends on the sample preparation, in particular, on the regime of layer drying. However, the layers of minimum thickness (with δ not exceeding ~40 nm) exhibit no such dependence. Since the polymer casting solution is a system comprising three weakly bound components (polymer, solvent, and fullerene), the behavior of this system may in fact be sensitive to various external factors. For example, evaporation of the solvent (in air at room temperature) may be accompanied by the segregation of C_{60} molecules at the solvent–substrate interface [7] resulting in a nonuniform initial distribution of C_{60} in depth of the polymer layer. According to [8], an increase in the depth of a thin implanted layer of a gas-diffusant leads to a shift of the desorption peak toward higher temperatures. In our experiments, the depth of fullerene in a polymer film is determined by the thickness of dry polymer layer.

Figure 2 shows the characteristic temperature dependences of the rate of fullerene desorption $dN_{C_{60}}/dt$ from PS films of the same thickness with various initial content of C_{60}. As the fullerene concentration increases, the curve shape significantly changes: the temperature interval ΔT of fullerene evolution expands, while the temperature of the desorption onset ($T_0 \cong 200$°C) remains unchanged. Indeed, $\Delta T \cong 150$°C for φ = 7000, and $\Delta T \cong 300$°C for φ = 7. As φ increases, the peak of the curve (T^*_{max}) shifts toward higher temperatures and an additional shoulder appears on the high-temperature branch. The diffusion activation energy (E_{diff}) was determined using the Arrhenius relation for the initial stage of desorption (i.e., for T = 200–300°C). It was found that $E_{diff} \approx 96 \pm 4$ kJ/mol irrespective of the fullerene concentration. The fact that E_{diff} is independent of φ implies that about 3 mass % of C_{60} molecules in the samples occur in the state of molecular dispersion. Determining E_{diff} for the other possible states is hindered by the presence of the low-temperature stage. For this reason, the process of fullerene outdiffusion was characterized by the value of T_{max}. As demonstrated in [9], this value is proportional to the activation energy, provided that the experimental conditions (e.g., the sample heating rate) remain unchanged.

The results of TDMS measurements of the kinetics of C_{60} desorption from a pure fullerene film (also deposited from solution) with a thickness corresponding to several monolayers (ML) of C_{60} molecules showed that the position of maximum T_{max} of the thermodesorption curve depends on the calculated layer thickness. For such multilayer C_{60} films with thicknesses corresponding to ~3, 50, and 100 ML, the peak temperatures were ~380, 440, and 470°C, respectively. As the layer thickness increases further, the value of T_{max} remains virtually unchanged. The activation energy E_d determined for the initial part of the curve of C_{60} desorption from multilayer C_{60} films was ~115 kJ/mol. This value is somewhat lower than the activation energies reported for the fullerene films obtained by thermal deposition. For example, the activation energy for C_{60} desorption from a multilayer film on Al_2O_3(0001) was E_d = 136 kJ/mol [10], while an analogous value for a monolayer of C_{60} on pyrographite was 163 kJ/mol [11]. The difference of our E_d value from published data is probably related to some features in the microstructure of layers deposited from solution, in particular, with the presence of islands and their size distribution and/or with the residual solvent strongly retained in C_{60} layers on the metal surface (for example, it was demonstrated [12] that residual solvent is removed from the C_{60}–toluene system only during C_{60} sublimation).

As can be seen from Figs. 1 and 2, the values of T^*_{max} (~300°C) for the kinetics of C_{60} desorption from PS are significantly lower than T_{max} for the fullerene desorption from a pure C_{60} multilayer film. This fact indicates that the energy of intermolecular interaction between C_{60} and PS macromolecules is smaller than the energy of C_{60}–C_{60} bonds. This provides conditions for the formation of C_{60} clusters in a polymer matrix and the nucleation of a new phase at a certain concentration of C_{60}. Earlier, we demonstrated this possibility by

TDMS and X-ray diffraction analysis of C_{60} mixtures with a trifluorochloroethylene–vinylidene fluoride copolymer [13] and PMMA [14]. The possibility of nucleation of foreign molecules in a polymer matrix was also demonstrated long ago [15–18]. It is believed that the formation of molecular aggregates, clusters, and dissolved compounds in a polymer matrix is possible, provided that the intermolecular interaction between molecules dissolved in the polymer is stronger than the interaction between these molecules and polymer macromolecules.

In the context of considering the structure of PS–fullerene blends, it was also of interest to compare this system with the P-α-MS–fullerene blends. The results of TDMS measurements showed that C_{60} desorption from P-α-MS (in contrast to that from PS) takes place both before and in the course of the thermal degradation (depolymerization with liberation of α-methylstyrene monomers) of P-α-MS macromolecules (Fig. 3). This is related to the fact that the thermal stability of P-α-MS is lower than that of PS. Indeed, the temperature interval of the thermal degradation of PS extends from 470 to 570°C (with T^*_{max} = 530°C, Fig. 1), while P-α-MS exhibits degradation in the range 300–420°C (T^*_{max} = 365°C, Fig. 3). For neat P-α-MS, this temperature is always about 10°C lower (~355°C) than for the P-α-MS–fullerene blends. This fact is indicative of a certain inhibiting action of C_{60} on the thermal degradation of P-α-MS.

Nevertheless, there are common features in the behavior of two polymer blends with fullerene C_{60}. A certain fraction of C_{60} molecules in the P-α-MS matrix also occurs in the state of molecular dispersion. This is evidenced by a shift of the peaks T_{max} of fullerene desorption kinetics toward lower values with fullerene content in the blend decreasing to φ = 30 (Fig. 3). For φ = 2.5, the thermogram (measured under otherwise equal conditions) shows the presence of C_{60} molecules in two different states manifested by two desorption peaks. The second peak is naturally attributed to C_{60} clusters. In the P-α-MS matrix, fullerene clusters do not pass to the state of molecular dispersion by the moment of the onset of macrochain degradation and, hence, sublime either in the course of depolymerization or upon complete degradation of P-α-MS macromolecules and their elimination from the system. The presence of C_{60} clusters in P-α-MS–fullerene blends with φ = 2.5 was also indicated by the aforementioned evolution of residual toluene traces simultaneously with the sublimation of C_{60} (Fig. 3). The temperature of the second peaks in the kinetics of C_{60} desorption from P-α-MS is 420°C, which corresponds to T_{max} for the sublimation of fullerene from a multilayer C_{60} film. Evaluation of the activation energy for C_{60} desorption from P-α-MS–fullerene blends gave $E_{diff} \cong 92$ kJ/mol, which agrees well (to within experimental error) with the value for the PS–fullerene system.

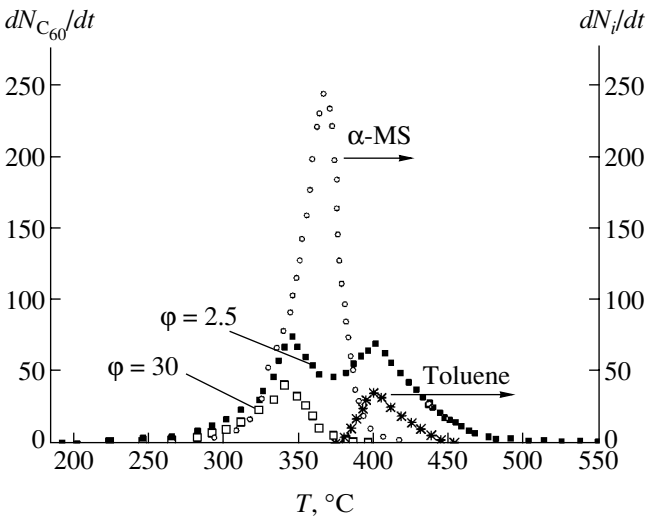

Fig. 3. Temperature dependence of the rate of C_{60} desorption from P-α-MS films with φ = 2.5 and 30 (left ordinate axis) and the rates of α-methylstyrene and residual toluene evolution (right ordinate axis). The intensities of desorption peaks are not normalized.

In conclusion, the results of our TDMS measurements showed that fullerene C_{60} in submicron adsorbed films of blends with PS and P-α-MS occurs both in the state of molecular dispersion and in the form of clusters. These results will be taken into account in the course of more detailed investigations of the mechanism of formation of fullerene states in polymer matrices aimed at the development of methods for the modification of physical properties of fullerene-containing polymers.

Acknowledgments. This study was supported by the programs "New Materials and Structures" and "Low-Dimensional Quantum Structures" of the Russian Academy of Sciences.

REFERENCES

1. *Handbook of Nanoscience, Engineering, and Technology*, Ed. by W. A. Goddard, D. W. Brenner, S. E. Lyshevski, and G. J. Iafrate (CRC Press, London, 2003), pp. 17–13.
2. *Thin Films: Interdiffusion and Reactions*, Ed. by J. M. Poate, K. Tu, and J. Meier (Wiley, New York, 1978).
3. T. Ishii, H. Nozawa, and T. Tamamura, Microelectron. Eng. **35**, 113 (1997).
4. N. M. Emanuel' and A. L. Buchachenko, *Chemical Physics of Molecular Decomposition and Stabilization of Polymers* (Nauka, Moscow, 1988) [in Russian].
5. J. Guillet, *Polymer Photophysics and Photochemistry: An Introduction to the Study of Photoprocesses in Macromolecules* (Cambridge Univ. Press, Cambridge, 1985; Mir, Moscow, 1988).

6. O. F. Pozdnyakov, B. P. Redkov, and A. O. Pozdnyakov, Pis'ma Zh. Tekh. Fiz. **28** (24), 53 (2002) [Tech. Phys. Lett. **28**, 1046 (2002)].
7. G. D. Parfitt and C. H. Rochester, *Adsorption from Solution at the Solid/Liquid Interface* (Academic, London, 1983).
8. A. G. Zholnin and A. G. Zaluzhnyĭ, Poverkhnost, No. 10, 33 (1986).
9. *Handbook of Thin-Film Technology*, Ed. by L. I. Maissel and R. Glang (McGraw-Hill, New York, 1970).
10. A. Tokmakoff, D. R. Haynes, and S. M. George, Chem. Phys. Lett. **186**, 450 (1991).
11. H. Ulbricht, G. Moss, and T. Hertel, Phys. Rev. Lett. **90**, 095501 (2003).
12. O. F. Pozdnyakov, B. P. Redkov, B. M. Ginzburg, *et al.*, Pis'ma Zh. Tekh. Fiz. **24** (23), 23 (1998) [Tech. Phys. Lett. **24**, 916 (1998)].
13. A. O. Pozdnyakov, B. M. Ginzburg, O. F. Pozdnyakov, *et al.*, Zh. Prikl. Khim. (S.-Peterburg) **73**, 134 (2000).
14. B. M. Ginzburg, E. Yu. Melenevskaya, A. V. Novoselova, *et al.*, Vysokomol. Soedin., Ser. A **46**, 1 (2004).
15. C. E. Rogers, V. Stannett, and M. Szwarz, J. Phys. Chem. **63**, 1406 (1959).
16. P. E. Rouse, J. Am. Chem. Soc. **69**, 1068 (1947).
17. H. Yasuda and V. Stannett, J. Pol. Sci. **57**, 907 (1962).
18. E. B. Trostyanskaya, A. R. Bel'nik, A. M. Poĭmanov, *et al.*, Vysokomol. Soedin., Ser. A **12**, 1778 (1970).

Translated by P. Pozdeev

Technical Physics Letters, Vol. 30, No. 10, 2004, pp. 843–845. Translated from Pis'ma v Zhurnal Tekhnicheskoĭ Fiziki, Vol. 30, No. 20, 2004, pp. 1–7.

Information Encoding by Stabilized Cycles of Dynamical Systems

A. Yu. Loskutov*, S. D. Rybalko, and A. A. Churaev

Moscow State University, Moscow, 119899 Russia

Bauman State Technical University, Moscow, 107005 Russia

** e-mail: Loskutov@moldyn.phys.msu.ru*

Received April 1, 2004

Abstract—A new method is proposed for masking transferred data with the aid of chaotic maps. The cryptographic stability is analyzed by the method of total probing. A correlation analysis of the obtained codes is performed and predictability of the code sequence is evaluated. A network application is developed, which allows legal users to exchange messages protected by the proposed method. © *2004 MAIK "Nauka/Interperiodica".*

In the present-day stage of development of communication technologies, the problem of protecting information is among the most important. In this Letter, we propose an original method of data encoding, which makes use of the possibility of stabilizing the cycles of chaotic maps. This possibility is based on a well-known fact of the theory of dynamical systems [1–3] (see also [4, 5] and references therein): there exist periodic perturbations of chaotic dynamical systems belonging to rather general types, which lead to stabilization of the cycle with a given period. Although data encoding by means of chaotic systems is now very popular (see, e.g., [6–11] and references therein), the proposed method is advantageous in allowing a network application to be developed for exchanging messages without preliminary synchronization of the transmitter and receiver (which is usually necessary in other approaches). Moreover, programs to be developed in the nearest future will allow sound messages to be encoded as well.

In order to explain the proposed principle of data encoding, we will first describe the main theoretical result concerning the stabilization of cycles. Consider a map of some region M and $\mathbf{R}^j$ into itself:

$$T_a : \mathbf{x} \mapsto \mathbf{f}(\mathbf{x}, a), \tag{1}$$

where a is a parameter from the set of possible values $A \subset \mathbf{R}$, $\mathbf{x} = \{x_1, \ldots, x_j\}$, and $\mathbf{f} = \{f_1, \ldots, f_j\}$. Let us introduce the concept of parametric perturbation. The most natural way of doing this is to define a map with respect to parameter a, which would determine its value at each moment of time, $G : A \longrightarrow A$, $a \longrightarrow g(a)$. A perturbation will be called periodic with a period of τ, provided that the function $g(a)$ is defined only in τ points $a_1, \ldots, a_\tau$ in the following manner: $a_{i+1} = g(a_i)$, $i = 1, \ldots, \tau - 1$; and $a_1 = g(a_\tau)$. In this case, the set of perturbations with period τ can be brought into correspondence with the set $\mathbf{A} = \{\hat{a} \in \underbrace{A \otimes A \otimes \ldots \otimes A}_{\tau \text{ times}}$:

$$\hat{a} = (a_1, \ldots, a_\tau),\ a_i \neq a_j,\ 1 \leq i, j \leq \tau,\ i \neq j,\ a_1, \ldots, a_\tau \in A\},$$

$$\mathbf{A} \subset \mathbf{R}^\tau.$$

Let us introduce a subset $A_c \subset A$ corresponding to only the chaotic behavior of map (1). In some papers (see, e.g., [2, 12–12]), it was proved that, for $j = 1$ and $j = 2$, there exist perturbations $\hat{a} = (a_1, a_2, \ldots, a_\tau)$ such that, for $\hat{a} \in \mathbf{A}_c$ (or $g(a) \in A_c$), a perturbed map will be regular with a stable cycle of period $t = \tau n$. Moreover, the following exact result is valid for one-dimensional maps ($j = 1$) [5].

Let a map $T_a : x \mapsto f(x, a)$, $x \in M$, $a \in A$ obey the conditions that (i) there exists a subset $\sigma \subset M$ such that, for any $x_1, x_2 \in \sigma$, there can be found $a^* \in A$ for which $f(x_1, a^*) = x_2$ and (ii) there exists a critical point $x_c \in \sigma$ such that $\partial f(x, a)/\partial x|_{x = x_c} \equiv D_x f(x_c, a) = 0$ for any $a \in A$. Then, for any $x_2, x_3, \ldots, x_\tau \in \sigma$, there can be found x_1 and $a_1, a_2, \ldots, a_\tau$ such that the cycle $(x_1, x_2, \ldots, x_\tau)$ will be a stable cycle of perturbed map $\mathbf{T}_a$ for $\hat{a} = (a_1, \ldots, a_\tau)$.

For data encoding, it is necessary to develop a method for evaluating the permissible noise level (see [15]). This can be readily done as follows [5]. Let the perturbed map $\mathbf{T}_a$ for $\hat{a} = (a_1, a_2, \ldots, a_\tau)$ to have a stable cycle of period τ, $p = (x_1, x_2, \ldots, x_\tau)$. Then, provided that

$$|\Delta a_i| \leq \delta_a = 1/\left(\tau S_a L S_x^{\tau-1} \sum_{i=1}^{\tau} S_x^i\right),$$

Table 1. The principle of encoding symbols and letter sequences for secure data transmission

$$\left\{\begin{array}{c} Y \\ \text{Symbol} \end{array}\right\} \longrightarrow \left\{\begin{array}{c} n_1, n_2, n_3 \\ \text{ASCII codes} \end{array}\right\}$$

$$\longrightarrow \left\{\begin{array}{c} \text{Cycles of periods } n_i + 2 \\ | \qquad\qquad | \\ x_0, \ldots, x_{n_1+2}, \ldots, x_{(n_1+2)+n_2+2}, \ldots, x_{(n_1+2+n_2+2)+n_3+2} \\ \text{Manifold of dynamical variables} \end{array}\right\}$$

$$\longrightarrow \left\{\begin{array}{c} \{a_1, \ldots, a_{n_1+2}\}, \{b_1, \ldots, b_{n_2+2}\}, \{c_1, \ldots, c_{n_3+2}\} \\ \text{Manifold of parameters} \end{array}\right\} \longrightarrow \left\{\begin{array}{c} a_1, \ldots, c_{n_3+2} \\ \text{Sequence of numbers} \end{array}\right\}$$

(where $i = 1, 2, \ldots, \tau$; $S_a = \max_{x,a}|D_a f(x, a)|$; $L = \max_{x,a}|D_x^2 f(x, a)|$; and $S_x = \max_{x,a}|D_x f(x, a)|$, this map also has a stable cycle, $p' = (x_1 + \Delta x_1, x_2 + \Delta x_2, \ldots, x_\tau + \Delta x_\tau)$ of period τ for $\hat{a}' = (a_1 + \Delta a_1, a_2 + \Delta a_2, \ldots, a_\tau + \Delta a_\tau)$, where $|\Delta x_i| \le \delta_x = 1/LS_x^{\tau-1}$.

In the first step of encoding, it is necessary to obtain the ASCII codes of all symbols involved in the text to be encoded. As is known, each symbol in the ASCII system corresponds to a unique triad of integers. For example, Latin letter "a" corresponds to the ASCII code 97 with the triad $n_1 = 0$, $n_2 = 9$, $n_3 = 7$. Then, each member of a triad is interpreted as the period of a cycle inherent in a dynamical system. In order to avoid degenerate cycles (period 0) and stable cycles (period 1), we add 2 to each n_i ($i = 1, 2, 3$). Now, using the chaotic properties of an applied map (or a random number generator), we create a sequence with a length equal to the sum of all n_i (increased by two) plus one. The last element is used for beginning the count of cycle periods.

The obtained sequence of random numbers is considered as the sequence of values of the dynamical variable x. For this sequence to bear information concerning the encoded symbols, we replace a part of elements by the values of critical points x_c, that is, the points where $f'(a, x))|_{x_c} = 0$. These points are separated by $n_i + 2$ steps beginning with the first. Thus, the sequence consists of subsequences, the number of which is equal to the number of members in the sequence ($n_i + 2$), that is, to the number of symbols in the coded text multiplied by three. The periods of the cycle will be equal to $n_i + 2$.

Now let us calculate the values of the control parameter $\hat{a} = a_1, \ldots, a_n$, that is, determine the perturbation stabilizing the obtained sequence of cycles. This can be readily done by considering the inverse problem of determining the parameters from the form of the map. For particular maps, perturbations $\hat{a}$ producing stabilization of the cycle of a given period form a certain region in the parametric space. This circumstance can be used for encoding repeated symbols by means of random selection of parameters from this region.

The main steps of the data encoding protocol using the proposed method are presented in Table 1. The final sequence $a_1, \ldots, c_{n_3+2}$ (representing parameters rather than the message) is sent to a transmitter, where all operations (with certain differences related to rounding) are performed in the reverse order (the method is symmetric).

In order to justify the proposed method, it is necessary to perform a statistical correlation analysis and evaluate the cryptographic stability [16]. The statistical analysis was performed using a sequence of 9000 values of the control parameters, encoding a message consisting of 1000 Latin letter "o" symbols. The transmission of this symbol represents the most dangerous regime of operation of the proposed method, since the ASCII code of this symbol is 111 and the information about each "o" is contained in the three sequential cycles of period $n_i + 2 = 1 + 2 = 3$, whose repetition is highly undesired. Satisfactory results obtained in this particular case will provide evidence of even greater reliability of the proposed method in the case of encoding other symbols. The statistical analysis gave the following results: correlation coefficient, $r = 0.0077$; regression equation, $y = 4.9322905 + 0.00769911509x$; the average value in the set, $\bar{x} = 4.96478169$. Therefore, the proposed method of data encoding is highly reliable from the standpoint of correlation analysis and is capable of protecting data messages of considerable length.

The main qualitative measures of cryptographic stability of an encrypting system are the laboriousness and reliability of the cryptographic analysis [17, 18]. We have evaluated the cryptographic stability of the proposed data encoding protocol by the method of total probing, which consists in sequential random and

Table 2. Results of evaluation of the laboriousness of decoding

Byte/coefficient	K	$E^{\alpha,\beta}$	$t_{(E)}$
1	2^{27}	2^{26}	67 s
2	2^{51}	2^{50}	30 years
3	2^{75}	2^{74}	6×10^8 years
4	2^{99}	2^{98}	10^{16} years
5	2^{123}	2^{122}	1.5×10^{23} years

Note: The left column indicates the number of bytes intended for encoding the control parameter; the right column shows the laboriousness of decoding converted into time, assuming the computation speed is equal to that of modern supercomputers.

equiprobable trial of N keys without repeats from set K. The process of probing is terminated upon testing k keys, where $k = j$, $1 < j < N$, j being the first key number for which the decoded text is considered substantially meaningful, or $k = N$ if this event does not take place for $j \le N$. The decoded text is assessed for meaningfulness using the following hypotheses: $H(0)$ for the open text and $H(1)$ for a random text. In formulating a probabilistic model, the assessment procedure is characterized by the following errors: $\alpha = P(H(1)/H(0))$, the probability of rejecting a meaningful text, and $\beta = P(H(0)/H(1))$, the probability of taking a meaningless text as meaningful. A model for calculation of the laboriousness of the cryptographic analysis can be formulated as

$$E^{\alpha,\beta}(k) = \frac{1}{K}\sum_{k=1}^{N} k(1-\beta)^{k-1}$$

$$\times\left[\beta(N-k) + \frac{\alpha\beta}{1-\beta}(k-1) + (1-\alpha)\right] + \frac{N}{K}N\alpha(1-\beta)^{N-1}$$

$$+ \frac{K-N}{K}\left(\sum_{k=1}^{N} k(1-\beta)^{k-1}\beta + N(1-\beta)^{N}\right),$$

where $E^{\alpha,\beta}(k)$ is the mathematical expectation characterizing termination of the probing process after probing k keys and N is the number of probed keys. The results of calculations performed assuming an errorless mechanism of taking decisions ($\alpha = 0$, $\beta = 0$) are summarized in Table 2. The reliability was evaluated using the relation

$$P(N, \alpha, \beta) = [(1-\alpha)/K]\sum_{t=1}^{N}(1-\beta)^{t-1}.$$

Obviously, the reliability of the method of total probing assuming errorless mechanism of taking decisions ($\alpha = 0$, $\beta = 0$) is $P = 1$.

Thus, the main advantages of the proposed method of data encoding are as follows: (i) the protocol can be implemented using a rather wide class of maps; (ii) the transmitted signal contains only information necessary for the further data processing, rather than the informative message as such; (iii) the dynamical system, which serves as the key for decoding, possesses chaotic properties; (iv) the decoding process does not require preliminary synchronization of the transmitter and receiver; (v) the method is stable with respect to external noise; (vi) theoretically, the number of possible variants is infinite. As for practical realization, a network application has been developed, which allows legal users to exchange messages protected by the proposed method.

REFERENCES

1. V. V. Alekseev and A. Yu. Loskutov, Dokl. Akad. Nauk SSSR **293**, 1346 (1987) [Sov. Phys. Dokl. **32**, 270 (1987)].
2. A. Yu. Loskutov and A. I. Shishmarev, Usp. Mat. Nauk **48**, 169 (1993).
3. E. Ott, C. Grebogi, and J. A. Yorke, Phys. Rev. Lett. **64**, 1196 (1990).
4. S. Boccaletti, C. Grebogi, Y.-C. Lai, *et al.*, Phys. Rep. **329**, 103 (2000).
5. A. Loskutov, Comp. Math. Model. **12**, 314 (2001).
6. K. M. Cuomo and A. V. Oppenheim, Phys. Rev. Lett. **71**, 65 (1993).
7. S. Hayes, C. Grebogi, E. Ott, and A. Mark, Phys. Rev. Lett. **73**, 1781 (1994).
8. L. Kocarev and U. Parlitz, Phys. Rev. Lett. **74**, 5028 (1995).
9. T. L. Carroll and L. M. Pecora, Chaos **9**, 445 (1999).
10. M. P. Kennedy and G. Kolumbán, Signal Process. **80**, 1307 (2000).
11. B. Fraser, P. Yu, and T. Lookman, Phys. Rev. E **66**, 017202 (2002).
12. A. Loskutov and A. I. Shishmarev, Chaos **4**, 391 (1994).
13. A. N. Deryugin, A. Yu. Loskutov, and V. M. Tereshko, Teor. Mat. Fiz. **104**, 507 (1995).
14. A. N. Deryugin, A. Loskutov, and V. M. Tereshko, Chaos, Solitons and Fractals **7** (10), 1 (1996).
15. M. Dolnik and E. M. Bollt, Chaos **8**, 702 (1998).
16. *Contemporary Cryptology: The Science of Information Integrity*, Ed. by G. J. Simmons (IEEE Press, New York, 1992).
17. *Theory and Practice of Providing the Information Security*, Ed. by P. D. Zegzhda (Yakhtsmen, Moscow, 1996).
18. *Cryptography*, Ed. by V. P. Sherstyuk and E. A. Primenko (SOLON-R, Moscow, 2002).

Translated by P. Pozdeev

Technical Physics Letters, Vol. 30, No. 10, 2004, pp. 846–849. Translated from Pis'ma v Zhurnal Tekhnicheskoĭ Fiziki, Vol. 30, No. 20, 2004, pp. 8–16.

Application of Ion Implantation for Synthesis of Copper Nanoparticles in a Zinc Oxide Matrix for Obtaining New Nonlinear Optical Materials

A. L. Stepanov[a,b,*], R. I. Khaibullin[b,c], N. Can[d], R. A. Ganeev[e,f], A. I. Ryasnyansky[e,g], C. Buchal[h], and S. Uysal[d]

[a] *Institute for Experimental Physics and Erwin Schrödinger Institute for Nanoscale Research, Karl-Franzens-University Graz, A-8010 Graz, Austria*

[b] *Kazan Physicotechnical Institute, Russian Academy of Sciences, Kazan, Tatarstan, 420029 Russia*

[c] *Gebze Institute of Technology, 41400 Gebze-Kocaeli, Turkey*

[d] *Physics Department, Faculty of Arts and Sciences, Celal Bayar University, 45040 Manisa, Turkey*

[e] *NPO Akadempribor, Academy of Sciences of Uzbekistan, Tashkent, 700125 Uzbekistan*

[f] *Institute for Solid State Physics, University of Tokyo, Chiba 277-8581, Japan*

[g] *Samarkand State University, Samarkand, 703004 Uzbekistan*

[h] *Institut für Schichten & Grenzflachen, KFA GmbH, Julich Forschungszentrum, D-52425 Julich, Germany*

** e-mail: anstep@kfti.knc.ru; andrey.stepanov@uni-graz.at*

Received March 24, 2004

Abstract—We have obtained a layered composite material by implantation of single crystal zinc oxide (ZnO) substrates with 160-keV Cu^+ ions to a dose of 10^{16} or 10^{17} cm^{-2}. The composite was studied by linear optical absorption spectroscopy; the nonlinear optical characteristics were determined by means of *Z*-scanning at a laser radiation wavelength of 532 nm. The appearance of the optical plasmon resonance bands in the spectra indicated that ion implantation to the higher dose provides for the formation of copper nanoparticles in a subsurface layer of ZnO. The new nonlinear optical material comprising metal nanoparticles in a ZnO matrix exhibits the phenomenon of self-defocusing and possesses a high nonlinear absorption coefficient ($\beta = 2.07 \times 10^{-3}$ cm/W). © *2004 MAIK "Nauka/Interperiodica".*

In recent years, much effort has been devoted to the research and development of new composites based on wide-bandgap semiconductors and insulators containing metal nanoparticles, which are promising materials for optoelectronics and nonlinear optics. The phenomenon of collective excitation of conduction electrons in such nanoparticles under the action of electromagnetic (light) waves, called the surface plasmon resonance, accounts for a selective optical absorption and gives rise to nonlinear optical effects in the same spectral range [1, 2]. As is known [3], materials with a high concentration of metal nanoparticles synthesized, for example, by ion implantation, possess pronounced nonlinear optical properties. For this reason, such composites can be successfully used in integrated optoelectronic devices, for example, in waveguides with nonlinear optical switching providing for signal conversion at short (pico- or femtosecond) laser pulse durations [3].

Previously, metal nanoparticles have been successfully synthesized in the matrix of zinc oxide (ZnO)—a wide-bandgap semiconductor characterized by an optical bandgap width of 3.8 eV (corresponding to 326.3 nm). The first study in this direction [4] was devoted to the synthesis of gold nanoparticles in a ZnO matrix. Presently available data on the synthesis of metal nanoparticles in ZnO [4–12], with indication of a particle size and the methods of synthesis (including ion implantation [5, 8]) and characterization, are summarized in the table. However, the ion implantation synthesis of cobalt nanoparticles described in [5] requires additional (postimplantation) thermal treatments, which complicates the technology of such composite materials. On the other hand, copper nanoparticles had been formed directly by low-energy ion implantation [8], but the particle size was so small that a postimplantation annealing was still required to enlarge them. It should be noted that there is a large number of other publications devoted to the implantation of various metal ions into ZnO, but the ion doses were so small that even subsequent high-temperature treatments did not lead to the formation of metal nanoparticles. For this reason, papers reporting on the ion doping of ZnO are not included in the table.

1063-7850/04/3010-0846$26.00 © 2004 MAIK "Nauka/Interperiodica"

From the standpoint of effective manifestation of nonlinear optical properties, the most promising metals are those with a high density of free conduction electrons, in particular, copper [3]. This study was aimed at experimental verification of the possibility of obtaining a new nonlinear optical material directly by the synthesis of copper nanoparticles in a ZnO substrate by means of ion implantation, without any postimplantation treatments. As seen from literature indicated in the table, nonlinear optical properties of ZnO with dispersed metal nanoparticles have not been studied so far.

A composite material was obtained using single crystal ZnO substrates optically transparent in a broad spectral range (~500–1100 nm). This matrix was implanted with 160-keV Cu^+ ions at a dose of 1×10^{16} or 1×10^{17} cm^{-2} at a high ion beam current density (~20–50 $\mu A/cm^2$). The ion implantation was performed at room temperature in a vacuum of 10^{-6} Torr on an EATON 3204 implanter (Julich, Germany). The optical density spectra were measured using a Perkin-Elmer Lambda 19 spectrophotometer. The spectra of the absorption cross section were also modeled, within the framework of the classical theory of interaction between electromagnetic waves and a spherical particle (Mie's theory), using a method described elsewhere [13]. The nonlinear optical characteristics of samples were determined by the method of *Z*-scan using a setup described in [14] in which the material was probed by second-harmonic radiation of a Nd:YAG laser with a wavelength of 532 nm, a pulse duration of 55 ps, and a pulse energy of 0.2 mJ. In order to avoid thermal effects influencing the nonlinear optical characteristics, the laser pulse repetition rate was not increased above 2 Hz. The laser beam intensity was controlled within (1–5) × 10^8 W/cm^2, which excluded the optical breakdown of samples.

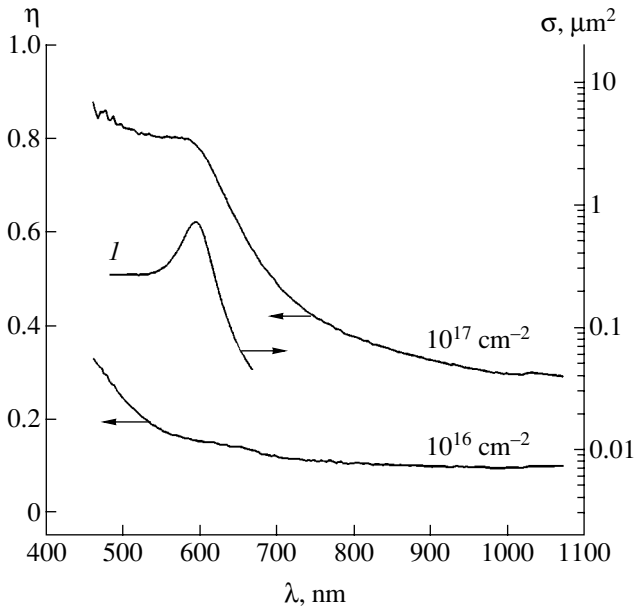

Fig. 1. Experimental spectra of the optical density η of ZnO implanted with copper to various doses, in comparison to the model spectrum of the absorption cross section σ calculated using the Mie theory (curve *1*) for a single 10-nm spherical particle in a ZnO matrix.

Figure 1 shows the experimental optical absorption spectra of the ZnO samples implanted with Cu^+ ions at different ion doses. For the sample implanted with copper to a lower dose, the spectrum is virtually identical to that of unirradiated ZnO, except for a somewhat increased absorption in a short-wavelength region

Metal nanoparticles in a ZnO matrix: types and methods of synthesis and diagnostics

Metal*	Method of synthesis	Method of diagnostics**	Particle size, nm	Authors
Co	Ion implantation and thermal annealing	XRD, SQUID	3.5	Norton *et al.*, 2003 [5]
Cu	RF sputtering and thermal annealing	OS, XRD, TEM	2–17	Varquer-Cuchillo *et al.*, 2001 [6] Pal *et al.*, 2004 [7]
Cu	Ion implantation and thermal annealing	OS	–	Kono *et al.*, 2003 [8]
Ru	Chemical deposition from solution	OS, XPS, SEM	2	Bozlee *et al.*, 2000 [9]
Pt	RF sputtering and thermal annealing	OS, XRD, TEM	1–15	Pal *et al.*, 2004 [7]
Au	Electrodeposition from solution	OS, TEM	5–50	Yoshino *et al.*, 1996 [4]
Au	Chemical deposition from solution	OS, XRD, SEM	5–40	Bozlee *et al.*, 2000 [9]
Au	Magnetron sputtering	OS, XRD, TEM	20–70	Liao *et al.*, 2003 [10]
Au	Laser ablation	OS, XRD, SEM	2–6	Tiwari *et al.*, 2003 [11]
Au	Sol-gel coating and thermal annealing	OS, XRD, SEM	50–100	Wang *et al.*, 2003 [12]
Au	RF sputtering and thermal annealing	OS, XRD, TEM	1–27	Pal *et al.*, 2004 [7]

* Metals are listed in order according to the Periodic Table; ** methods of diagnostics: OS, optical spectroscopy; XRD, X-ray diffraction; XPS, X-ray photoelectron spectroscopy; SEM, scanning electron microscopy; TEM, transmission electron microscopy; SQUID, superconducting quantum interference device magnetometry.

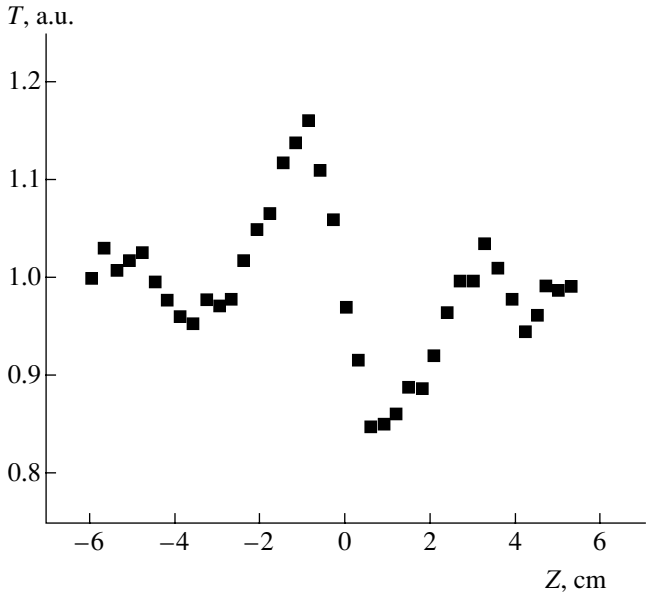

Fig. 2. Normalized transmission $T(Z)$ on the Z scale measured in the scheme with closed aperture for a ZnO matrix implanted with copper to a dose of 1×10^{17} cm^{-2}.

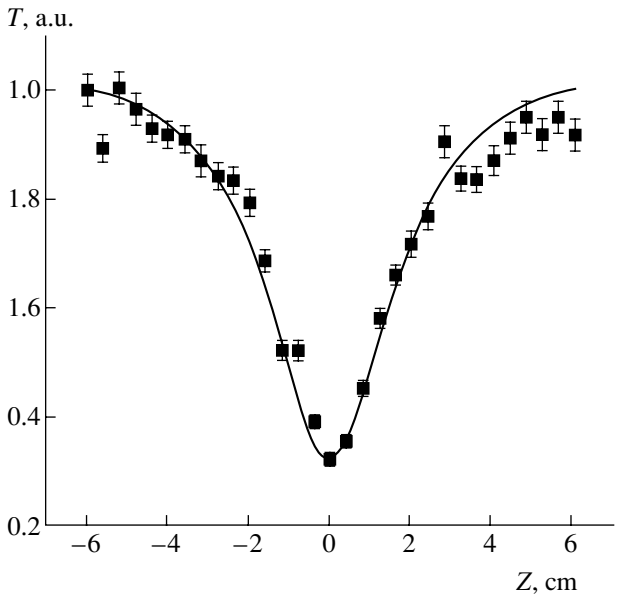

Fig. 3. Normalized transmission $T(Z)$ on the Z scale measured in the scheme with open aperture for a ZnO matrix implanted with copper to a dose of 1×10^{17} cm^{-2}. Solid curve shows the results of a model calculation.

(<450 nm), which is related to radiation-induced defects in the sample crystal. Therefore, we may conclude that this irradiation dose does not provide for the formation of sufficiently large (>2 nm) implanted copper particles capable of producing significant optical absorption due to the surface plasmon resonance. In contrast, a wide selective absorption band with a maximum at ~600 nm observed in the spectrum of the sample implanted at a higher dose is direct evidence of the formation of such copper nanoparticles exhibiting surface plasmon resonance [1]. For the comparison, Fig. 1 also shows a model spectrum of the absorption cross section calculated for a single 10-nm spherical particle in a ZnO medium, which is characterized by maximum optical absorption at the same wavelength. Thus, the calculation confirmed the possibility of formation of copper particles in a ZnO matrix. The difference between shapes of the model and experimental spectra is probably explained by the distribution of the synthesized metal nanoparticles with respect to size, which usually takes place during the ion implantation of dielectrics [2].

We believe that the main factor favoring the formation of larger nanoparticles of copper in ZnO, in the present case, in comparison to the results obtained in [8], is the higher ion beam current density used in our experiments. The surface energy density liberated in the course of stopping of the incident copper ions in our experiments was ~8 W/cm^2, which is more than 50 times the value reported in [8]. The high ion beam power ensures significant local heating in the irradiated ZnO layer, increases the diffusion mobility of implanted copper, and, hence, favors the effective nucleation and growth of metal nanoparticles.

The nonlinear optical characteristics were studied only using a ZnO sample implanted to a higher dose (1×10^{17} cm^{-2}), which was known to contain metal nanoparticles. Figures 2 and 3 show the results of measurements of the normalized transmission $T(Z)$ on the Z scale in the schemes with open and closed aperture, respectively. The shape of the $T(Z)$ curve in Fig. 2 shows that laser radiation is subject to nonlinear self-defocusing with a negative nonlinear refractive index. The complicated shape of this curve is probably determined by superposition of the effects of nonlinear refraction both from metal nanoparticles and from the ZnO matrix modified by the presence of these particles.

The character of the $T(Z)$ curve in Fig. 3 is evidence of a clear manifestation of the nonlinear optical absorption. For determining the nonlinear absorption coefficient β, we used an approach described in detail elsewhere [14]. The $T(Z)$ curve was modeled using a method proposed by Kwak *et al.* [15]. The obtained value, $\beta = 2.07 \times 10^{-3}$ cm/W, is significantly greater than that of the ZnO matrix (5×10^{-9} cm/W) for the same wavelength [16]. We believe that the high coefficient β of the composite is directly related to the presence of copper nanoparticles. It should be also noted that the value of β in our samples is two orders of magnitude higher than in a dielectric SiO_2 matrix with copper nanoparticles synthesized by ion implantation [17].

In summary, we have demonstrated the possibility of synthesizing large nanoparticles of copper in a subsurface layer of ZnO by ion implantation without subsequent thermal treatments. Using this method, we obtained a new nonlinear optical composite material,

Cu:ZnO, exhibiting self-defocusing of laser radiation and possessing a high nonlinear absorption coefficient. The latter circumstance makes the new composite a promising material for active light intensity limiters in the visible spectral range.

Acknowledgments. This study was sponsored in part by the Federal Program for Support of the Leading Scientific Schools of Russia (project no. NSh-1904.2003.2), the program "New Materials and Structures" of the Department of Physics of the Russian Academy of Sciences, the Scientific and Technical Research Council of Turkey (TÜBITAK project no. TBAG-2324-103T048), and the Science and Technology Center of Uzbekistan (grant no. 2.1.22).

A.L.S. is grateful to the Lise Meitner Programme of the Austrian Scientific Foundation (Austria) and the Alexander Humboldt Foundation (Germany) for support. R.I.K. gratefully acknowledges the NATO-TÜBITAK Advanced Fellowship Programme for support of his work at the Gebze Institute of Technology.

REFERENCES

1. U. Kreibig and M. Vollmer, *Optical Properties of Metal Clusters* (Springer-Verlag, Berlin, 1995).
2. A. L. Stepanov and D. E. Hole, in *Recent Research & Development in Applied Physics*, Ed. by A. Pandalai (Transworld Res. Network, Kuala, 2002), Vol. 5, pp. 1–26.
3. R. F. Haglund, Jr., L. Yang, R. H. Magruder III, *et al.*, Nucl. Instrum. Methods Phys. Res. B **91**, 493 (1994).
4. T. Yoshino, S. Takanezawa, T. Ohmori, and H. Masuda, Jpn. J. Appl. Phys. **35**, L1512 (1996).
5. D. P. Norton, M. E. Overberg, S. J. Pearton, *et al.*, Appl. Phys. Lett. **83**, 5488 (2003).
6. O. Vazquez-Cuchillo, A. Bautista-Hernandez, U. Pal, and L. Meza-Montes, Mod. Phys. Lett. B **15**, 625 (2001).
7. U. Pal, J. Garcia-Serrano, G. Casarrubias-Segura, *et al.*, Sol. Energy Mater. Sol. Cells **81**, 339 (2004).
8. K. Kono, S. K. Arora, and N. Kishimoto, Nucl. Instrum. Methods Phys. Res. B **206**, 291 (2003).
9. B. J. Bozlee and G. J. Exarhos, Thin Solid Films **377**–**378**, 1 (2000).
10. H. Liao, W. Wen, G. K. L. Wong, and G. Yang, Opt. Lett. **28**, 1790 (2003).
11. A. Tiwari, A. Chugh, C. Jin, and J. Narayan, J. Nanosci. Nanotechnol. **3**, 368 (2003).
12. X.-H. Wang, J. Shi, S. Dai, and Y. Yang, Thin Solid Films **429**, 102 (2003).
13. A. L. Stepanov, Zh. Tekh. Fiz. **74** (2), 1 (2004) [Tech. Phys. **49**, 143 (2004)].
14. R. A. Ganeev, A. I. Ryasnyansky, A. L. Stepanov, and T. Usmanov, Phys. Status Solidi B **241**, 935 (2004).
15. Ch. H. Kwak, Y. L. Lee, and S. G. Kim, J. Opt. Soc. Am. B **16**, 600 (1999).
16. E. W. Van Stryland, M. A. Woodal, H. Vanherzeele, and M. J. Soileau, Opt. Lett. **10**, 490 (1985).
17. R. F. Haglund, Jr., L. Yang, R. H. Magruder III, *et al.* Opt. Lett. **18**, 373 (1993).

Translated by P. Pozdeev

Technical Physics Letters, Vol. 30, No. 10, 2004, pp. 850–853. Translated from Pis'ma v Zhurnal Tekhnicheskoĭ Fiziki, Vol. 30, No. 20, 2004, pp. 17–24.

The Interaction of Cobalt with Oxidized Silicon Surface

M. V. Gomoyunova[a,*], I. I. Pronin[a], N. R. Gall[a], S. L. Molodtsov[b], and D. V. Vyalikh[a]

[a] *Ioffe Physicotechnical Institute, Russian Academy of Sciences, St. Petersburg, 194021 Russia*
[b] *Institut für Oberflächen und Mikrostrukturphysik, Technische Universität Dresden, D-01062 Dresden, Germany*
e-mail: Marina.Gomoyunova@mail.ioffe.ru

Received March 24, 2004

Abstract—The initial stages of the growth of cobalt disilicide ($CoSi_2$) on a 2×1 reconstructed Si(100) surface in the presence of oxygen have been studied for the first time by method of high-resolution photoelectron spectroscopy. The evolution of the electron structure of the sample surface was traced in the course of silicon oxidation, cobalt deposition, and subsequent thermal annealing. It is established that cobalt atoms penetrate to the oxide–silicon interface even at room temperature. This phenomenon favors the formation of an epitaxial $CoSi_2$ layer with improved morphology. © *2004 MAIK "Nauka/Interperiodica".*

Thin films of cobalt disilicide ($CoSi_2$) epitaxially grown on the surface of single crystal silicon substrates are widely used in modern solid state electronics. However, obtaining perfect $CoSi_2$ films with thicknesses in the nanometer range on Si(100)2×1 substrates used in silicon technology encounters certain difficulties. These difficulties are related to the discontinuity of the films formed in the course of solid-phase synthesis and to the formation of $CoSi_2$ grains misoriented relative to the substrate [1–3]. It was demonstrated [4–6] that the structural perfection and morphology of $CoSi_2$ films can be significantly improved by preliminary oxidation of the substrate surface. However, there was a disagreement between assumptions [4–6] concerning the mechanisms responsible for this effect.

In this context, this study was aimed at elucidating the role of oxygen in the process of silicide formation in the system studied. For this purpose, we have studied the initial stages of the growth of cobalt disilicide on the oxidized silicon surface by the method of high-resolution core level photoelectron spectroscopy using synchrotron radiation.

The experiments were performed on a Russian–German synchrotron radiation channel operating at the BESSY II storage ring. The photoelectron spectra were recorded under ultrahigh vacuum conditions at an overall energy resolution of ~130 meV. The detector collected Si 2*p* core level electrons emitted within a cone around the normal to the sample surface. The samples were prepared using single crystal silicon plates of the KEF-1 grade, with disorientation relative to the (100) crystal face not exceeding 0.1°. The plates were chemically pretreated as described by Ishizaka and Shiraki [10]. Then, the samples were annealed under ultrahigh vacuum conditions at 1200°C and slowly cooled down to room temperature. This pretreatment ensured the obtaining of 2×1 reconstructed Si(100) single crystal surface free of carbon- and oxygen-containing contaminations. The elemental composition of the sample surface was monitored by photoelectron spectroscopy.

The surface of single crystal silicon plates was oxidized at room temperature by holding in oxygen at a pressure of $\sim 10^{-7}$ Torr to a total exposure of 10^4 langmuir. Cobalt atoms were deposited onto the substrate surface at a rate of ~1 monolayer (ML) per minute ($1\ \text{ML} = 6.8 \times 10^{14}$ atoms per square centimeter, which corresponds to the surface density of silicon atoms on the Si(100) single crystal face). The measurements of the photoelectron spectra were performed at room temperature in a vacuum of 1.2×10^{-10} Torr.

Figure 1 shows the typical Si 2*p* photoelectron spectra with subtracted background obtained for a pure silicon substrate prior to oxidation, after exposure in oxygen, and after depositing various amounts of cobalt corresponding to 1.5, 4, and 8 ML. As can be seen, the interaction of oxygen with the Si(100)2×1 surface significantly modified the initial photoelectron spectrum. Changes include a decrease in the intensity of the peaks of pure silicon, disappearance of a shoulder (corresponding to the upper atoms of silicon dimers in the substrate) on the right-hand side of the $2p_{3/2}$ line [8–11], and an increase in the dip between $2p_{3/2}$ and $2p_{1/2}$ components (in the region of the mode corresponding to atoms of the second layer of the reconstructed surface). These changes are related to reconstruction of the silicon crystal surface in the course of oxidation. The oxidation process also accounts for the appearance of new

components with positive shifts in the core electron binding energy observed in a large (about 4 eV wide) interval ranging from 100.5 to 104 eV. According to the published data [12–14], these modes correspond to oxidized silicon phases with various valence states of Si atoms (from +1 to +4) and reflect the formation of an oxide layer of complex composition on the crystal surface. The phases with low valence of silicon (Si^{1+} and Si^{2+}) are in contact with a pure silicon substrate, while the phases of Si^{3+} and Si^{4+} are localized at the surface of the oxidized sample. The absence of the mode corresponding to the upper atoms of dimers (characteristic of the Si(100)2 × 1 surface) indicates that the oxide layer formed on the crystal surface is continuous (to within the sensitivity of the given probing method).

The deposition of cobalt on the oxidized silicon surface produces further modification of the photoelectron spectrum. The main changes involve the lines of pure silicon, while the oxide modes exhibit only a slight variation, most noticeably manifested by a small decrease in intensity. This indicates that cobalt atoms deposited onto the sample surface penetrate through the oxide layer rather than stay on the surface. Otherwise, a cobalt film would form on the surface and strongly attenuate the signal from oxide, which is not observed. Alternatively, a small decrease in the intensity of the oxide modes could also take place if the deposited cobalt atoms were assembled into three–dimensional islands on the surface. However, in this case, there would be no significant changes in the shape of the modes of pure silicon, which also contradicts the experiment (as was pointed out above, these modes are strongly modified). All these observations lead to the conclusion that cobalt atoms do not form a metal film on the sample surface, penetrate through the oxide layer, and accumulate at the oxide–silicon interface.

As for the lines of pure silicon, their changes upon cobalt deposition consist, first, in a significant drop in intensity of the 2*p* doublet and, second, in leveling of the peak intensities of the $2p_{3/2}$ and $2p_{1/2}$ components. The latter fact is most clearly pronounced in the Si 2*p* spectrum measured after depositing of cobalt at an amount corresponding to 8 ML. It is known that cobalt deposition onto the pure Si(100)2 × 1 reconstructed surface leads to the formation of a Co–Si solid solution layer. As the layer thickness increases, the concentration of silicon atoms at the sample surface decreases and, when the amount of deposited cobalt reaches 6–7 ML, a pure metal film forms and begins to grow. It should be also noted that the mode corresponding to the Co–Si solid solution is characterized by a negative shift of the Si 2*p* binding energy [15–18]. No such mode was observed in our experiments and, hence, no solid solution phase was formed at the oxide–silicon interface. The growing film of cobalt attenuates the signal from pure silicon, which is manifested by a decrease in intensity of the $2p_{3/2}$ and $2p_{1/2}$ lines with an increasing

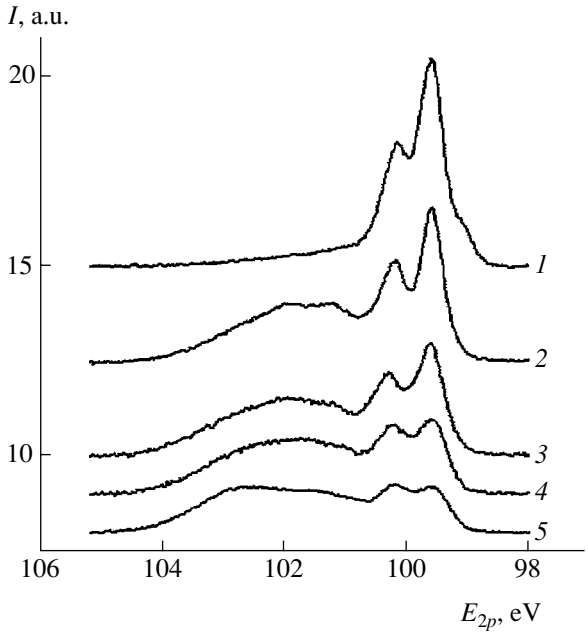

Fig. 1. Si 2*p* photoelectron spectra measured at $h\nu$ = 130 eV: (*1*) initial Si(100)2 × 1 surface; (*2*) oxidized surface; (*3–5*) oxidized surface upon cobalt deposition at an amount corresponding to 1.5, 4, and 8 ML, respectively.

amount of deposited cobalt. The leveling of intensities of these peaks can be explained by superposition of the $2p_{1/2}$ peak with the "tail" of the line of a Si^{1+} oxide phase. Indeed, estimation based on decomposition of the Si 2*p* spectrum of oxidized silicon into components [13, 14, 19] showed that the contribution of the Si^{1+} mode to the Si $2p_{1/2}$ peak intensity amounts to 15–20%. In order to ensure the leveling of $2p_{3/2}$ and $2p_{1/2}$ components, the signal from pure silicon has to be attenuated only by a factor of four or five. The amount of deposited cobalt is quite sufficient to provide for this decrease.

Now let us turn to the last stage of our experiment, whereby the samples after oxidation and cobalt deposition were annealed in vacuum. As can be seen from the data presented in Fig. 2, changes in the Si 2*p* photoelectron spectra measured in the course of annealing are revealed upon reaching a temperature of about 250°C. These changes are manifested by variation of the ratio of intensities of the peaks at ~99.5 and ~100 eV. The intensity of the $2p_{3/2}$ component begins to exceed again that of the $2p_{1/2}$ component, and this difference increases with the temperature of annealing. In addition, there is a certain decrease in spacing between the two peaks. The observed changes are explained by a decrease in the degree of attenuation of the signal from pure silicon by the cobalt film, which is related to the gradual decomposition of this film as a result of the solid-phase reaction between cobalt and silicon with the formation of cobalt disilicide at the interface. The mode of silicon entering into cobalt disilicide is charac-

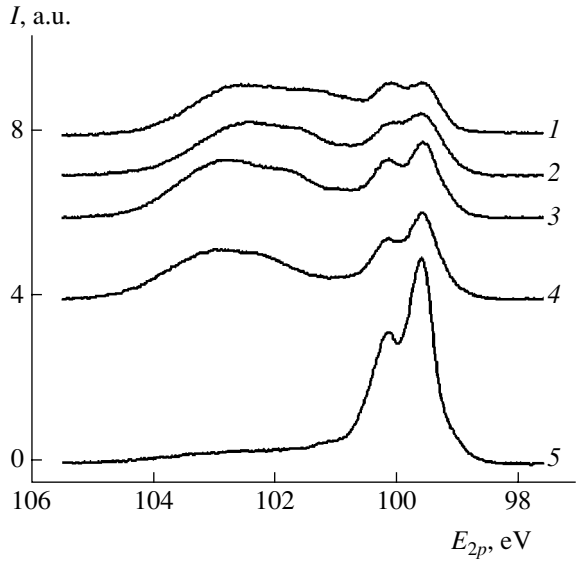

Fig. 2. Si 2*p* photoelectron spectra ($h\nu$ = 130 eV) of a silicon surface upon oxidation and deposition of 8 ML of cobalt (*1*) in the initial state and (*2*–*5*) upon subsequent annealing to 250, 400, 750, and 850°C, respectively.

terized by a binding energy close to that of pure silicon. For this mode, the energy shift is positive and amounts to ~250 meV [15–18]. The superposition of silicon and disilicide modes also accounts for the observed decrease in spacing between the two Si 2*p* peaks.

The process of silicide formation in the system under consideration occurs in a range of temperatures up to about 400°C. Further increase (up to ~750°C) is also accompanied by some, but not very significant, transformation of the photoelectron spectrum. Comparison of the obtained results to the data reported previously [18] for the Co/Si system shows that the temperature interval of the solid-phase reaction of $CoSi_2$ synthesis is virtually the same in the presence and in the absence of oxygen.

In the temperature range from 250 to 750°C, the oxide modes of the Si 2*p* signal exhibit no qualitative changes. There are certain transformations in the corresponding energy interval related to redistribution of the particular oxide components, whereby the modes of higher valence increase and the modes of lower valence decrease. On the whole, the oxide layer is retained in the entire temperature range of the solid-phase synthesis of $CoSi_2$ and, hence, the reaction of silicide formation proceeds under this oxide layer. Therefore, the oxide layer cannot play the role of a diffusion barrier for cobalt atoms (in contrast to what was suggested in [1, 20]) in the course of silicide formation.

Disappearance of the oxide modes is observed when the annealing temperature is increased to 850°C. Simultaneously, the intensity of the other spectral components significantly increases, since the corresponding signals are no longer attenuated by the oxide film covering the sample surface. As a result, the shape of lines in the spectrum becomes very much like that in the Si 2*p* spectrum of an epitaxial film of cobalt disilicide formed on the surface of silicon in the absence of oxygen [18]. The main difference is the absence of the surface mode (characteristic of the Co/Si system) due to the upper atoms of silicon dimers, which is related to partial removal of these atoms from the substrate surface. In our case, this is evidence of improved morphology of the cobalt disilicide layer formed on the surface of oxidized silicon.

The obtained results show evidence of the following mechanism by which oxygen influences the process of silicide formation in the system studied. As is known, the solid-phase synthesis of cobalt disilicide on the Si(100)2 × 1 surface usually leads to the formation of $CoSi_2$ grains misoriented relative to the substrate, for example, $CoSi_2$(221) [1, 3]. This is related to the mass transfer and faceting of the substrate material, which hinders the epitaxial growth of a $CoSi_2$(100) film and impairs its morphology [1–3]. The presence of an oxide layer on the initial sample surface spatially confines the region where the reaction of silicide formation proceeds and hinders atomic rearrangements involving changes in the phase volume. Apparently, this is the positive role of preliminary oxidation of a single crystal silicon surface.

Acknowledgments. The work was supported in part by the Russian Foundation for Basic Research (project no. 01-02-17288), the Ministry of Industry, Science, and Technology of the Russian Federation (project no. 40.012.1.1.1152), and the Russian–German Laboratory at BESSY II.

REFERENCES

1. J. R. Jimenez, L. J. Schowalter, L. M. Hsiung, *et al.*, J. Vac. Sci. Technol. A **8**, 3014 (1990).
2. C. W. T. Bulle-Lieuwma, A. H. van Ommen, J. Hornstra, and C. N. A. M. Aussems, J. Appl. Phys. **71**, 2211 (1992).
3. M. V. Gomoyunova, I. I. Pronin, D. A. Valdaitsev, *et al.*, Phys. Low-Dimens. Semicond. Struct. **3**/**4**, 163 (2002).
4. T. R. Tung, Appl. Phys. Lett. **68**, 3461 (1996).
5. T. R. Tung, Jpn. J. Appl. Phys. **36**, Part 1, 1650 (1997).
6. Y. Hayashi, M. Yoshinaga, H. Ikeda, *et al.*, Surf. Sci. **438**, 116 (1999).
7. A. Ishizaka and Y. Shiraki, J. Electrochem. Soc. **133**, 666 (1986).
8. E. Landemark, C. J. Karlsson, Y.-C. Chao, and R. I. G. Uhrberg, Phys. Rev. Lett. **69**, 1588 (1992).
9. T.-W. Pi, I.-H. Hong, C.-P. Cheng, *et al.*, J. Electron Spectrosc. Relat. Phenom. **107**, 163 (2000).
10. H. Koh, J. W. Kim, W. H. Choi, and H. W. Yeom, Phys. Rev. B **67**, 073306 (2003).

11. M. V. Gomoyunova, I. I. Pronin, N. R. Gall, *et al.*, Pis'ma Zh. Tekh. Fiz. **29** (12), 25 (2003) [Tech. Phys. Lett. **29**, 496 (2003)].

12. G. Hollinger and F. J. Himpsel, Phys. Rev. B **28**, 3651 (1983).

13. Y. Hoshino, T. Nishimura, T. Nakada, *et al.*, Surf. Sci. **488**, 249 (2001).

14. P. Morgen, T. Jensen, C. Gundlach, *et al.*, Comput. Mater. Sci. **21**, 481 (2001).

15. J. M. Gallego, R. Miranda, S. Molodtsov, *et al.*, Surf. Sci. **239**, 203 (1990).

16. G. Rangelov, P. Augustin, J. Stober, *et al.*, Phys. Rev. B **49**, 7535 (1994).

17. G. Rangelov and Th. Fauster, Surf. Sci. **365**, 403 (1996).

18. M. V. Gomoyunova, I. I. Pronin, N. R. Gall, *et al.*, Fiz. Tverd. Tela (St. Petersburg) **45**, 1519 (2003) [Phys. Solid State **45**, 1596 (2003)].

19. H. W. Yeom, H. Hamamatsu, T. Ohta, and R. I. G. Uhrberg, Phys. Rev. B **59**, R10413 (1999).

20. F. Takahashi, T. Irie, J. Shi, *et al.*, Appl. Surf. Sci. **169**, 315 (2001).

Translated by P. Pozdeev

Technical Physics Letters, Vol. 30, No. 10, 2004, pp. 854–856. Translated from Pis'ma v Zhurnal Tekhnicheskoĭ Fiziki, Vol. 30, No. 20, 2004, pp. 25–29.

A Multichannel Energy Filter Comprising a Cylinder with Closed Ends and an Axial Filament Electrode

L. P. Ovsyannikova* and T. Ya. Fishkova

Ioffe Physicotechnical Institute, Russian Academy of Sciences, St. Petersburg, 194021 Russia

** e-mail: L.Ovsyannikova@mail.ioffe.ru*

Received April 28, 2004

Abstract—A new electrostatic multichannel deflector providing energy filtration of charged particles is proposed. The device comprises a cylinder with closed ends and an axial filament electrode. The potential profile in the system is analytically calculated. The main parameters of the energy filter are calculated for a charged particle beam injected and extracted via grounded end faces. Owing to a small azimuthal beam size compared to the cylinder perimeter, the proposed system is quite compatible with one- to four-channel dynamical monopole mass spectrometers, providing energy-filtered beam deflection to a detector. © *2004 MAIK "Nauka/Interperiodica".*

Previously [1], we have studied a cylindrical capacitor with an inner electrode of small radius and two grounded flat end electrodes through which a beam of charged particles is injected and extracted. Then [2] we calculated an energy analyzer of the cylindrical mirror type with grounded end plates, the electron-optical parameters of which have proved to be close to those of a classical cylindrical mirror with second-order focusing and an entrance angle of 42.3° for the source and detector arranged on the axis of rotational symmetry of the system. The results of our previous investigations showed that introduction of the end electrodes does not impair the properties of cylindrical systems with open ends; moreover, these electrodes prevent the system from penetration of the external fields.

This study was aimed at a theoretical description of the electrostatic cylindrical system providing deflection of a charged particle beam injected at one end toward an external cylinder at the opposite end. This configuration can be used in a system with several sources of charged particles arranged in the azimuthal direction—in particular, in spatially matched one- to four-channel dynamical monopole mass spectrometers, where each channel is formed by two electrodes forming a 90°-dihedral angle and a cylindrical electrode situated opposite to the apex. The proposed system, arranged at the exit of such a mass spectrometer, provides for the filtration of a particle beam with respect to the energy and prevents the admission of undesired fast charged particles, photons, and neutrals, thus increasing the sensitivity threshold of the measuring system.

Consider a system comprising two coaxial cylinders, with the grounded external cylinder of radius R and two end electrodes and an infinitely small gap l between the end electrodes and a central (field-generating) filament electrode of radius ρ. The electrostatic potential distribution in this device is described by the function

$$\Phi(r, z) = 4\frac{V}{z}\sum_{n=0}^{\infty}\frac{[K_0(\xi_2)I_0(\xi) - I_0(\xi_2)K_0(\xi)]}{K_0(\xi)I_0(\xi_1) - I_0(\xi_2)K_0(\xi_1)}\frac{\sin(\zeta)}{(2n+1)}, \quad (1)$$

where V is the filament electrode potential; $\xi = (2n + 1)\pi r/L$; $\zeta = (2n + 1)\pi z/L$; L is the distance between end electrodes; ξ_1 and ξ_2 are the values of ξ for $r = R$ and ρ, respectively; and I_0 and K_0 are the zero-order modified Bessel functions. It was established that the series in this expression converges quite rapidly and the potential can be determined to within three digits using only the first two terms, provided that the filament electrode is sufficiently thin (R/ρ = 20–200) and the system length is such that L/R = 1–4. The values of the potential obtained using formula (1) were compared to the results of numerical calculations performed using the TEO program developed by the authors. Figure 1 shows the potential profiles in a system with R/ρ = 100 and L/R = 2.5 (the longitudinal axis z is the rotational symmetry axis). In the working region carrying the beam of charged particles ($r \geq 0.4R$), the difference between the results of analytical and numerical calculations does not exceed 5%.

Figure 2 shows the particle trajectories in a beam entering the system parallel to the rotational symmetry axis. This shape of the trajectories is related to the effect of a retarding potential applied to the filament electrode (with grounded external cylinder and end electrodes).

1063-7850/04/3010-0854$26.00

Parameters of the deflecting cylindrical energy filter

L/R	β	r_a/R	r_0/R	s_0/R	r_b/R	s/R	λ/R	D/R	δ, %
1.5	3.0	0.61	0.56–0.66	0.1	0.933	6.6×10^{-3}	0.15	0.34	1.9
			0.52–0.72	0.2		2.3×10^{-2}	0.31		6.8
			0.48–0.78	0.3		5.2×10^{-2}	0.46		15.3
2.0	1.5	0.56	0.51–0.61	0.1	0.939	5.1×10^{-3}	0.17	0.39	1.3
			0.46–0.66	0.2		2.2×10^{-2}	0.33		5.6
			0.43–0.73	0.3		4.6×10^{-2}	0.50		11.8
2.5	0.9	0.52	0.47–0.57	0.1	0.937	5.0×10^{-3}	0.18	0.42	1.2
			0.43–0.63	0.2		2.0×10^{-2}	0.36		4.8
			0.39–0.69	0.3		4.3×10^{-2}	0.54		10.4
3.0	0.6	0.50	0.45–0.55	0.1	0.934	4.9×10^{-3}	0.19	0.43	1.2
			0.40–0.60	0.2		1.8×10^{-2}	0.37		4.2
			0.36–0.66	0.3		4.1×10^{-2}	0.56		9.5

The system geometry was selected so as to provide for the sharpest focusing at the exit end near the cylindrical electrode. For this purpose, the ratio of the radii of cylindrical and filament electrodes must be large (R/ρ = 50–200) and the distances between the end electrodes and the filament must be small (we used $l = 0.1R$). Previously, we established that the focusing effect disappears at $l \approx R - \rho$. The length of the system was used as a variable parameter. The trajectories of positive singly charged particles in this cylindrical system were numerically calculated using the TEO program.

Parameters of the system with $R/\rho = 100$ and various lengths ($1.5 \le L/R \le 3.0$) are presented in the table, where $\beta = eV/\varepsilon$ is the energy filter strength (e is the electron charge and ε the initial beam energy); r_a and r_b are the entrance and exit coordinates of the main trajectory around which the focusing takes place, respectively; r_0 are the coordinate of the extreme trajectories for various values of the entrance slit width s_0; s is the corresponding exit slit width in the meridional plane on the exit end electrode; and $\lambda = (s_0 r_b)/r_a$ is the azimuthal size of the exit slit. The table also gives the values of the energy dispersion D and the energy resolution $\delta = \Delta\varepsilon/\varepsilon$. All linear dimensions are indicated relative to the cylinder radius.

As can be seen from the table, an increase in the system length leads to a rapid decrease in the force required for the beam focusing at the external cylinder, to a somewhat sharper focusing and greater dispersion, and to a corresponding increase in the energy resolution. Note that the ratio of the entrance and exit slit widths M is significantly smaller than unity. For a small entrance slit width $s_0 = 0.1R$, we have $M = (7–5)\times10^{-2}$; for a medium slit, $s_0 = 0.2R$ and M = 0.12–0.09; and for a large slit, $s_0 = 0.3R$ and M = 0.17–0.14.

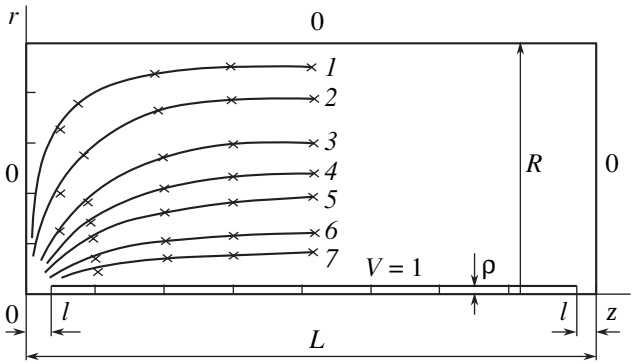

Fig. 1. The pattern of the potential distribution in a cylindrical system with an axial filament electrode for R/ρ = 100, L/R = 2.5, and $\Phi(r, z)/V$ = 0.02 (*1*), 0.05 (*2*), 0.1 (*3*), 0.15 (*4*), 0.2 (*5*), 0.3 (*6*), and 0.4 (*7*): (solid curves) numerical calculation; (crosses) analytical calculation by formula (1).

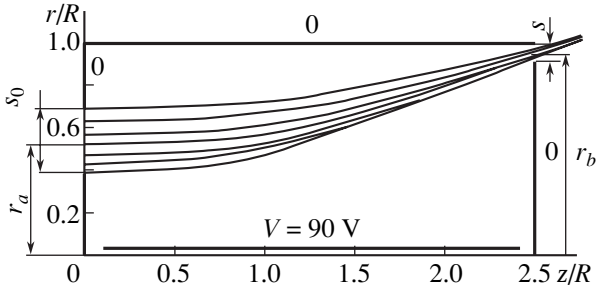

Fig. 2. Trajectories of positive singly charged particles in a deflecting cylindrical energy filter tuned to ε = 100 eV.

In conclusion, it should be noted that the proposed cylindrical system with an axial filament electrode has a large aperture, which makes it possible to work with wide charged particle beams. This is especially important in the case of operation with monopole mass spectrometers. In addition, a change in the filament radius for the same external cylinder within $R/\rho = 50–200$ influences the system parameters rather weakly. It is possible to use the geometric scaling laws and vary the filament radius so as to obtain the desired system dimensions. While the geometric parameters are scaled, the electrical characteristics remain unchanged.

REFERENCES

1. L. P. Ovsyannikova, S. V. Pasovets, and T. Ya. Fishkova, Zh. Tekh. Fiz. **62** (12), 171 (1992) [Sov. Phys. Tech. Phys. **37**, 1215 (1992)].
2. L. P. Ovsyannikova and T. Ya. Fishkova, Zh. Tekh. Fiz. **64** (10), 174 (1994) [Tech. Phys. **39**, 1072 (1994)].

Translated by P. Pozdeev

Technical Physics Letters, Vol. 30, No. 10, 2004, pp. 857–858. Translated from Pis'ma v Zhurnal Tekhnicheskoĭ Fiziki, Vol. 30, No. 20, 2004, pp. 30–34.

The Effect of Alternating Current on the Thermal Activation Threshold of the Tunnel Josephson Junctions

I. N. Askerzade

Institute of Physics, National Academy of Sciences of Azerbaijan, Baku, Azerbaijan
Department of Physics, Ankara University, 06100 Tangodan, Ankara, Turkey
e-mail: solstphs@physics.ab.az; iasker@science.ankara.edu.tr

Received April 16, 2004

Abstract—The process of thermal activation in the tunnel Josephson junctions simultaneously carrying both constant (dc) and alternating (ac) currents has been studied. The presence of the ac component leads to a decrease in the potential barrier for a metastable state of the Josephson junction. The thermal activation threshold is expressed as a function of the ac current amplitude. The results agree with the data of recent experiments on the statistics of switching from a superconducting to resistive state in the Josephson tunneling junctions. © *2004 MAIK "Nauka/Interperiodica".*

The Josephson junctions exhibit macroscopic quantum behavior at low temperatures [1]. In recent years, such effects have received much attention from researchers [2, 3]. In the case when the capacitance of a Josephson junction is large, that is, the MacCumber–Stewart parameter β is large [1] ($\beta = (2e/\hbar)I_c R_N^2 C \gg 1$, where R_N and C are the normal resistance and capacitance of the junction and I_c is the critical current), the junction may exhibit plasma phase oscillations on the bottom of the normalized potential well, $u(\phi) = (-i\phi - \cos\phi)$ (see the figure). Here, $u(\phi)$ is measured in Josephson energy units ($E_J = \hbar I_c/2e$) and the dc current I, in I_c units. The frequency of these oscillations depends on the dc current I and is given by the formula (see, e.g., [4])

$$\omega_p = \left(\frac{2eI_c}{\hbar C}\right)^{1/2}(1 - i^2)^{1/4}. \quad (1)$$

This dependence was originally observed by Dahm *et al.* [5] for the Josephson junctions connected to a dc voltage source. The validity of relation (1) confirms the sinusoidal relation between current and phase in the Josephson junctions. The lifetime of the state on the potential well bottom is determined by the Kramers formula [6] $\tau = (2\pi/\omega_A)\exp(-\Delta u/kT)$ [6], where ω_A is the so-called attempt frequency [1]. In the case of the Josephson tunneling junctions with $\beta \gg 1$, the value of ω_A coincides with the plasma frequency ω_p. For a dc current, the potential barrier height is given by the formula $\Delta u = (3/2)(1 - i^2)^{3/2}$ (see the inset in the figure).

Recently, Gronbech-Jensen *et al.* [7] studied the lifetime of a metastable state in the tunnel Josephson junctions simultaneously carrying dc and ac currents, confirmed the validity of relation (1), and determined the effect of the ac component on the thermal activation threshold. It was experimentally demonstrated that this threshold decreases with increasing ac current amplitude. However, no theoretical analysis of this behavior was presented.

This study was aimed at a theoretical investigation of the effect of alternating current on the potential barrier height and, hence, on the thermal activation threshold of the tunnel Josephson junction simultaneously

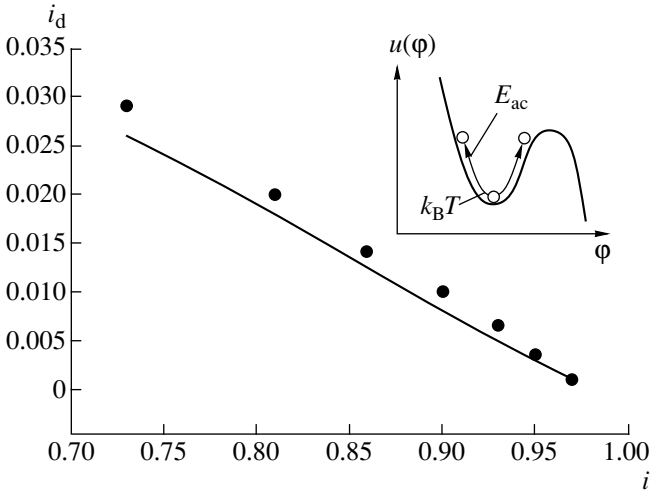

Dependence of the thermal activation threshold of a Josephson junction on the ac current amplitude: (black circles) experimental data from [7]; (solid curve) calculation using formula (6). The inset shows a plot of the potential energy $u(\phi) = (-i\phi - \cos\phi)$ versus the phase difference ϕ for the Josephson junction carrying dc and ac currents.

1063-7850/04/3010-0857$26.00 © 2004 MAIK "Nauka/Interperiodica"

carrying dc and ac currents. The obtained results agree with the experimental data [7].

The dynamics of a Josephson junction in an external circuit is described, with allowance for the thermal fluctuations, by the following equations [4]:

$$\ddot{\phi} + \alpha\dot{\phi} + \sin\phi = i + i_d\sin(\omega_d t) + \xi(t), \quad (2a)$$

$$\langle\xi(t)\xi(t')\rangle = 4\frac{kT}{E_J}\delta(t-t'), \quad \langle\xi(t)\rangle = 0, \quad (2b)$$

where ϕ is the Josephson phase; i and i_d are the dc and ac (drive) current components expressed in units of the critical current I_c; ω_d is the applied field frequency expressed in units of the plasma frequency at a zero dc current, $\omega_p(i=0) = (2eI_c/\hbar C)^{1/2}$; and $\xi(t)$ is the fluctuation current component. Below, we consider only the δ-correlated thermal fluctuations.

For evaluating the lifetime of the metastable state, let us separate the slow and fast phase motions as $\phi = \phi_0 + \phi_1$. Here, the fast phase component ϕ_1 satisfied the equation

$$\ddot{\phi}_1 + \alpha\dot{\phi}_1 = i_d\sin\omega_d t, \quad (3)$$

while the slow phase component ϕ_0 only weakly varies during the ac current period. Equation (3) follows from equations of state (2) because the term with $\sin\phi$ yields zero when averaged over the period. The solution of this equation can be expressed as

$$\phi_1 = -\frac{i_d}{\alpha^2+\omega_p^2}\sin\omega_p t - \frac{\alpha}{\omega_p}\frac{i_d}{\alpha^2+\omega_p^2}\cos\omega_p t. \quad (4)$$

For further analysis of thermal activation in the tunnel Josephson junctions, it is necessary to determine the form of the potential $u(\phi) = (-i\phi - \cos\phi)$ averaged over the ac field period. Using formulas [8]

$$\cos(a\sin\Omega t) = \sum_n A_n e^{in\Omega t}, \quad A_n = J_{2k}(a), \quad n = 2k,$$
$$\sin(a\sin\Omega t) = \sum_n B_n e^{in\Omega t}, \quad B_n = J_{2k+1}(a), \quad n = 2k+1, \quad (5)$$

and averaging over the period, we eventually obtain the following expression for the effective potential:

$$u_{\text{eff}}(\phi) = -J_0\left(\frac{i_d}{\alpha^2+\omega_p^2}\right)J_0\left(\frac{\alpha}{\omega_p}\frac{i_d}{\alpha^2+\omega_p^2}\right)\cos\phi - i\phi, \quad (6)$$

where $J_0(x)$ is the zero-order Bessel function. Thus, the presence of the ac component leads to renormalization of the Josephson potential $u(\phi) = (-i\phi - \cos\phi)$. Formula (6) clearly shows that the potential barrier height decreases with increasing amplitude of the alternating current component i_d.

The results of calculations using formula (6) are presented in the figure by a solid curve, in comparison to the experimental data (black circles) taken from [7]. Since the energy barrier height Δu decreases with increasing current in the Josephson junction, the action of thermal fluctuations will switch the system from superconducting to resistive state at a current somewhat lower than $I(t) = I_c$. The statistics of such switching was, experimentally measured in [7], where this method, offering a powerful tool for determining the nature of the potential barrier, was used for studying the classical and quantum behavior of the tunnel Josephson junctions [1, 4]. The measurements in [7] were performed for low-temperature tunnel junctions of the Nb–$NbAlO_x$–Nb type with the switching statistics determined for 10000 events. By changing the ac current amplitude, it was possible to control the dc current corresponding to a peak in the distribution of switching events. As can be seen from the figure, the experimental dependence of $i_d(i)$ agrees well with the results of calculations based on the model considered above.

In conclusion, a theory of the thermal activation of Josephson junctions simultaneously carrying both constant (dc) and alternating (ac) currents was developed. It was demonstrated that the presence of an ac current component leads to a decrease in the potential barrier height for a metastable state, thus facilitating thermal activation in the tunnel Josephson junctions. The results of calculations agree well with the published experimental data.

Acknowledgments. The author is grateful to Prof. C. Aydin and Prof. S. Atag for support of this investigation.

REFERENCES

1. K. K. Likharev, *Introduction to the Dynamics of Josephson Junctions* (Nauka, Moscow, 1985) [in Russian].
2. *Quantum Mesoscopic Phenomena and Mesoscopic Devices in Microelectronics*, Ed. by I. O. Kulik and R. Ellialtioglu (Kluwer, Dordrecht, 2000).
3. C. Cosmelli, P. Carelli, M. G. Castelliano, *et al.*, Supercond. Sci. Technol. **16**, 1337 (2003).
4. A. Barone and G. Paterno, *Physics and Applications of the Josephson Effect* (Wiley, New York, 1982; Mir, Moscow, 1984).
5. A. J. Dahm, A. Denenstein, T. F. Finnegan, *et al.*, Phys. Rev. Lett. **20**, 859 (1968).
6. H. Kramers, Physica **7**, 284 (1940).
7. N. Gronbech-Jensen, M. G. Castelliano, F. Chiarello, *et al.*, cond-mat/0403245.
8. G. A. Korn and T. M. Korn, *Mathematical Handbook for Scientists and Engineers* (McGraw-Hill, New York, 1968).

Translated by P. Pozdeev

Technical Physics Letters, Vol. 30, No. 10, 2004, pp. 859–861. Translated from Pis'ma v Zhurnal Tekhnicheskoĭ Fiziki, Vol. 30, No. 20, 2004, pp. 35–41.

Subnanosecond Electron Beams Formed in a Gas-Filled Diode at High Pressures

S. B. Alekseev, V. P. Gubanov, V. M. Orlovskiĭ, and V. F. Tarasenko*

Institute of High-Current Electronics, Siberian Division, Russian Academy of Sciences, Tomsk, Russia

** e-mail: VFT@loi.hcei.tsc.ru*

Received April 19, 2004

Abstract—Subnanosecond electron beams can be formed in gas-filled diodes at high pressures (up to 6 and 4 bar in helium and nitrogen, respectively). In a diode filled with air at atmospheric pressure, a beam current amplitude above 240 A was obtained at a pulse duration (FWHM) of ~0.2 s and a beam current density of ~40 A/cm^2. © *2004 MAIK "Nauka/Interperiodica".*

Introduction. Previously, we demonstrated that high-current subnanosecond electron beams can be obtained in gas diodes filled with molecular or atomic gases and their mixtures at pressures of up to 1 atm [1–6]. For example, a beam current amplitude reached behind a 40-μm-thick AlBe foil was as high as ~70 A in air and ~200 A in helium at a pulse duration (full width half height, FWHM) not exceeding 0.3 ns, while the reduced field $E/p = U/dp$ averaged over the interelectrode gap was as small as ~0.1 kV/(cm Torr), where E is the electric field strength, p is the gas pressure, U is the voltage applied to the gap, and d is the gap width. The latter parameter was much smaller than the critical value of E_{cr}/p predicted for the formation of runaway electrons [7].

In order to explain these results, it was suggested [1, 3, 4] that the critical field is reached near the anode when the plasma expands due to the ionization front propagating from cathode to anode. Such a subnanosecond electron beam with an amplitude of several dozen amperes obtained in an air-filled diode at 1 atm was referred to as a subnanosecond avalanche electron beam (SAEB) [4]. However, experiments at still higher pressures were not performed and it was unclear whether such high-current beams can be obtained in gas-filled diodes at pressures above atmospheric. It might be expected that, if the mechanism suggested in [1, 3, 4] was valid, further increase in the pressure would not significantly influence the conditions of formation of subnanosecond electron beams in gas-filled diodes. Indeed, as the pressure increases, the critical field strength [5, 7] can still be reached at a proportionally smaller distance from the plasma (spreading from cathode) to the anode. For this assumption to be valid, increased pressure in the diode should not disturb the volume character of discharge during a period of time of about ~1 ns.

This study was aimed at determining the possibility of electron beam formation in a gas-filled diode at pressure above atmospheric.

Experimental. The experiments were performed in systems employing two generators, capable of forming voltage pulses with a duration of 1–2 ns and a front width of ~0.5 ns and below, and two gas-filled diodes of different design. Both diodes comprised a flat anode and a small-size cathode, which ensured additional field amplification near the cathode. The system with generator 1 (of the modified SINUS type [8]) also comprised an additional transmitting line with a wave impedance of 40 Ω and allowed the pressure of helium and nitrogen in the diode to be increased up to 6 atm. The modified generator formed on a matched 40-Ω load a voltage pulse with an amplitude of ~180 kV, an FWHM ~ 1.5 ns, and a front width of ~0.5 ns. In this diode, cathode 1 comprised a set of three coaxial cylinders (12, 22, and 30 mm in diameter) made of a 50-μm-thick titanium foil, embedded into one another [1–3].

Generator 2 (similar to RADAN-220 [9]) produced in the discharge gap a voltage pulse with an amplitude of up to ~200 kV at a shorter pulse duration, FWHM ~ 1 ns. The gas diode in this system was characterized by minimum dimensions (for the given conditions) and minimum inductance. Generator 2 was loaded on a diode filled with air at atmospheric pressure and equipped with cathode 2, representing a steel tube with a diameter of 6 mm and a wall thickness of 50 μm [4]. The anode in both diodes was made of 40-μm-thick AlBe foil. The cathode–anode spacing in both systems could be varied within 10–20 mm.

Signals from the capacitive voltage divider, the electron beam collectors, and shunts were measured using a 4-GHz digital oscillograph of the TDS-7405 type at a sweep of 20 G/s, which corresponds to 20 points/ns. The diode discharge could be photographed by a digital camera via a grid in the output window.

1063-7850/04/3010-0859$26.00 © 2004 MAIK "Nauka/Interperiodica"

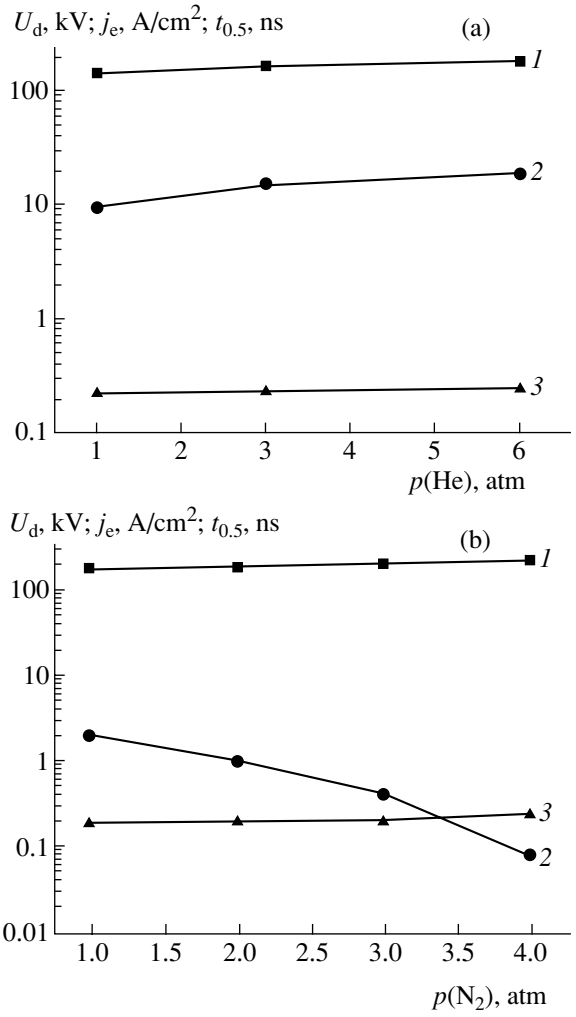

Fig. 1. Plots of (*1*) the discharge voltage amplitude U_d across the gap, (*2*) the beam current density j_e, and (*3*) the current pulse duration $t_{0.5}$ = FWHM versus gas pressure for a diode filled with (a) helium and (b) nitrogen and powered by generator 1.

Results. The experiments were performed in a significantly expanded range of gas pressures used for the electron beam formation. In particular, an electron beam was obtained for the first time in a gas-filled diode operating at a pressure of 6 atm. Figure 1 shows the pressure dependences of the voltage amplitude across the gap, the beam current density, and the current pulse duration (FWHM) measured using generator 1 and a diode filled with (a) helium and (b) nitrogen. As can be seen from these data, the current pulse amplitude and duration (FWHM) remain virtually unchanged as the helium pressure increases from 1 to 6 atm. The discharge under these conditions retained the volume character (Fig. 2a). A decrease in the beam current observed in the case of nitrogen at a pressure of 2–4 atm was related to a decrease of the region occupied by the volume discharge and to contraction of the discharge at a pressure of ~4 atm.

The duration of beam current pulses measured at an ~0.1 ns resolution in helium and nitrogen was virtually the same (FWHM ~ 0.2 ns). It was found that the current pulse duration depended on the collector and was minimum for a small-size collector. Apparently, the plasma (expanding due to the ionization front propagating away from the cathode) does not reach the anode simultaneously at various points. As a result, the time to attaining the critical field also exhibits a certain scatter and the total current pulse duration is greater than the width of a current pulse collected from a small area. The average electron beam energy behind the foil for generator 1 and the diode filled with helium to p = 1–6 atm was ~70 keV. All these results confirm the assumption [1, 3, 4] concerning the electron beam formation in the region between the plasma (expanding due to the ionization front propagating away from the cathode) and the anode upon reaching the critical value of the reduced field.

We observed a very strong dependence of the beam current amplitude behind the foil on the size and inductance of the gas diode. In the experiments with generator 2 and cathode 2 in the diode filled with air at atmospheric pressure, the beam current amplitude behind the foil in the case of a minimum inductance was ~240 A at an FWHM ~ 0.2 ns. The photograph of the electron beam induced luminescence in this case is presented in Fig. 2b. As can be seen, the beam has a diameter in excess of 4 cm and contains a central region with a diameter of ~1.5 cm and a large current density (on average, ~40 A/cm^2). We believe that the very small amplitudes of the beam current pulses observed in gas-filled diodes at atmospheric pressure (see review [10]) are related to a large inductance of these gas diodes.

Discussion. The obtained results can be interpreted as follows. When a voltage pulse with a leading front width not exceeding 1 ns is applied to the gap, the electric field strength at the cathode (possessing a small radius of curvature) is maximum and electrons are injected into the gap, first, due to the field emission (enhanced by positively charged ions) and, then, due to the explosive electron emission. The effect of field amplification at the cathode surface is sufficiently strong for generation of fast electrons. These fast electrons provide for the preionization in the gap, the formation of volume discharge in the cathode region, and the expansion of plasma at a velocity of ~10^9 cm/s due to the ionization front propagating toward the anode. At the boundary of the expanding plasma, electrons are partly accelerated due to the positive voltage on the anode and due to their repulsion from the surface of the electron cloud. This mechanism accounts for the formation of a subnanosecond electron beam.

The leading front of the beam current pulse is determined by the leading front of the applied voltage pulse, which has a subnanosecond width. Moreover, due to a decrease in the distance from plasma to anode and an

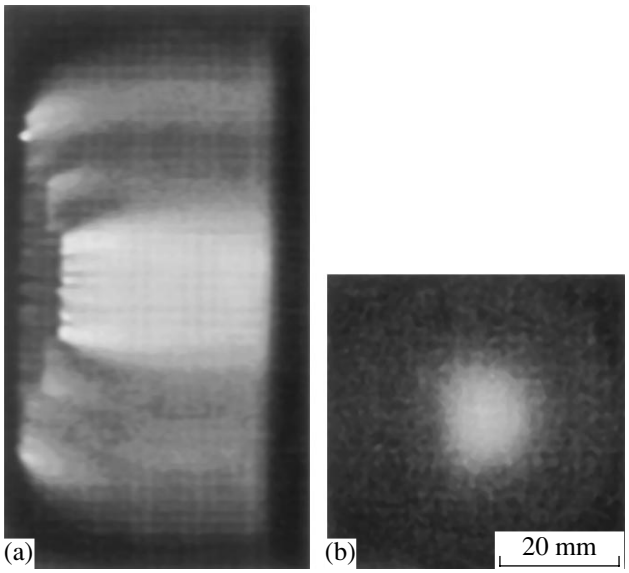

Fig. 2. Photographs of (a) the discharge in helium at a pressure of 6 atm and a gap width of 16 mm (generator 1) and (b) the electron-beam-induced luminescence in a diode filled with air at atmospheric pressure (generator 2).

additional enhancement of the electric field at the front of the voltage pulse between plasma and anode, the width of the leading front of the current pulse is even smaller than that of the voltage pulse. A subnanosecond width of the trailing front of the current pulse is determined by the large velocity of plasma propagation upon attaining the critical field strength in a local region near the anode and upon leveling of the electric field strength in the gap after plasma arrival at the anode. According to this mechanism, conditions for the formation of subnanosecond electron beams can be realized in different gases at various (including high) pressures. It should be stressed that maximum beam current amplitudes in the gas-filled diodes are obtained under the conditions of a volume discharge.

Conclusion. Thus, the results of our investigation demonstrated for the first time that the conditions of subnanosecond electron beam generation in a gas-filled diode are retained when the gas pressure is increased up to 6 atm for helium and 4 atm for nitrogen (and even these values are not limiting). The bombardment of the anode by fast electrons may lead to the creation of anode plasma, after which the critical field strength is attained in a region between the cathode and anode plasma.

Acknowledgments. The authors are grateful to S.D. Korovin for support of this investigation.

REFERENCES

1. S. B. Alekseev, V. M. Orlovskiĭ, and V. F. Tarasenko, Pis'ma Zh. Tekh. Fiz. **29** (10), 29 (2003) [Tech. Phys. Lett. **29**, 411 (2003)].
2. S. B. Alekseev, V. M. Orlovskiĭ, and V. F. Tarasenko, Pis'ma Zh. Tekh. Fiz. **29** (16), 45 (2003) [Tech. Phys. Lett. **29**, 679 (2003)].
3. S. B. Alekseev, V. P. Gubanov, V. M. Orlovskiĭ, *et al.*, Prib. Tekh. Éksp., No. 4, 81 (2003).
4. V. F. Tarasenko, V. M. Orlovskiĭ, and A. A. Shunaĭlov, Izv. Vyssh. Uchebn. Zaved., Fiz., No. 3, 94 (2003).
5. V. F. Tarasenko, S. I. Yakovlenko, V. M. Orlovskiĭ, *et al.*, Pis'ma Zh. Éksp. Teor. Fiz. **77**, 737 (2003) [JETP Lett. **77**, 611 (2003)].
6. V. F. Tarasenko, V. G. Shpak, S. A. Shunaĭlov, *et al.*, Pis'ma Zh. Tekh. Fiz. **29** (21), 1 (2003) [Tech. Phys. Lett. **29**, 879 (2003)].
7. A. N. Tkachev and S. I. Yakovlenko, Pis'ma Zh. Éksp. Teor. Fiz. **77**, 264 (2003) [JETP Lett. **77**, 221 (2003)].
8. V. P. Gubanov, S. D. Korovin, I. V. Pegel', *et al.*, Izv. Vyssh. Uchebn. Zaved., Fiz., No. 12, 110 (1996).
9. M. I. Yalandin and V. G. Shpak, Prib. Tekh. Éksp., No. 3, 5 (2001).
10. L. P. Babich, T. V. Loĭko, and V. A. Tsukerman, Usp. Fiz. Nauk **160** (7), 49 (1990) [Sov. Phys. Usp. **33**, 521 (1990)].

Translated by P. Pozdeev

Technical Physics Letters, Vol. 30, No. 10, 2004, pp. 862–864. Translated from Pis'ma v Zhurnal Tekhnicheskoĭ Fiziki, Vol. 30, No. 20, 2004, pp. 42–49.

The Temperature Dependence of the Strength of Adhesion between Steels and Epoxy-Rubber Glues and Polyamides in a Rubberlike State

V. I. Vettegren[a,*], V. B. Kulik[a], A. Ya. Bashkarev[b], A. A. Lebedev[b], and V. A. Sytov[c]

[a] *Ioffe Physicotechnical Institute, Russian Academy of Sciences, St. Petersburg, 194021 Russia*
[b] *St. Petersburg State Technical University, St. Petersburg, 195251 Russia*
[c] *Central Research Institute for Materials, St. Petersburg, Russia*
** e-mail: Victor.Vettegren@mail.ioffe.ru*
Received April 28, 2004

Abstract—We have studied the temperature dependence of the strength of adhesion between steel 45 and epoxy-rubber glues and polyamide coatings in a rubberlike (high elasticity) state, measured at a fixed loading rate. An empirical relationship is established between the adhesion strength σ and the temperature above the glass transition point. *© 2004 MAIK "Nauka/Interperiodica".*

Introduction. The adhesion strength σ is one of the main characteristics of polymeric adhesive coatings and joints. As is known [1–6], the strength of adhesion between metals, crystals, polymers, etc., is related to the temperature T and the time to fracture (lifetime) τ by the Zhurkov equation

$$\sigma = \frac{U_0}{\gamma} - \frac{k_B T}{\gamma} \ln \frac{\tau}{\tau_0}, \quad (1)$$

where $\tau_0 \approx 10^{-13}$ s, U_0 is the activation energy for the rupture of interatomic bonds, γ is a parameter related to the activation volume of bond rupture, and k_B is the Boltzmann constant.

Previously [7], we have studied the temperature dependence of the strength of adhesion between epoxy-rubber glues and steel 45 in a temperature range from 20 to 450 K. It was established that the value of σ for the steel and glues studied obeys Eq. (1) only in the region of $T < T_g$, where T_g is the glass transition temperature for a given glue.

This study was aimed at elucidating the nature of deviations from Eq. (1) at temperatures above the glass transition point ($T > T_g$).

Experimental. We have studied the temperature dependence of the strength of adhesion between steel 45 and a series of glues and polyamides: KDS-19 (a block copolymer of epoxidian resin, butadiene-nitrile carboxylated rubber, and *metha*-tri(carborane sebacate)glycide); K-300 (an organosilicon resin cured with a low-molecular-weight polymer); KVS-31 (a block copolymer of epoxidian resin, low-molecular-weight butadiene-nitrile rubber with terminal carboxy groups); polyamide 6; polyamide 66; and polyamide 66/6.

The samples comprised pairs of steel cylinders with a diameter of 1 cm and a length of 2.5 cm glued together by their edge faces. Prior to gluing, the edge faces of the steel cylinders were mirror finished. Then, a layer of glue or a polyamide melt was applied and the cylinders were placed into a special device ensuring matching of the cylinder axes and providing for the required pressing load. Until termination of the glue polymerization and polyamide solidification process, the samples were kept in this device for 24 h at room temperature. The final polymer layer thickness after this treatment was about 1 mm.

The glued joints were tensile tested at a fixed loading rate in a special laboratory lever device. The time to fracture varied from ≈10 to 10^3 s. Not less than five samples were tested at each fixed temperature, after which the results were averaged. The scatter of adhesion strengths measured at each fixed temperature did not exceed 5%.

The glass transition temperatures of glues and polyamides were determined by means of differential scanning calorimetry using a Perkin-Elmer DSC-2 calorimeter operating at a temperature scan rate of 10 K/min.

Results. Figure 1 shows the typical temperature dependences of the adhesion strength (fracture stress) for the joints of steel 45 with glue K-300 and polyamide 66/6. The curves observed for the joints with other glues and polyamides exhibited qualitatively the same behavior.

As can be seen from Fig. 1, the experimental curves, can be divided into two regions. In the first region, extending from room temperature up to the glass transition temperature T_g, the adhesion strength decreases

1063-7850/04/3010-0862$26.00 © 2004 MAIK "Nauka/Interperiodica"

linearly with increasing temperature. The second region, $T > T_g$, is characterized by a slope of the experimental curve gradually decreasing with an increase in the temperature. The values of T_g for various glues and polyamides are given in Tables 1 and 2.

Discussion of results. The temperature dependence of σ at $T < T_g$ was studied in detail previously [7]. It was established that the adhesion strength under the conditions of a constant loading rate can be described using Eq. (1) and the Baily criterion of damage addition [5, 6]:

$$\int_0^{t_f} \frac{dt}{\tau[\sigma(t), T]} = 1, \quad (2)$$

where t_f is the time to fracture. The latter condition can be approximately rewritten as

$$\sigma_f(T) \approx \frac{U_0}{\gamma} - \frac{k_B T}{\gamma} \ln \frac{\tau_{ef}}{\tau_0}, \quad (3)$$

where σ is the fracture stress and τ_{ef} is the time to fracture under a constant load, which is related to the time to fracture under a constant loading rate τ_{ef} as $\tau_{ef} \approx 0.1 t_f$.

According to formula (3), the adhesion strength has to be approximately a linear function of the temperature, in agreement with what is experimentally observed for temperatures not exceeding T_g (Fig. 1).

Above the glass transition temperature, polymers are known to occur in a rubberlike (high elasticity) state in which the prefracture deformation (elongation at break) increases up to several hundred percents and the γ value determined from fracture tests continuously decreases [8]. This is manifested by a decrease in the slope of the temperature dependence of σ observed in experiment.

The temperature dependence of the strength of a polymer in the rubberlike state is empirically described by the relation [9]

$$\tau = \tau_0 \left(\frac{\sigma(T_g)}{\sigma} \right)^m \exp \frac{U_0}{k_B T}, \quad (4)$$

where $\sigma(T_g)$ is the strength at the glass transition temperature and m is an empirical constant. There were attempts [5] to relate the parameter m to some other characteristics of a given polymer, such as elastic modulus, glass transition temperature, and the value of γ at $T < T_g$.

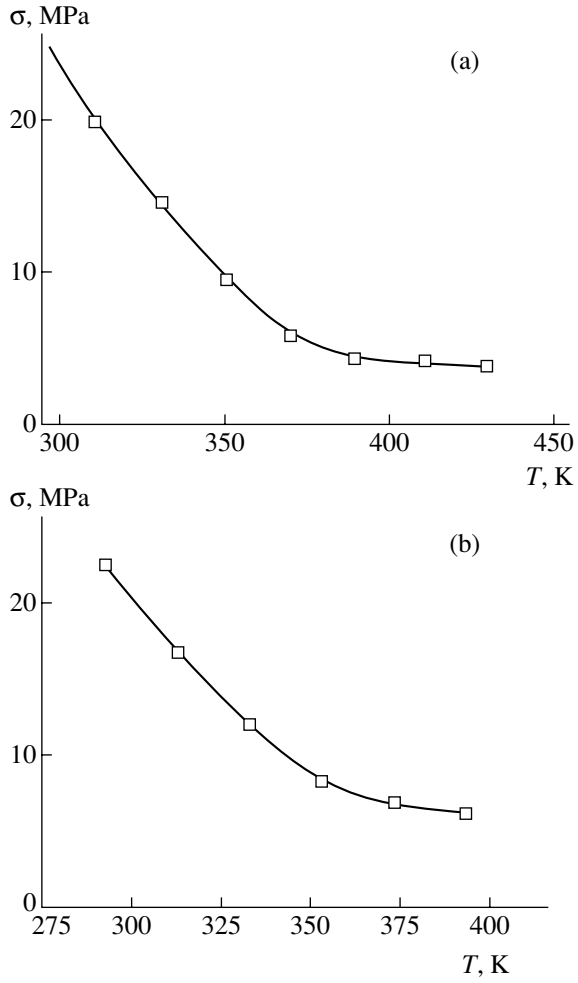

Fig. 1. Temperature dependences of the strength of adhesion of steel 45 with (a) epoxy-rubber glue K-300 and (b) polyamide 66/6 for the time to fracture $t_f \approx 10$ s.

We suggest that the parameter m is related to the activation energy of fracture, U_0, and the glass transition temperature by the formula

$$m = \frac{U_0}{3 k_B T_g}. \quad (5)$$

Substituting expression (5) into relation (4), we obtain

$$\ln\sigma \approx \ln\sigma(T_g) - \frac{3 k_B T_g}{U_0} \ln \frac{\tau_{ef}}{\tau_0} + 3\frac{T_g}{T} = A + 3\frac{T_g}{T}. \quad (6)$$

According to this equation, the logarithm of the

Table 1. The glass transition temperatures of epoxy-rubber glues

Glue		KDS-19	K-300	KVS-31
T_g, K	From DSC data	310	330	300
	From $\ln\sigma = f(1/T)$ relation	370	360	270

Table 2. The glass transition temperatures of polyamides

Glue		PA6	PA66	PA66/6
T_g, K	From DSC data	370	293	358
	From $\ln\sigma = f(1/T)$ relation	350	320	330

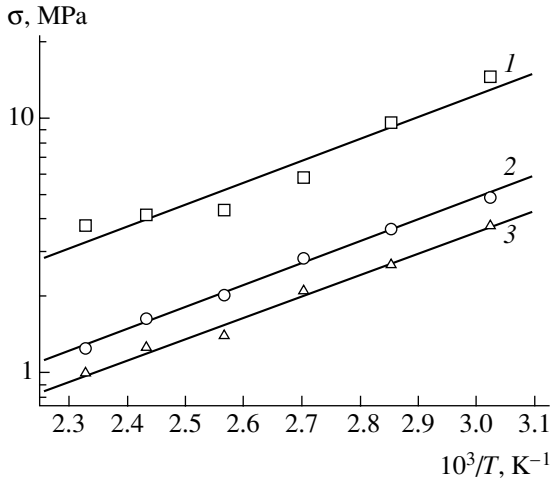

Fig. 2. Logarithmic plots of $\sigma = f(1/T)$ for the glued joints of steel 45 with epoxy-rubber glue K-300 for various times to fracture (s): (*1*) 10; (*2*) 10^2; (*3*) 10^3.

strength at a fixed time to fracture has to be proportional to the inverse temperature. The coefficient of proportionality (slope) of this dependence must be $3T_g$, independently of the time to fracture.

Figure 2 shows plots of the adhesion strength versus inverse temperature in a logarithmic scale for the glued joints of steel 45 with K-300 tested at $T \geq T_g$. As can be seen, the experimental points observed for various times to fracture fit well to straight lines with the same slope. For the other glued joints, the experimental points plotted as $\lg\sigma = f(1/T)$ also fit straight lines. By determining the slope of these plots, it was possible to determine T_g. As can be seen from Tables 1 and 2, the glass transition temperatures determined in this way are reasonably close to the values obtained from DSC measurements.

Therefore, the temperature dependence of the adhesion strength of epoxy-rubber glues and polyamides in the rubberlike state in the glued joints with steel 45 is described well by relation (6).

Acknowledgments. This study was supported by the Federal Targeted Program "Integration 2002–2006," project no. IO198/695.

REFERENCES

1. S. N. Zhurkov, Vestn. Akad. Nauk SSSR **11**, 78 (1957).
2. S. N. Zhurkov, Int. J. Fract. Mech. **1**, 311 (1965).
3. V. R. Regel', A. I. Slutsker, and E. E. Tomashevskiĭ, Usp. Fiz. Nauk **106** (2), 193 (1972) [Sov. Phys. Usp. **15**, 593 (1972)].
4. S. N. Zhurkov, Vestn. Akad. Nauk SSSR **3**, 46 (1968).
5. V. P. Regel', A. L. Slutsker, and É. E. Tomashevskiĭ, *Kinetic Nature of the Strength of Solids* (Nauka, Moscow, 1975) [in Russian].
6. V. A. Petrov, A. Ya. Bashkarev, and V. I. Vettegren', *Physical Basis for the Prediction of the Lifetime of Construction Materials* (Politekhnika, St. Petersburg, 1993) [in Russian].
7. V. I. Vettegren', A. Ya. Bashkarev, and V. A. Sytov, Pis'ma Zh. Tekh. Fiz. **30** (3), 31 (2004) [Tech. Phys. Lett. **30**, 99 (2004)].
8. V. A. Stepanov, N. N. Peschanskaya, and V. V. Shpeĭzman, *Strength and Relaxation Phenomena in Solids* (Nauka, Leningrad, 1984) [in Russian].
9. G. M. Bartenev, *Strength and Mechanisms of Fracture of Polymers* (Khimiya, Moscow, 1984) [in Russian].

Translated by P. Pozdeev

Technical Physics Letters, Vol. 30, No. 10, 2004, pp. 865–867. Translated from Pis'ma v Zhurnal Tekhnicheskoĭ Fiziki, Vol. 30, No. 20, 2004, pp. 50–55.

Direct Observation of the Photoinduced Evolution of the Plastic Properties of Glassy Semiconductors

M. L. Trunov

Uzhgorod National University, Uzhgorod, Ukraine

e-mail: stm@tn.uz.ua

Received May 5, 2004

Abstract—The evolution of the plastic properties of chalcogenide glassy semiconductor films continuously irradiated by light in the spectral region of intrinsic absorption has been studied. The photoinduced variation of plasticity (photoplastic effect) exhibits a two-stage character, whereby an intermediate metastable phase is formed in the first stage. The plasticity of this phase is higher than that of the light-stable phase formed upon prolonged irradiation. In both stages, the photoplastic effect was quantitatively characterized by viscosity measured using a microindentation technique. The most pronounced photoplastic effect is observed in freshly deposited $As_{50}Se_{50}$ films, the viscosity of which changes from ~1.5×10^{12} P in the initial stage (giant photosoftening) to ~6×10^{14} P in the final stage. © *2004 MAIK "Nauka/Interperiodica".*

Previously [1, 2], thin films of As–S(Se) chalcogenide glasses were found to exhibit a negative photoplastic effect, whereby the samples irradiated by light in the spectral region of intrinsic absorption passed from viscoelastic to plastic state (this structural transition is also called photosoftening). The macroscopic model of this phenomenon was based on the assumption that the viscosity of chalcogenide glasses drops under the action of light at room temperature from the initial level to 10^{12}–10^{13} P (which is close to the viscosity of such glasses near the glass transition temperature T_g). This assumption was confirmed by the behavior of viscosity evaluated from the kinetics of microindentation in the course of irradiation [2]. Analogous results were obtained for films of chalcogenide glasses of different compositions [3, 4] and for As_2S_3 glassy fibers exposed to a weakly absorbed light at an intensity of about 100 W/cm^2 with simultaneous application of tensile stresses [5]. The value of viscosity (5×10^{12} P) obtained in illuminated stressed glass under such conditions [5] agrees well with the results obtained previously [1, 2], which is evidence of the universal character of these phenomena and a common mechanism responsible for the observed behavior.

This Letter presents the results of investigation of the kinetics of a photoplastic effect in thin films of chalcogenide glasses of the As–Se system.

The experiments were performed with 1- to 3-μm-thick films obtained by thermal evaporation of As_xSe_{1-x} glasses from quasi-closed effusion cells and deposition at a rate of 2–5 nm/s onto unheated quartz glass substrates. The samples were exposed to radiation of a He–Ne laser operating at a wavelength of 633 nm. The radiation power density at the sample surface did not exceed 130 mW/cm^2. Irradiation at this intensity does not lead to heating of the film [6], and, hence, all the effects described below are of athermal (electronic) nature.

The mechanical properties of the deposited films were studied by the method of cyclic microindentation. The measurements were performed on a PMT-3 microhardness meter using a Vickers indenter (a tetrahedral diamond pyramid with a 136° angle between opposite faces) under a load of P = 0.02–0.05 N. During the experiment, several microindentations on the irradiated sample were made at the same indenter load. After each load–unload cycle, the sample was moved so that each subsequent cycle was performed in a new region of the film. The exposure was not suspended between the sequential indentations, and the time required for the sample translation (not exceeding 10 s) was added to the total exposure equal to the sum of all preceding load–unload cycles. In the first series of experiments, the exposure in each subsequent cycle was increased from 10 s to 2 h; in the second series, the exposure time was fixed at 20 s. The sum of the diameters of the indenter prints did not exceed 200 μm, which was much smaller than the laser spot size (2 mm) on the sample surface. The experiments were performed with five samples prepared in the same evaporation–deposition cycle. The sample diameter was 15 mm, which allowed repeated series of measurements to be performed so as to gain statistics providing for reliable and reproducible results.

Figure 1 (rows I–IV) shows the interferograms of indenter imprints obtained in the first series of experiments (at a load of P = 0.02 N) with freshly prepared (as-deposited) $As_{50}Se_{50}$ films. The measurements in these experiments were performed in the dark (row I),

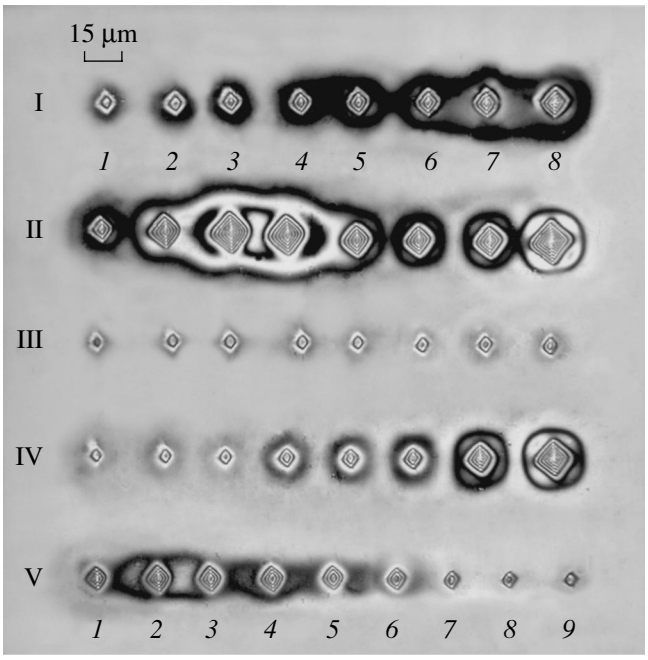

Fig. 1. Interferograms of sequential microindentations in a 3-μm-thick as-deposited $As_{50}Se_{50}$ film. The duration of every next load-unload cycle in rows I–IV increases with the number, amounting to 10 s (*1*), 30 s (*2*), 1 min (*3*), 3 min (*4*), 5 min (*5*), 10 min (*6*), 30 min (*7*), and 120 min (*8*). In row V, the time of each cycle is fixed (20 s) and the exposure increases with the number, amounting to 20 (*1*), 50 (*2*), 80 (*3*), 140 (*4*), 200 (*5*), 300 (*6*), 600 (*7*), and 1200 s (*8*); imprint *9* was obtained immediately after switching off the radiation source.

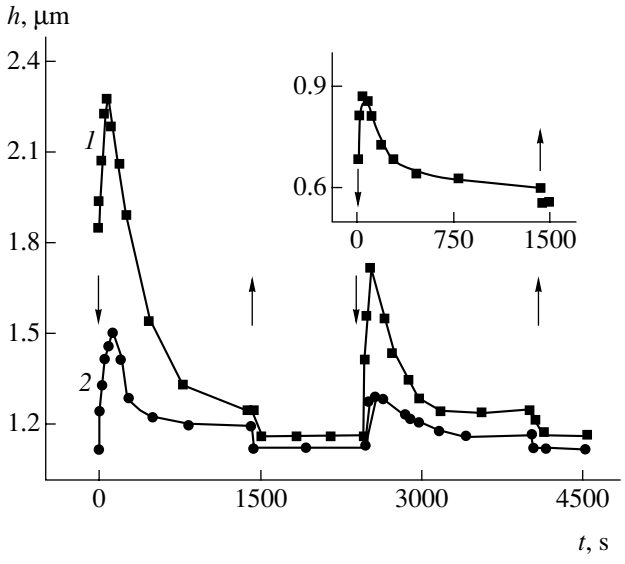

Fig. 2. Plots of the indenter penetration depth *h* versus exposure time *t* for as-deposited (*1*) $As_{50}Se_{50}$ and (*2*) $As_{40}Se_{60}$ films. The inset shows data for the $As_{50}Se_{50}$ film upon thermal annealing. All films were 3 μm thick; the time of loading at each point was Δt = 20 s. Arrows indicate the moments of radiation source switching on (↓) and off (↑).

during the first exposure (row II), after switching off the radiation source (row III), and during repeated exposure (row IV). In multiply repeated series of measurements with the laser switched on and off, the results are analogous to those presented in rows III and IV.

As can be seen from the experimental data, the depth of indenter penetration in the dark only very slightly increases with the time of indenter loading (Fig. 1, row I) in the sequence of microindentations on a freshly prepared film and is virtually independent of this time in the sequence of measurements performed in the dark after exposure of the film (Fig. 1, row III). The pattern is significantly different for the measurements in the course of irradiation, whereby the indenter penetration nonlinearly varies with the time: in the initial stage, the indenter print rapidly increases to reach a maximum size after a 120-s exposure; then, the penetration depth exhibits a decrease followed by new growth in proportion to the time of exposure (Fig. 1, row II). During the second exposure after holding in the dark, the depth of indenter penetration virtually linearly increases with time from the very beginning (Fig. 1, row IV). The interferograms of the indenter microprints measured using a Michelson microinterferometer showed that the initially brittle glass becomes soft and fluid under the action of light and stress. This is manifested by a significant increase in the indenter penetration depth and the appearance of fluidity zones appearing as a broad black-and-white contour along the perimeter. Such zones are typically observed during microindentation testing of plastic materials, such as metals.

It should be noted that certain plasticity is also inherent in the as-deposited films (Fig. 1, row I). However, the observed increase in the indenter penetration depth with the loading time is mostly related to a reduced initial density of packing in the film and the presence of a free volume (voids, pores, and other microdefects destroyed by high pressure at the indenter tip).

It was demonstrated previously [2] that the rate of the indenter penetration into chalcogenide glasses in the course of exposure is controlled by viscous flow in the material. For this reason, the observed nonmonotonic variation of the indenter print size during the first exposure (Fig. 1, row II) is indicative of the photoinduced variation of the glass viscosity. This is confirmed by the results of the second series of experiments, in which the films were subjected to microindentation at a fixed time (Δt = 20 s) of indenter loading (Fig. 1, row V). In this case, the kinetics of indenter penetration reflects variation of the viscosity of the irradiated glass time-averaged over Δt. Therefore, the observed behavior shows that the viscosity drops to a minimum level within the first 50 s of exposure, then gradually increases, and eventually ceases to change with the duration of exposure. The value of viscosity estimated using the method described in [2] amounted to ~1.5 ×

10^{12} P in the initial stage and ~6×10^{14} P in the final stage.

Figure 2 (curve *1*) shows quantitative data characterizing the entire process of microindentation in the second series of experiments with $P = 0.04$ N, including repeated cycles of exposure. As can be seen, the intermediate stage of increased plasticity is observed both during the first cycle of irradiation and in the course of repeated exposures. Similar behavior, although less pronounced, was also observed in experiments with As–Se films of other compositions, for example $As_{40}Se_{60}$ (Fig. 2, curve *2*), and with annealed $As_{50}Se_{50}$ films (see the inset in Fig. 2). Thus, the results of our experiments show that the process of microindentation in all cases has two stages. In the first stage (during the initial exposure), the film is characterized by a higher plasticity than in the second stage corresponding to prolonged irradiation.

According to the intramolecular model of photoinduced plasticity in chalcogenide glasses [7], the simultaneous action of light and applied stress leads to a transformation of molecules of the $As_4S_4(Se_4)$ type from closed (three-dimensional) to open (planar) configuration. Therefore, maximum changes in the photoplasticity of such glasses must be observed in films with maximum concentration of such molecules (i.e., in $As_{50}Se_{50}$ films), which is confirmed in experiment.

Acknowledgments. The author is grateful to V.S. Bilanich and A.A. Grabar for their help in conducting experiments.

REFERENCES

1. M. L. Trunov and A. G. Anchugin, Pis'ma Zh. Tekh. Fiz. **18** (1), 37 (1992) [Sov. Tech. Phys. Lett. **18**, 14 (1992)].
2. M. L. Trunov and A. G. Anchugin, Pis'ma Zh. Tekh. Fiz. **18** (5), 78 (1992) [Sov. Tech. Phys. Lett. **18**, 158 (1992)].
3. M. L. Trunov, A. G. Anchugin, N. D. Savchenko, *et al.*, Proc. SPIE **2113**, 186 (1994).
4. M. L. Trunov, J. Non-Cryst. Solids **192**–**193**, 431 (1995).
5. H. Hisakuni and K. Tanaka, Science **270**, 974 (1995).
6. A. Saliminia, T. Galstian, and A. Villeneuve, Phys. Rev. Lett. **85**, 4112 (2000).
7. S. N. Yannopoulos, Phys. Rev. B **68**, 064206 (2003).

Translated by P. Pozdeev

Technical Physics Letters, Vol. 30, No. 10, 2004, pp. 868–870. Translated from Pis'ma v Zhurnal Tekhnicheskoĭ Fiziki, Vol. 30, No. 20, 2004, pp. 56–62.

Cathode-Initiated Vacuum Breakdown in a Pulse Regime

A. A. Emel'yanov*, E. A. Emel'yanova, and T. N. Safonova

Orel State Technical University, Orel, Russia

** e-mail: emel@ostu.ru*

Received January 8, 2004; in final form, May 12, 2004

Abstract—Based on an analysis of the Joule heating of emitters by thermionic current, new methods and criteria are proposed for evaluating vacuum breakdown cathode-initiated in a pulse regime for an arbitrary cathode shape. The applicability of the proposed methods and validity of the new criteria are confirmed by the results of experiments using nanosecond pulses applied to coaxial copper electrodes with a gap width of $d = 0.2$ mm and an area of $S = 2500$ mm^2. © *2004 MAIK "Nauka/Interperiodica".*

The process of cathode-initiated breakdown in vacuum is related to emitter destruction by the current. In a stationary regime, vacuum breakdown is initiated when the microscopic electric field strength at a cathode reaches a certain critical value determined by the properties of the emitter material [1],

$$E = E_{cr}. \quad (1)$$

Criterion (1) is valid both in a regime of constant current and in the case of high-voltage pulses of sufficiently large duration ($t_p > 10^{-6}$ s). A decrease in the voltage pulse duration leads to an increase in the microscopic electric field strength, and, at $t_p \le 10^{-6}$ s, the criterion of breakdown initiation involves the current density j and the breakdown delay time t_d [2]:

$$j^2 t_d = \text{const}. \quad (2)$$

It was suggested [3] that breakdown in a pulse regime is initiated when the factors determining this process are accumulated to certain critical level, so that the criterion can be formulated as

$$\int_0^{t_d} f(U)dt = G, \quad (3)$$

where $f(U)$ is the rate of accumulation of the aforementioned control factors.

In the case of cathode-initiated breakdown, such a determining factor is the energy liberated in the emitter as a result of the current passage. The breakdown is initiated when this energy is equal to that required for emitter destruction by the current. As the amplitude of applied voltage pulses increases, the power supplied to the emitter grows and the breakdown delay time drops. For the cathode initiation, criterion (3) can be written as [4]

$$\int_0^{t_d} j^2 dt = \text{const}. \quad (4)$$

In practice, a criterion in this form is applicable only to the classical emitters of known geometry, for which the current density can be determined. In the case of cathodes with large working surfaces, the geometry of microemitters is unknown and criterion (4) is useless.

In order to develop new methods and criteria for evaluation of the conditions of cathode-initiated vacuum breakdown applicable to systems with electrodes of arbitrary shape, we have studied the effect of high-voltage conditioning of the cathode with pulses of a width equal to the breakdown delay time on the cathode surface quality and on the electric strength of insulation in a pulse mode.

From the standpoint of cathode-initiated breakdown in vacuum, the quality of the cathode surface is characterized by the coefficient β of the electric field strength amplification at microinhomogeneities of the cathode surface. Conditioning of the cathode by the application of voltage pulses with a duration equal the breakdown delay time ($t_p = t_d$) is the optimum regime, which favors the formation of a surface whose quality is determined by the power of conditioning pulses. The pulse power in the optimum regime is determined by the macroscopic field strength E_0 initiating the breakdown at the cathode. The coefficient β characterizing the cathode surface quality obtained as a result of conditioning in a regime with $t_p = t_d$ is a function of the critical field strength [5],

$$\beta = \left(\frac{E_{cr}}{E_0}\right)^{0.9}\Bigg|_{t_p = t_d}, \quad (5)$$

where $E_{cr} = 1.32 \times 10^{10}$ V/m is the critical field strength. Conditioning in this regime ensures the formation of the ideal cathode surface characterized by the amplification coefficient $\beta = 1$, for which the field strength at the tip (E) and base (E_0) of a microinhomogeneity (protrusion) are equal: $E = E_0 = E_{cr}$.

Using condition (5), we can relate relative changes of the parameter β and the electric E_0 in the pulse mode achieved by conditioning in the regime with $t_p = t_d$. This will provide a new form of the criterion of cathode-initiated breakdown applicable to electrodes with a developed working surface of arbitrary geometry.

The cathode surface conditioned by pulses of various durations, $t_{p1} = t_{d1}$ and $t_{p2} = t_{d2}$, is characterized by different amplification coefficients in the established regime: β_1 and β_2. The cathode-initiated breakdown at the surfaces with different coefficients β_1 and β_2 will also possess different electric field strengths (E_{01} and E_{02}) and pulsed breakdown voltages (U_1 and U_2).

Introducing quantities characterizing the relative change in the surface quality,

$$K_\beta = \frac{\beta_1}{\beta_2}, \tag{6}$$

and the electric strength,

$$K_U = \frac{U_2}{U_1}, \tag{7}$$

and using relation (5), we obtain a criterion of the cathode-initiated breakdown for a cathode conditioned by pulses with $t_p = t_d$:

$$\left.\frac{K_\beta}{K_U^{0.9}}\right|_{t_p = t_d} = 1. \tag{8}$$

Thus, relation (8) is a new form of the criterion of cathode-initiated breakdown in a pulse regime. This condition establishes a relation between relative changes of the cathode surface quality and the electric field strength in the pulse mode upon conditioning in the optimum regimes with $t_{p1} = t_{d1}$ and $t_{p2} = t_{d2}$.

Small changes of the cathode surface correspond to weak variations of the parameter β. In this case, a final value of β_2 achieved as a result of conditioning in the regime with $t_{p2} = t_{d2}$ can be represented as a sum of the initial value β_1 and a small increment $\Delta\beta$,

$$\beta_2 = \beta_1 + \Delta\beta. \tag{9}$$

By the same token, for cathode-initiated breakdown, weak variations of the parameter correspond to small changes in the electric strength and the breakdown voltage,

$$U_2 = U_1 + \Delta U. \tag{10}$$

With neglect of the second-order terms, criterion (8) can be written in an alternative form as

$$\frac{\Delta\beta}{\beta_1} = -0.9\left.\frac{\Delta U}{U_1}\right|_{t_p = t_d}, \tag{11}$$

according to which a relative decrease in the coefficient β ($\Delta\beta < 0$) corresponds to a certain relative increase in the breakdown voltage ($\Delta U > 0$), while a relative decrease in the cathode surface quality ($\Delta\beta > 0$) corresponds to a relative decrease in the electric strength ($\Delta U < 0$).

The proposed criteria (8) and (11) were experimentally verified using coaxial copper electrodes with a gap width of $d = 0.2$ mm and an area of $S = 2500$ mm^2 at a residual pressure of $P \approx 10^{-5}$ Pa. The breakdown was initiated by high-voltage pulses with $t_{p1} = 200$ ns and $t_{p2} = 50$ ns. Prior to the conditioning in each pulse regime, we measured a dc current–voltage characteristic, plotted it in Fowler–Nordheim coordinates, and determined the field amplification coefficient β from the slope of this plot. After accomplishing the dc measurements and determining the β value, we studied the cathode-initiated breakdown conditions by applying pulses and gradually increasing their amplitude until the first breakdown took place at a minimum overvoltage. Prior to these measurements, the cathode was conditioned by pulses $t_p \approx t_d$ until reaching established values of the amplification coefficient and the electric strength in the pulse mode.

Plots of the field amplification coefficient β and the related voltage U for the first pulse-induced breakdown in the established regime versus the number of pulses with durations $t_{p1} = 200$ ns and $t_{p2} = 50$ ns are presented in the figure. A comparison of the behavior of $\beta(n)$ and $U(n)$ for $t_p = \text{const}$ confirms that the state of the surface is correlated with the electric strength. A decrease in the surface quality (manifested by increasing β) leads to a reduction of the electric strength (a decrease in U), while improved surface quality (decreasing β) increases the electric strength (as manifested by an increase in U). This correlation of U and β confirms that processes on the cathode surface are responsible for the pulse–induced breakdown.

Upon conditioning in the optimum regime using pulses with $t_{p1} = 200$ ns, the average values of the field amplification coefficient and the pulse-induced breakdown voltage were $\bar{\beta}_1 = 107$ and $\bar{U}_1 = 24.6$ kV, respectively, with a relative scatter of $\sigma_{\beta 1}/\bar{\beta}_1 = 0.46$ and $\sigma_{U1}/\bar{U}_1 = 0.27$. The process of optimum conditioning

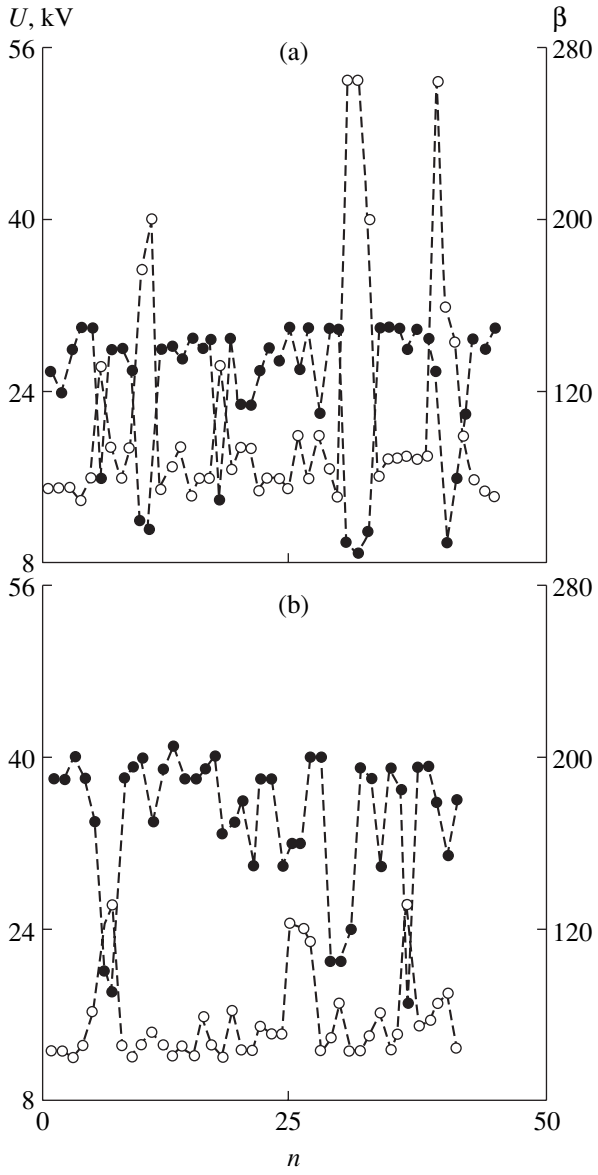

Plots of the field amplification coefficient β (open circles) and the related voltage U for the first pulse-induced breakdown (black circles) in the established regime with $t_p = t_d$ versus the number of pulses with durations (a) $t_{p1} = 200$ ns and (b) $t_{p2} = 50$ ns.

with $t_{p2} = 50$ ns increased the surface quality to $\bar{\beta}_2 = 77$ and the electric strength to $\bar{U}_2 = 34$ kV at a reduced relative scatter, $\sigma_{\beta 2}/\beta_2 = 0.3$ and $\sigma_{U2}/\bar{U}_2 = 0.19$.

Using the criterion of the pulse-induced breakdown in form (8) relating changes in the surface quality K_β and the electric strength K_U in the pulse mode, we can ascertain that cathode-initiated breakdown is responsible for deterioration of the electric strength of insulation with respect to a pulsed voltage with $t_{p1} = 200$ ns and $t_{p2} = 50$ ns. The error of evaluation was ~3%. Indeed, a fourfold change in the pulse duration on the passage from $t_{p1} = 200$ ns and $t_{p2} = 50$ ns leads to ~40% variations in the surface quality and the electric strength. The relative scatter in β and U values also changes by ~40%. The same criterion in form (11) confirmed the role of the cathode-initiated breakdown mechanism for the pulses with $t_{p1} = 200$ ns and $t_{p2} = 50$ ns, but with a relative error of ~11%.

In conclusion, we have proposed new methods and criteria for evaluating cathode-initiated breakdown in vacuum in a pulse regime, which are confirmed by the results of experiments with electrodes possessing a developed working surface. The proposed approach can be used for evaluation of the mechanism of breakdown initiation in vacuum gaps with an arbitrary geometry of electrodes.

REFERENCES

1. D. Alpert, D. A. Lee, F. M. Lyman, *et al.*, J. Vac. Sci. Tech. **1**, 35 (1964).
2. G. K. Kartsev, G. A. Mesyats, D. I. Proskurovskiĭ, *et al.*, Dokl. Akad. Nauk SSSR **129**, 309 (1970).
3. N. F. Olendzskaya and M. A. Sal'man, Zh. Tekh. Fiz. **40**, 333 (1970) [Sov. Phys. Tech. Phys. **15**, 242 (1970)].
4. A. A. Emel'yanov and G. M. Kassirov, Izv. Vyssh. Uchebn. Zaved., Fiz., No. 9, 105 (1976).
5. A. A. Emel'yanov, Prib. Tekh. Éksp., No. 5, 68 (1997).

Translated by P. Pozdeev

Technical Physics Letters, Vol. 30, No. 10, 2004, pp. 871–873. Translated from Pis'ma v Zhurnal Tekhnicheskoĭ Fiziki, Vol. 30, No. 20, 2004, pp. 63–69.

Sliding Electric Arc Discharge as a Means of Aircraft Trajectory Control

V. S. Aksenov, V. V. Golub*, S. A. Gubin, V. P. Efremov, I. V. Maklashova, A. I. Kharitonov†, and Yu. L. Sharov

Institute for High Energy Densities, Associated Institute for High Temperatures, Russian Academy of Sciences, Moscow, Russia

** e-mail: golub@ihed.ras.ru*

Received May 6, 2004

Abstract—The dynamics of sliding electric arc discharge and the formation of shock waves in the stages of leader motion and the electric arc development in a supersonic air flow behind the shock wave have been studied for an initial pressure of 0.09–0.5 atm (bar). The air flow in the discharge was imaged using an optical system comprising a shadow device (IAB-458), an optical interference attachment (RP-452), and a modified ruby laser (OGM-20) producing 10–15 output pulses per pumping pulse. Stable initiation of sliding electric arc discharge takes place in a supersonic air flow behind the shock waves with $1.7 < M < 3.4$. This discharge produces shock waves leading to separation of the boundary layer and to an increase in the pressure at the surface. These shock waves can be used for modifying gasdynamics in the air flow streamlining the surface and for controlling the motion of an aircraft. © *2004 MAIK "Nauka/Interperiodica".*

Sliding electric arc discharge moves from one electrode to another along a semiconductor surface and is terminated upon discharge of a capacitive bank with the formation of a high-power electric arc generating a shock wave in the surrounding space [1, 2]. This type of discharge is used in various electrophysical devices, for example, in effective light sources [1–3]. However, a sliding electric arc discharge can be also used as a means of controlling the trajectory of an aircraft [4–6]. A high-power shockwave generated by sliding electric arc discharge at the aircraft surface modifies the character of streamlining of the surface by air flow, which gives rise to a force that can be used to control the aircraft trajectory.

The length of the sliding electric arc (equal to the interelectrode gap width) may vary from a few millimeters to several meters [7]. The material at the surface of which the discharge is generated may be carbon, carbon-containing ceramics, and some other semiconductors. The results of determination of the leader velocity v at a field strength in the range E = 40–225 kV/m for rods of various lengths made of different materials are satisfactorily approximated by a linear relation $\log v = 2.6951 \log E - 10.066$ (where $[v]$ = m/s and $[E]$ = V/m). Assuming that the leader velocity corresponds to that of the ideal one-dimensional shock wave in air, the excess pressure at the leader front can be also described by a linear relation: $\log(\Delta P) = 4.55 \log E - 20.44$ (where $[\Delta P]$ = atm and $[E]$ = V/m).

† Deceased.

The question of primary importance is whether stable initiation of sliding electric arc discharge is possible in a supersonic air flow under the conditions modeling the aircraft flight at a supersonic velocity. There were experiments with high-velocity plasma jets obtained using electric arc discharge in gases and with discharge plasma interacting with supersonic gas jets [8]. However, to the best of our knowledge, no data are available on the initiation of sliding electric arc discharge in a supersonic gas flow.

This study was devoted to modeling the initiation of sliding electric arc discharge on the surface of aircraft by exciting discharge in a supersonic gas flow behind the shock wave front in a shock tube at a reduced gas pressure.

The experiments were performed in a diaphragm shock tube with a 72×72 mm square cross section. The lengths of the high- and low-pressure chambers were 1.25 and 6.7 m, respectively. The discharge gap was situated in the lower part of the tube, in the middle of a transparent section with a 110×69 mm viewport. The driving gas was air or helium. The low-pressure chamber was filled with air at an initial pressure of 0.09–0.5 atm for shock waves with the Mach numbers within $1.7 < M < 3.39$.

The discharge was initiated by the breakdown of spark gaps between electrodes and the surface of a semiconductor carbon–graphite composite rod with a 2×4 mm cross section and a length of 68 mm flush-mounted on the plate surface. The interelectrode distance was 60 mm. A storage bank with a capacitance of 50 μF was charged to a voltage of 3.1 kV.

1063-7850/04/3010-0871$26.00 © 2004 MAIK "Nauka/Interperiodica"

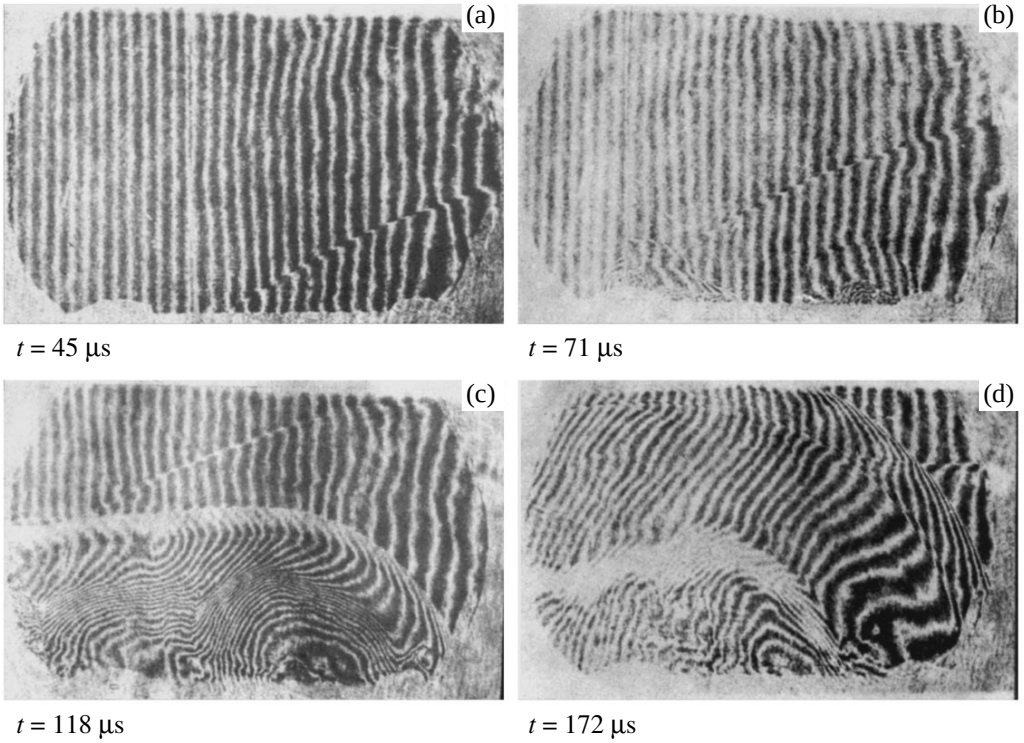

Fig. 1. A sequence of interference images illustrating the development of sliding electric arc discharge in air flow behind the shock wave front (M = 1.91, experiment 1).

The interaction of the electric arc discharge with the shock wave was imaged by the shadow and interference techniques using a system comprising an IAB-458 shadow device, an RP-452 optical interference attachment, and an SFR high-speed camera. The light source was a modified OGM-20 ruby laser producing 10–15 output pulses (with a duration of 50–70 ns) per 800-J pulse of a pumping lamp. A passive liquid gate (saturation filter [9]) was filled with a low-concentration solution of vanadyl phthalocyanine in toluene.

The time series of the images of sliding electric arc discharge in resting air reveal a high symmetry of the shock wave, which exhibits a cylindrical shape with spherical edges. Figures 1 and 2 illustrate the development of sliding discharge behind the front of a shock wave formed in air at an initial pressure of 0.33 and 0.09 atm and a flow velocity of 394 and 876 m/s, respectively. The first image (Fig. 1a) shows the shock wave front moving along the shock tube. The sliding discharge excited between the moments of time corresponding to Figs. 1a and 1b has the form of leaders (plasma formations) propagating from electrodes toward the center, with attached shock waves appearing at the heads of these leaders. Probably, even these relatively weak shock waves are capable of producing the breakage and separation of the boundary layer in a high-velocity air flow. The second image (Fig. 1b) shows two leaders having traveled 22 mm toward each other, with the corresponding compression waves 15 mm away from each leader head. Evidently, the

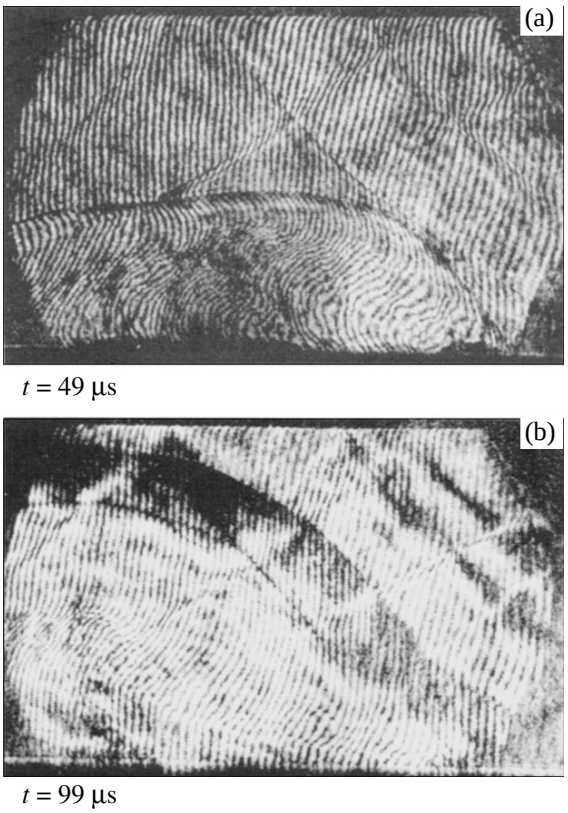

Fig. 2. Sequential interference images illustrating the development of sliding electric arc discharge in air flow behind the shock wave front (M = 3.39, experiment 2).

velocity of a leader moving in the direction opposite to the air flow (right to left in Fig. 1) differs only slightly from the velocity of another leader moving with the air flow from the opposite electrode, since the two leaders meet at the center of the discharge gap. Therefore, the high-velocity air flow under these conditions does not significantly influence the time to closure of the discharge gap. The third image (Fig. 1c) illustrates the gap closure by a plasma column with the formation of a high-power shock wave. This image reveals the shock wave outgoing from the electric arc discharge closed upon the meeting of leaders and the region of gas heated to a high temperature. As can be seen in Fig. 1c, the distance traveled by the shock wave front in the direction opposite to the flow is about half that in the transverse direction. This image also reveals a shadow pattern due to the boundary between the regions of cold air and that heated by the discharge, the latter being blown away by the flow. The fourth image (Fig. 1d) shows how the discharge-initiated shock wave is reflected from the upper wall and the region of hot air is moved leftward.

Figure 2 illustrates the behavior of a sliding electric arc discharge behind the front of a high-power shock wave formed in a supersonic air flow. The first image (Fig. 2a) reveals a shock wave formed due to the electric arc closure. Here, the shock wave (usually symmetric) is distorted by the oncoming flow. As can be seen in the second image (Fig. 2b), the stopped shock wave does not move along the flow and propagates only in the transverse direction.

The results of our experiments show that the shock wave formed due to the electric arc closure possesses sufficient intensity and spatial dimensions to provide for the breakage and separation of a boundary layer at the streamlined surface. Separation of the boundary layer gives rise to a force acting on the surface at this site. This force can be used as a control factor capable of modifying the total force acting upon the surface streamlined by a high-velocity air flow.

Sliding electric arc discharge can be readily formed on any surface and controlled so as to operate at a required frequency. The formation of periodic shock waves due to such a discharge initiated at a certain frequency at the aircraft surface will produce periodic breakage and separation of a boundary layer, with the corresponding modification of the gasdynamic parameters of air streamlining this surface and the development of a controlled periodic force acting on the aircraft surface.

In conclusion, our investigation of the process of sliding electric arc discharge in air flow behind the shock wave lead to the following conclusions.

(i) A plasma contact (leader) moving at an approximately constant supersonic velocity gives rise to an attached shock wave and, after electric arc closure, to a more powerful shock wave.

(ii) Stable initiation of sliding electric arc discharge behind the shock wave front in a supersonic air flow with $1.7 < M < 3.4$ is provided at an initial discharge voltage of 2.6–3.35 kV, with the formation of a high-power shock wave upon closure of the interelectrode gap by a plasma column.

(iii) Shock waves generated in air by sliding electric arc discharge at an aircraft surface can probably be used for controlled modification of the gasdynamic parameters of air streamlining this surface and, hence, for control of the aircraft motion.

Acknowledgments. This study was supported in part by the Presidium of the Russian Academy of Sciences, project no. 20-2003.

REFERENCES

1. E. A. Zobov, V. G. Sokolov, A. N. Sidorov, *et al.*, Prikl. Mekh. Tekh. Fiz., No. 2, 19 (1980).
2. É. A. Fazizov, N. A. Akhmerov, G. G. Gladush, *et al.*, Teplofiz. Vys. Temp. **22**, 655 (1984).
3. *High Speed Physics*, Ed. by K. Vollrath and G. Thomer (Springer, Vienna, 1967), Vol. 1.
4. V. S. Aksenov, S. A. Gubin, and V. P. Efremov, in *Proceedings of the 18th International Conference "The Physics of Matter in High-Energy-Stressed States" (Chernogolovka, 2003)*, Ed. by V. E. Fortov (Inst. Probl. Khim. Fiz. RAN, Chernogolovka, 2003), p. 103.
5. V. S. Aksenov, S. A. Gubin, V. V. Golub, *et al.*, in *Proceedings of the 5th Workshop on Magnetoplasma Aerodynamics for Aerospace Applications, 2003.*
6. V. S. Aksenov, V. V. Golub, S. A. Gubin, *et al.*, in *Proceedings of the Scientific Coordination Symposium "Problems in the Physics of Ultrashort Processes in Highly Nonequilibrium Media,"* Ed. by V. P. Efremov, G. E. Norman, *et al.* (Inst. Probl. Khim. Fiz. RAN, Chernogolovka, 2003), p. 25.
7. É. M. Bazelyan and Yu. P. Raĭzer, *Spark Discharge* (Mosk. Fiz. Tekh. Inst., Moscow, 1997) [in Russian].
8. S. A. Losev, *Gasdynamic Lasers* (Nauka, Moscow, 1977) [in Russian].
9. *Quantum Electronics*, Ed. by S. A. Akhmanov, M. E. Zhabotinskiĭ, *et al.* (Sov. Éntsiklopediya, Moscow, 1989) [in Russian].

Translated by P. Pozdeev

Technical Physics Letters, Vol. 30, No. 10, 2004, pp. 874–876. Translated from Pis'ma v Zhurnal Tekhnicheskoĭ Fiziki, Vol. 30, No. 20, 2004, pp. 70–76.

Nontrivial Behavior of the Piezoelectric Coefficients of 0–3 Composites of the Modified $PbTiO_3$ Ceramics–Polymer Type

S. V. Glushanin, V. Yu. Topolov*, and A. V. Krivoruchko

Rostov State University, Rostov-on-Don, Russia

** e-mail: topolov@phys.rsu.ru*

Received May 16, 2004

Abstract—Piezoelectric properties of the 0–3 connectivity composites comprising spheroidal inclusions of modified $PbTiO_3$ ceramics dispersed in a polymer matrix have been studied. Monotonic and nonmonotonic concentration dependences of the effective piezoelectric coefficients e_{3j}^*, d_{3j}^*, g_{3j}^*, and h_{3j}^* (j = 1, 3) of the composites with elongated ferroelectric ceramic (FC) inclusions are analyzed. The observed nontrivial piezoelectric response of the 0–3 composites of the modified $PbTiO_3$ ceramics–polymer type is determined to a considerable extent by properties of the polymer matrix and by the sign of the $e_{3j}^{(FC)}$ coefficients ($e_{3j}^{(FC)} > 0$). © *2004 MAIK "Nauka/Interperiodica".*

Composites of the 0–3 connectivity type comprising ferroelectric ceramic (FC) inclusions in an extended polymer matrix exhibit a variety of useful physical properties [1–4] and are widely used in modern piezoelectric technology, acoustics, and some other fields. Materials of this connectivity type show a significant dependence of their effective electromechanical properties, piezoelectric responsivity, and sensitivity of composites on the shape and mutual arrangement of FC inclusions [5–8]. In predicting the effective properties of the 0–3 composites of the FC ceramics–polymer type, FC components are typically represented by perovskitelike ceramics based on $BaTiO_3$ (BTO) and $Pb(Zr_{1-x}Ti_x)O_3$ (PZT) [3, 6, 8]. The piezoelectric coefficients $e_{3j}^{(FC)}$ of these ceramics have the following signs:

$$\mathrm{sgn}\, e_{33}^{(FC)} = -\mathrm{sgn}\, e_{31}^{(FC)} > 0. \quad (1)$$

Of special interest are the FCs based on modified $PbTiO_3$ ceramics characterized by a large anisotropy of the piezoelectric coefficients $d_{3j}^{(FC)}$ and by the same signs of $e_{3j}^{(FC)}$ values, with the $e_{33}^{(FC)}/e_{31}^{(FC)}$ ratio variable within wide limits. The group of such materials obeying the condition

$$\mathrm{sgn}\, e_{33}^{(FC)} = \mathrm{sgn}\, e_{31}^{(FC)} > 0 \quad (2)$$

includes, in particular, the FCs based on $(Pb_{0.9625}La_{0.025})(Ti_{0.99}Mn_{0.01})O_3$ (FC I; $e_{33}^{(FC)}/e_{31}^{(FC)}$ = 14.2) [9], $(Pb_{0.9625}La_{0.025})(Ti_{0.99}Mn_{0.01})O_3$ (FC II; 5.15) [10], $(Pb_{0.85}Nd_{0.10})(Ti_{0.99}Mn_{0.01})O_3$ (FC III, 4.91) [10], $(Pb_{0.855}Nd_{0.11})(Ti_{0.94}Mn_{0.02}In_{0.04})O_3$ (FC IV, 4.41) [10], and PZ34 (FC V, 1.80) [5], for which the entire sets of room-temperature elastic, piezoelectric, and dielectric coefficients are available.[1]

The aim of this study was to analyze, within the framework of the model of 0–3 connectivity composites with spheroidal inclusions, the influence of the FC component (modified $PbTiO_3$ ceramics) on the effective piezoelectric coefficients e_{3j}^*, d_{3j}^*, g_{3j}^*, and h_{3j}^* (j = 1, 3).

The piezoelectric composites under consideration, comprising FC inclusions dispersed in a polymer matrix, possess a cellular structure. According to the adopted model, it is assumed that all inclusions possess the same size and the spherical shape described by the equation $(x_1/a_1)^2 + (x_2/a_1)^2 + (x_3/a_3)^2 = 1$ in a Cartesian coordinate system $X_1X_2X_3$, with the residual polarization vector in each inclusion being directed along the OX_3 axis. The composite under consideration is described by the limiting symmetry group ∞mm. The volume fraction of the FC component, $m = V_{FC}/V_{cell}$ is defined as a fraction of the Banno unit cell V_{cell} occupied by a spheroidal inclusion with the volume V_{FC}. The effective electromechanical coefficients x_{ab}^* of the 0–3 connectivity composite are determined by the effective field method [6, 11], taking into account the electromechanical interactions between FC inclusions with the ratio of semiaxes $\rho = a_1/a_3$ varied in a broad

[1] A comparison of the electromechanical coefficients of FC I and FC II shows that their $e_{ij}^{(FC)}$ values significantly depend on the conditions of synthesis and polarization of the samples.

1063-7850/04/3010-0874$26.00 © 2004 MAIK "Nauka/Interperiodica"

range and the volume ratio m varied within [0.01; 0.50]. For comparison, note that, for a spherical inclusion ($\rho = 1$) in a cubic cell with the side length b_0, the radius of the inclusion may vary within $0 < r < b_0/2$ and the volume ratio within $0 < V_{FC}/V_{cell} < \pi/6$. It is also assumed that the resistivities of the FC ($\gamma^{(FC)}$) and polymeric (γ) components are related as $\gamma \geq \gamma^{(FC)}$, which favors better polarization of the composite. The values of x^*_{ab} have been calculated using experimental data on the electromechanical coefficients of FCs I–V and the following piezopassive polymers: araldite [5, 12], poly(urethane) (PU) [12], poly(ethylene) (PE) [5], and epoxy resin (ER) [5]. Some examples of the typical behavior of effective parameters of the 0–3 connectivity composites based on modified $PbTiO_3$ ceramics are presented in Figs. 1 and 2.

Characteristic features of the composites under consideration are the appearance of $\min d^*_{31}$, which has been observed for the first time (curve *1* in Fig. 1; curves *3* in Figs. 2a and 2b), and the "correlated" appearance of $\min g^*_{31}$ and $\max g^*_{33}$ (curves *2* and *3* in Fig. 1; curves *5* and *6* in Figs. 2a and 2b) for $0 < \rho < \rho^*$. It was established that ρ^* falls within 0.11–0.16 for various combinations of FCs and polymeric components; for the same FCs, ρ^* grows by 0.01–0.02 with increasing rigidity of the polymer matrix. The curve of $m_3(\rho)$ is not shown in Fig. 1 because the values of m_f satisfying the conditions $g^*_{31}(m_2, \rho) = g^*_{31, m}$ and $g^*_{33}(m_3, \rho) = g^*_{33, m}$ coincide to within 0.01. The calculated dependences of $e^*_{33}(m, \rho)$, $d^*_{33}(m, \rho)$, and $g^*_{33}(m, \rho)$ (see curves *2* and *4–6* in Figs. 2a–2c) are analogous to those reported previously [6, 8, 15] for the 0–3 composites based on FCs satisfying condition (1). The values of $g^*_{33, m}$ for $\rho \ll 1$ strongly depend on the rigidity of the polymer matrix surrounding the FC inclusions. For example the FC II–araldite composite with $\rho = 0.01$ has $g^*_{33, m}/g^{(FC)}_{33} = 9.13$, while the FC II–PE composite with the same ρ has $g^*_{33, m}/g^{(FC)}_{33} = 24.6$; the elastic moduli c_{11} and (c_{12} of these polymers differ by a factor of 2.3 and 1.5, respectively, and their permittivities ε_{pp} differ by a factor of 1.6.

It should be pointed out that, for $0 < \rho < \rho^*$, the 0–3 composites under consideration exhibit a large anisotropy: $e^*_{33}/e^*_{31} = h^*_{33}/h^*_{31} \gg 1$ for $\operatorname{sgn} e^*_{31} = \operatorname{sgn} h^*_{31} > 0$ and $d^*_{33}/|d^*_{31}| = g^*_{33}/|g^*_{31}| \approx 3$–5. These features in the behavior of $x^*_{3j}(m, \rho)$ are indicative of a significant influence of the polymer matrix on the piezoelectric properties of 0–3 composites with strongly elongated FC inclusions. This influence is clearly pronounced in the behavior of $d^*_{31}(m, \rho)|_{\rho \ll 1}$ (see curves *3* in Figs. 2a and 2b). The relation $d^*_{31} = e^*_{31}(s^{*E}_{11} + s^{*E}_{12}) + e^*_{33}s^{*E}_{13} < 0$ implies that $e^*_{3j} > 0$ and that the elastic compliances s^{*E}_{lj} are related as $e^*_{33}/e^*_{31} > -(s^{*E}_{11} + s^{*E}_{12})/s^{*E}_{13} < 0$, so that $e^*_{33}/e^*_{31} > c^{*E}_{33}/c^{*E}_{13}$ (c^{*E}_{ij} are the elastic moduli of the composite).

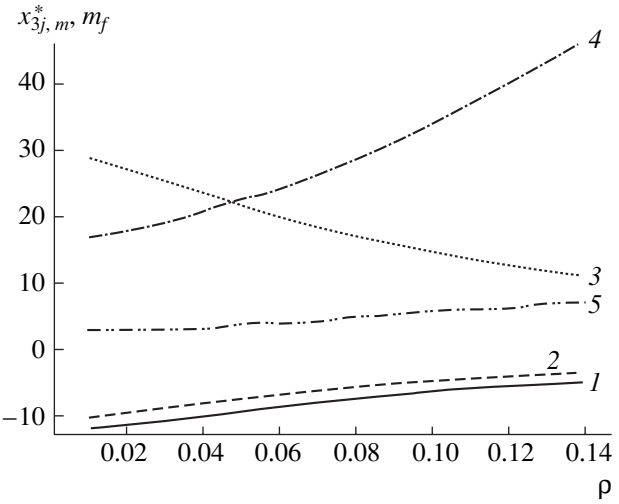

Fig. 1. Calculated values of (*1–3*) the local extrema of the effective piezoelectric coefficients $x^*_{3j, m}$ and (*4, 5*) the corresponding volume fractions m_f of spheroidal inclusions in 0–3 composites of the FC II–araldite type: (*1*) $d^*_{31, m} = \min d^*_{31}(m, \rho)|_{\rho = \text{ const}}$ [pC/N]; (*2*) $10^{-1} g^*_{31, m} = 10^{-1} \min g^*_{31}(m, \rho)|_{\rho = \text{ const}}$ [mV m/N]; (*3*) $10^{-1} g^*_{33, m} = 10^{-1} \max g^*_{33}(m, \rho)|_{\rho = \text{ const}}$ [mV m/N]; (*4*) m_1 [%]; (*5*) m_2 [%]. The m_f values were determined from the relations $d^*_{31}(m_1, \rho) = d^*_{31, m}$ and $g^*_{31}(m, \rho) = g^*_{31, m}$.

Both an increase in the volume fraction m of the FC inclusions and the "thickening" of spheroids with increasing ρ lead to a significant decrease in the e^*_{33}/e^*_{31} ratio at a small variation in c^{*E}_{33}/c^{*E}_{13}, which influences the shape of the $d^*_{31}(m, \rho)|_{\rho = \text{ const}}$ curve (cf. curves *3* in Figs. 2a and 2c). The passage from strongly elongated spheroids to spherical inclusions and the corresponding changes in the boundary conditions for the electric and mechanical fields lead to a decrease both in piezoelectric coefficients $|x^*_{3j}|$ of all four types at $m = \text{const}$ (cf. Figs. 2a and 2c) and in the anisotropy factor e^*_{33}/e^*_{31}. For this reason, the interval of $0 < \rho < \rho^*$ is of considerable interest for practical applications (Fig. 2a and 2b). In this interval. The ratio $d^*_{33}(m, \rho)/d^{(FC)}_{33}$ for various m (see curves *1–4* in Fig. 2d) is close to the experimental values of $d^*_{33}/d^{(FC)}_{33}$ [13, 14] of the 0–3 composites with two piezoelectrically active components (see curves *5* and *6* in Fig. 2d). In addition, composites of the FC II–piezopassive polymer type exhibit rela-

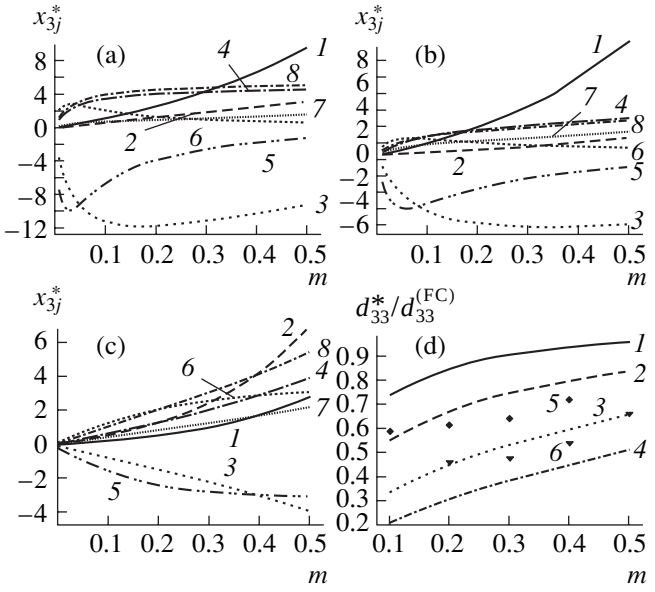

Fig. 2. (a–c) Calculated effective piezoelectric coefficients $e_{3j}^*(m, \rho)$ [C/m^2], $d_{3j}^*(m, \rho)$ [pC/N], $g_{3j}^*(m, \rho)$ [mV m/N], and $h_{3j}^*(m, \rho)$ [10^8 V m] of the 0–3 type FC II–araldite composite with $\rho = 0.01$ (a), 0.10 (b), and 1 (c): (*1*) $10^2 e_{31}^*$ (a–c); (*2*) e_{33}^* (a, b) and $10^2 e_{33}^*$ (c); (*3*) d_{31}^* (a, b) and $10\,d_{31}^*$ (c); (*4*) $10^{-1} d_{33}^*$ (a, b) and d_{33}^* (c); (*5*) $10^{-1} g_{31}^*$ (a, b) and g_{31}^* (c); (*6*) $10^{-2} g_{33}^*$ (a, b) and $10^{-1} g_{33}^*$ (c); (*7*) h_{31}^* (a–c); (*8*) $10^{-1} h_{33}^*$ (a, b) and h_{33}^* (c). (d) The ratio $d_{33}^*(m, \rho)/d_{33}^{(FC)}$ of the 0–3 type composites: (*1–4*) FC II–araldite composite with $\rho = 0.01$, 0.05, 0.10, and 0.15, respectively (calculated in this study); (*5*) $PbTiO_3$ ceramics–70/30 mol % vinylidene fluoride–trifluoroethylene copolymer, experiment [13]; (*6*) (Pb,Ca)TiO_3 ceramics–75/25 mol % vinylidene fluoride–trifluoroethylene copolymer, experiment [14].

tively high values of the hydrostatic piezoelectric modulus $g_h^* = g_{33}^* + 2g_{31}^*$. For example, the value of $g_h^*(m, \rho)$ decreases in the range $0.01 \le \rho \le 0.10$ from 90.3 to 52.6 (mV m)/N for the araldite matrix and from 114 to 54.7 (mV m)/N for the PU matrix. These estimates are comparable with the experimental values of g_h^* for various 0–3 composites of the $PbTiO_3$ ceramics–polymer type ($g_h^* = 47$–100 (mV m)/N [16]) and are much greater than $g_h^* = 8$ (mV m)/N reported for the PZT ceramics–PU composite [16].

In conclusion, we have established that the nontrivial behavior of piezoelectric coefficients of the 0–3 composites based on modified $PbTiO_3$ ceramics is related to the unusual sign of the $e_{3j}^{(FC)}$ coefficient ($e_{3j}^{(FC)} > 0$, see relation (2)), the influence of the elastic properties of a piezopassive polymer matrix, and a difference in the anisotropy factors e_{33}^*/e_{31}^* and d_{33}^*/d_{31}^* for elongated FC inclusions. The obtained results may favor the creation of new piezoelectric materials combining the advantages of anisotropic FC components with a regular microstructure of polymer matrices and the features of electromechanical interactions of FC inclusions.

Acknowledgments. The authors are grateful to Prof. A.V. Turik (Russia) and to Dr. M. Kamlah and Dr. Ch. Poizat (Germany) for their interest in the subject under investigation.

This study was supported in part by the Ministry of Education of the Russian Federation, project no. A03-2.9-413.

REFERENCES

1. R. E. Newnham, MRS Bull. **22** (5), 20 (1997).
2. T. Furukawa, K. Ishida, and E. Fukada, J. Appl. Phys. **50**, 4904 (1979).
3. L. P. Khoroshun, B. P. Masov, and P. V. Leshchenko, *Prediction of the Effective Properties of Piezoactive Composite Materials* (Naukova Dumka, Kiev, 1989) [in Russian].
4. H. L. W. Chan, P. K. L. Ng, and C. L. Choy, Appl. Phys. Lett. **74**, 3029 (1999).
5. F. Levassort, M. Lethiecq, C. Millar, and L. Pourcelot, IEEE Trans. Ultrason. Ferroelectr. Freq. Control **45**, 1497 (1998).
6. V. M. Levin, M. I. Rakovskaja, and W. S. Kreher, Int. J. Solids Struct. **36**, 2683 (1999); Int. J. Solids Struct. **37**, 7821(E) (2000).
7. C. R. Bowen and V. Yu. Topolov, Acta Mater. **51**, 4965 (2003).
8. Ch. Poizat and M. Sester, Comput. Mater. Sci. **16**, 89 (1999).
9. S. Ikegami, I. Ueda, and T. Nagata, J. Acoust. Soc. Am. **50**, Part 1, 1060 (1971).
10. K. Nagatsuma, Y. Ito, S. Jyomura, H. Takeuchi, and S. Ashida, *Piezoelectricity*, Ed. by G. W. Taylor, J. J. Gagnepain, T. R. Meeker, *et al.* (Gordon and Breach, New York, 1985), pp. 167–176.
11. B. Jiang, D.-N. Fang, and K.-C. Hwang, Int. J. Solids Struct. **36**, 2707 (1999).
12. V. Yu. Topolov and A. V. Turik, Zh. Tekh. Fiz. **71** (9), 26 (2001) [Tech. Phys. **46**, 1093 (2001)].
13. J. B. Ngoma, J. Y. Cavaille, J. Paletto, and J. Perez, Ferroelectrics **109**, 205 (1990).
14. C. J. Dias and D. K. Gas-Gupta, in *Proceedings of the 4th International Conference on Properties and Applications of Dielectric Materials, Brisbane, 1994* (IEEE, Brisbane, 1994), pp. 175–178.
15. G. A. Lushcheĭkin, Izv. Akad. Nauk SSSR, Ser. Fiz. **51**, 2273 (1987).
16. R. C. Pohanka and P. L. Smith, *Electronic Ceramics. Properties, Devices, and Applications*, Ed. by L. M. Levinson (Dekker, New York, 1988), pp. 45–145.

Translated by P. Pozdeev

Technical Physics Letters, Vol. 30, No. 10, 2004, pp. 877–879. Translated from Pis'ma v Zhurnal Tekhnicheskoĭ Fiziki, Vol. 30, No. 20, 2004, pp. 77–83.

Dynamics of the Oriented Interaction of Accelerated Particles with Nonchiral Carbon Nanotubes

S. I. Matyukhin[a,*] and S. Yu. Grishina[b]

[a] *Orel State Technical University, Orel, Russia*

[b] *Orel State Agricultural University, Orel, Russia*

* *e-mail: sim1@mail.ru*

Received February 17, 2004; in final form, May 21, 2004

Abstract—Dynamics of the oriented interaction of accelerated particles with nonchiral carbon nanotubes has been theoretically studied in terms of a continuous potential well known in the theory of channeling. The conditions of applicability of the adopted approximation are considered. Numerical solutions of the equations of motion of heavy particles inside carbon nanotubes with allowance for the electron drag are obtained and analyzed. © *2004 MAIK "Nauka/Interperiodica".*

As is known [1–3], particles penetrating into the cavities of fullerenes and nanotubes can significantly modify their mechanical, electromagnetic, and chemical properties. This circumstance opens wide prospects for using such carbon structures in applied chemistry, materials science, and nanoelectronics. However, the existing methods of doping fullerenes and nanotubes [1–3] are based mostly on the introduction of impurities from the vapor phase in the course of synthesis of carbon nanoparticles. Such techniques do not provide a sufficiently high production yield and cannot be implemented in flexible technologies, especially in those involving multistage processes. For this reason, the task of developing methods for the introduction of atoms, ions, and molecules into carbon nanostructures is the central R&D problem of nanotechnologies.

We believe [4–6] that a solution to this problem is provided by the well-known and thoroughly studied method of modification of the structure and properties of solids, which is based on the doping of materials by means of accelerated particle beams. This method of introducing impurity atoms, also widely known as ion implantation, has become the traditional and highly effective method of obtaining semiconductor structures with controlled properties and ensured rapid progress in the semiconductor electronics and microelectronics. The advantages of the ion beam technology include high product yield, local and exact character of ion implantation, and the possibility of introducing impurities of virtually any type in controlled amount. However, the use of ion implantation in nanotechnologies is still very restricted.

This paper presents the results of investigations [4–8] of the dynamics of the oriented interaction of accelerated particles with nonchiral (i.e., different from armchair and zig-zag configurations) carbon nanotubes (CNTs). The interaction is described in terms of a continuous potential well known in the theory of channeling [9, 10]. We will consider the conditions of applicability of the adopted approximation taking into account the electron drag and analyze the numerical solutions of the equations of motion of heavy particles inside CNTs.

The oriented interaction of accelerated particles with CNTs is characterized by the angle ψ between the particle velocity and the nanotube axis being smaller than a certain critical value ψ_c. For nonchiral CHTs and particles with the energy $E > 2\pi Z_1 Z_2 e^2/a_{TF}$, this critical angle is given by the formula

$$\psi_c \approx \sqrt{\frac{8\pi Z_1 Z_2 e^2 a_{TF}}{3\sqrt{3}a^2 E}}, \quad (1)$$

where $Z_1 e$ is the charge of atomic nuclei of the particles, $Z_2 e$ is the charge of the atomic nucleus of carbon ($Z_2 = 6$), a is the carbon–carbon bond length in CNTs ($a \approx 0.142$ nm), a_{TF} is the screening radius of the Thomas–Fermi interatomic potential [10, 11] defined as

$$a_{TF} \approx 0.885 a_B (Z_1^{1/2} + Z_2^{1/2})^{-2/3}, \quad (2)$$

and a_B is the Bohr radius. For example, for 5-keV protons, formula (1) yields $\psi_c \approx 5°$.

For $\psi < \psi_c$, the atomic particles exhibit collective correlated collisions with carbon atoms in CNT walls. This interaction can be described in terms of a continuous potential well known in the theory of channeling [9, 10]. For a particle incorporated into a nonchiral CNT, this potential has the following form:

$$U(r, z) = \frac{4R}{3\sqrt{3}a^2} \times \int_0^{2\pi}\int_0^{L} V\left(\sqrt{r^2 + R^2 - 2rR\cos\varphi + (z - z')^2}\right) d\varphi dz', \quad (3)$$

1063-7850/04/3010-0877$26.00 © 2004 MAIK "Nauka/Interperiodica"

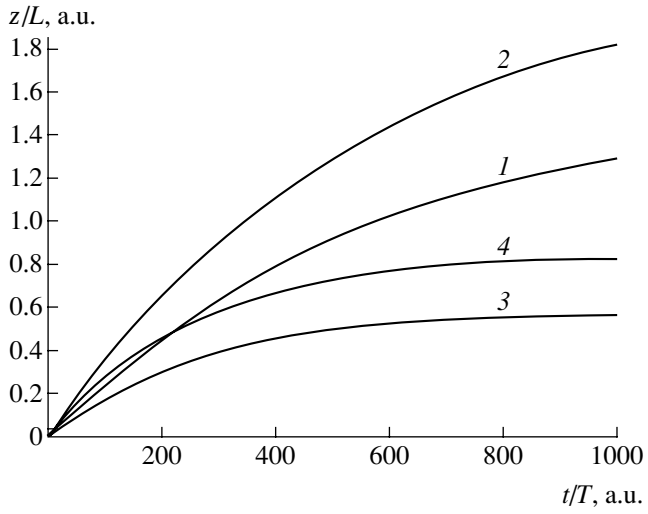

Fig. 1. Time variation of the penetration depth z for (*1*, *3*) 5-keV and (*2*, *4*) 10-keV protons implanted into a CNT with the chirality indices (11,9) at the initial radial coordinate $r_0 = 0.3R$ (*1*, *2*) and $0.7R$ (*3*, *4*).

where z is the depth of particle penetration; r is the distance from the CNT axis; R and L are the CNT radius and length, respectively; and $V(x)$ is the interatomic interaction potential.

Taking into account that the screening radius of the Thomas–Fermi interatomic potential [10, 11] is much smaller than the CNT length, $a_{TF} \ll L$, we may ignore the edge effects in expression (3). Moreover, since $a_{TF} < a \ll R$, we may describe the interaction of particles with CNT walls, neglecting the wall curvature. Thus, a particle moving inside a CNT can be considered [7, 8] as moving between two parallel atomic planes spaced by $r = R$ from the CNT axis. Then, the interaction potential (3) will coincide with the atomic plane potential

$$U(r) \approx \frac{4}{3\sqrt{3}a^2}\int_0^\infty V(\sqrt{(R-r)^2+\rho^2})\rho\,d\rho. \qquad (4)$$

In particular, for the Lindhard interatomic potential [9–11], we obtain

$$U(r) \approx \frac{8\pi Z_1 Z_2 e^2}{3\sqrt{3}a^2}(\sqrt{(R-r)^2+3a_{TF}^2}-(R-r)). \qquad (5)$$

The oriented motion of particles in the potential field (4) can be considered as proceeding in the channeling regime [9, 10]. This motion is characterized by strongly suppressed short-range collisions of particles with carbon atoms, so that the extent of the particle-induced CNT fracture is also significantly reduced.

For the introduction of particles into the internal cavities of CNTs, it is necessary to provide for their penetration through a potential barrier with a height not exceeding 100 eV (for protons, on the order of 16 eV) [7, 8]. For such energies, the de Broglie wavelength of a heavy particle with the mass $m \gg m_e$ (m_e is the electron mass) is much shorter than the CNT dimensions (for protons, this wavelength is on the order of 10^{-2} nm). Therefore, the oriented motion of particles inside CNTs can be described using the laws of classical mechanics. It is evident a priori that particles moving in a CNT will perform decaying radial oscillations with the period

$$T \approx \sqrt{2m}\int_{r_{min}}^{r_{max}}\left[E_0\psi_0^2 + U(r_0) - U(r) - \frac{M_0^2}{2mr^2}\right]^{-1/2} dr. \qquad (6)$$

Here, E_0 is the initial particle energy, ψ_0 is the initial angle of the particle velocity relative to the nanotube axis (entrance angle), M_0 is the initial momentum moment (angular moment) with respect to the axis, r_0 is the radial coordinate of the point of entrance into the nanotube, and r_{min} and r_{max} are the roots of the equation

$$E_0\psi_0^2 + U(r_0) - U(r) - \frac{M_0^2}{2mr^2} = 0 \qquad (7)$$

(the r_{min} and r_{max} values have the meaning of the minimum and maximum deviations of the particle from the axis; for $M_0 = 0$, we have $r_{min} = 0$).

Particles moving inside CNTs exhibit drag as a result of their interaction with electrons of carbon atoms in the CNT walls. The intensity of this scattering is determined by the local electron density and can be calculated [10] using the Bethe–Bloch or Lindhard theory, depending on the particle energy. The energy of the transverse motion of particles relative to the axis and the angular momentum relative to this axis in nonchiral nanotubes are adiabatic invariants.

Figures 1 and 2 show the results of solution of the equations of motion obtained by numerical methods for protons of various energies with allowance of energy losses related to the aforementioned electron drag. The calculations were performed for nonchiral CNTs with $L = 50$ μm and $R = 0.679$ nm. The curves refer to the cases when the entrance angle is $\psi_0 = 0$ and the initial radial coordinate is $r_0 = 0.3R$ (curves *1* and *2*) and $0.7R$ (curves *3* and *4*). The period of oscillations (6) of such particles inside the nanotube is on the order of 10^{-4} ns, which is approximately 400 times as small as the characteristic flight time L/v_0 (v_0 is the initial particle velocity). The interaction of particles with CNT walls was described using the continuous atomic plane potential determined by relations (5) and (2).

As can be seen from the results of numerical analysis (Figs. 1 and 2), channeling of the positive atomic particles with velocities $v < v_B Z_{1,2}^{2/3}$ (keV-energy

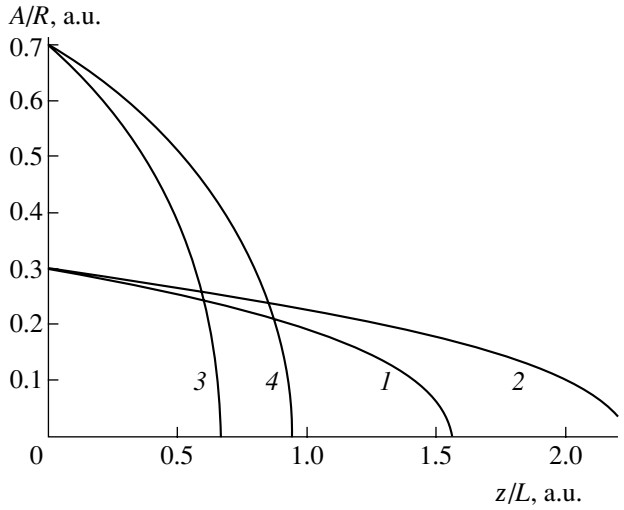

Fig. 2. Plots of the amplitude A of radial oscillations versus penetration depth z for (*1*, *3*) 5-keV and (*2*, *4*) 10-keV protons implanted into a CNT with the chirality indices (11,9) at the initial radial coordinate $r_0 = 0.3R$ (*1*, *2*) and $0.7R$ (*3*, *4*).

beams), where v_B is the Bohr velocity, can occur in a regime of stopping, whereby these particles lose energy as a result of the electron drag more rapidly than fly through the nanotube. Thus, by varying the primary beam energy, it is possible [4–6] to provide for the optimum conditions of ion implantation into carbon nanostructures. This circumstance opens wide possibilities for the use of ion beams in the commercial production of doped fullerenes and CNTs.

In practice, realization of the stopping regime depends on the relation between parameters such as the initial energy E_0, initial moment M_0 relative to the nanotube axis, coordinate r_0 of the point of particle entrance into the nanotube, and nanotube length L. At a given primary beam energy, the fraction of particles flying through the nanotube without stopping grows with decreasing L (Fig. 1). A decrease in the amplitude of transverse oscillations for such particles (Fig. 2) can be interpreted as focusing of the beam by nanotubes. The phenomenon of ion beam focusing by short nanotubes can find wide application in various ion beam technologies.

Acknowledgments. The work was supported by the Russian Foundation for Basic Research, project no. 03-03-96488.

REFERENCES

1. A. V. Eletskiĭ, Usp. Fiz. Nauk **170**, 113 (2000) [Phys. Usp. **43**, 111 (2000)].
2. *Molecular Nanostructures*, Ed. by H. Kuzmany, J. Fink, M. Mehring, and S. Roth (World Scientific, Singapore, 1998).
3. *Science and Application of Nanotubes*, Ed. by D. Tomanek and R. J. Enbody (New York, 2000).
4. V. V. Rozhkov and S. I. Matyukhin, in *Proceedings of the 15th International Conference on Physics of Radiation Phenomena and Related Materials Science, Kharkov, 2002*, p. 277.
5. S. I. Matyukhin, in *Proceedings of the 1st All-Russia Conference on Physicochemical Processes in Condensed State and Interphase Boundaries, Voronezh, 2002*, p. 217.
6. S. I. Matyukhin, in *Proceedings of the International Conference on Chemistry of Solid and Modern Micro- and Nanotechnology, Stavropol, 2002*, p. 77.
7. S. I. Matyukhin and S. Yu. Grishina, in *Proceedings of the 15th All-Russia Symposium on Modern Chemical Physics, Moscow, 2003*, p. 71.
8. S. I. Matyukhin and S. Yu. Grishina, in *Proceedings of the 12th International Conference on Radiation Physics and Chemistry of Inorganic Materials, Tomsk, 2003*, p. 344.
9. J. Lindhard, Mat. Fys. Medd. Dan. Vid. Selsk. **34** (14), 49 (1965).
10. Y.-H. Ohtsuki, *Charged Beam Interaction with Solids* (Taylor and Francis, London, 1983).
11. G. V. Dedkov, Usp. Fiz. Nauk **165**, 919 (1995) [Phys. Usp. **38**, 877 (1995)].

Translated by P. Pozdeev

Technical Physics Letters, Vol. 30, No. 10, 2004, pp. 880–882. Translated from Pis'ma v Zhurnal Tekhnicheskoĭ Fiziki, Vol. 30, No. 20, 2004, pp. 84–89.

Ion Defect Transport via Chains of Water Molecules in Copper Sulfate Hydrate

B. M. Gorelov and K. P. Konin

Institute of Surface Chemistry, National Academy of Sciences of Ukraine, Kiev, Ukraine

e-mail: user@surfchem.freenet.kiev.ua

Received March 2, 2004; in final form, May 21, 2004

Abstract—Crystalline copper sulfate hydrate $CuSO_4 \cdot 5H_2O$ exhibits microwave absorption related to the transport of ion defects via the chains of water molecules in the crystal lattice. The chains consist of H_2O molecules localized at two nonequivalent interstitial sites near Cu atoms. These chains account for two absorption bands, which are related to the transfer of ion defects of different types. © *2004 MAIK "Nauka/Interperiodica".*

As is known [1], the chains of water molecules linked by hydrogen bonds (Bernal–Fowler filaments) are capable of transporting protons in the form of ion defects of the H^+ (H_3O^+) and OH^- types. Molecular filaments stable with respect to temperature can form in aqueous systems at the surface of solids or in ice crystals. The conductivity of such filaments is determined by their structural perfection and the probability for charge carriers to occur at the chain ends. It is natural to assume that H_2O molecules are also capable of forming stable filaments in the crystal structures of other solids. In particular, conducting chains in crystalline copper sulfate hydrate $CuSO_4 \cdot 5H_2O$ can be formed by H_2O molecules localized near Cu atoms and bound by hydrogen bonds to the atomic environment [2]. Localization near the cations may favor the dissociation of molecules [1], thus leading to the appearance of charge carriers at the chain ends and stimulating conductivity via such filaments.

This paper presents the results of investigations of the transfer of ion defects via chains of water molecules in crystalline copper sulfate hydrate $CuSO_4 \cdot 5H_2O$ in a microwave field.

The experiments were performed on powdered crystalline samples with an average particle size of ~10 μm and a powder density of 1.1–1.3 g/cm^3. The samples were studied before and after destruction of the conducting chains by thermal or radiation (room-temperature exposure to γ radiation of a ^{60}Co source) treatment. The microwave conductivity and reflection coefficient were measured in an 8–12 GHz frequency range by the short-circuited line method using a Ya2R-67 indicator.

The microwave conductivity σ of the initial $CuSO_4 \cdot 5H_2O$ samples exhibits a sharp increase at temperatures $T \geq 25$°C (Fig. 1). For $T \geq 50$°C, the behavior of $\sigma(T)$ can be described by the exponent $\sigma(T) = C\exp(-E/kT)$, where k is the Boltzmann constant, $C = 6.0 \times 10^5$ $(\Omega\ \text{cm})^{-1}$, and $E = 0.65$ eV. The crystal lattice of $CuSO_4 \cdot 5H_2O$ contains three bound states of water molecules, which can be removed by heating the samples to ~95, 110, and 240°C. In the first two states (each with a concentration of $\sim 5.5 \times 10^{21}$ cm^{-3}), water molecules are localized near Cu(0, 0, 0) and Cu (1/2, 1/2, 0) atoms, while in the third state they occur near O atoms of the SO_4 group [2].

The removal of water molecules from the first bound state does not influence the behavior of $\sigma(T)$ as long as the number of these molecules is $n \geq 2.3 \times 10^{21}$ cm^{-3} (Fig. 1, curve *2*). As the number of removed molecules increases, $\sigma(n, T)$ exhibits a sharp drop. The magnitude of this jump decreases with decreasing T. At $n < 2.3 \times 10^{21}$ cm^{-3}, the value of $\sigma(T)$ ceases to depend on the temperature, although H_2O molecules in the crystal lattice still occur in the three bound states (see curve *1* in the inset in Fig. 1). Only simultaneous removal of H_2O molecules from the first two bound states on heating the sample to 115°C leads to a decrease both in $\sigma(n, T)$ and in the jump magnitude (see curve *2* in the inset in Fig. 1). When the concentration of water molecules in the two states is 4.5×10^{21} cm^{-3}, the behavior of $\sigma(T)$ is described by the exponential law with $C = 2.2 \times 10^4$ $(\Omega\ \text{cm})^{-1}$, and $E = 0.04$ eV (Fig. 1, curve *3*). After the removal of water by annealing from the first and second bound states, σ of the resulting $CuSO_4 \cdot 3H_2O$ and $CuSO_4 \cdot H_2O$ hydrates is independent of the temperature (Fig. 1, curves *4* and *5*).

Thus, water molecules stimulate a sharp increase in the conductivity when they occupy two nonequivalent interstitial sites near Cu atoms and are present in a concentration of not less than $(2.3–3.5) \times 10^{21}$ cm^{-3}. The observed jumplike change and sharp growth of $\sigma(n, T)$ indicate that microwave absorption is not related to transitions in the H_2O, H_3O^+, or OH^- dipoles. Indeed, in

the case of dipole transitions, the conductivity is described by the formula

$$\sigma(\omega) = \frac{n\mathbf{D}^2}{3kT}\frac{1}{1+\exp(W/kT)}\frac{\omega^2\tau}{1+\omega^2\tau^2}, \quad (1)$$

where n is the concentration of dipoles, $\mathbf{D}$ is the dipole moment, W is the dipole transition energy, and τ is the relaxation time [3]. This value is proportional to $\mathbf{uD}^2$ and remains virtually constant in the temperature interval $20°C \le T \le 120°C$. The dipole absorption probably determines the constant level of $\sigma(n, T)$ attained after the annealing of water from bound states.

When H_2O molecules fill the aforementioned interstitials of two types, sharp growth of $\sigma(n, T)$ takes place, provided that the number of these molecules in these sites is sufficient to create continuous chains in the crystal structure (at a lattice parameter of $CuSO_4 \cdot 5H_2O$ equal to 6–10 Å [2]). The proton transport appears for $T \ge 25°C$, which can be related to the onset of dissociation of water molecules in the Coulomb field of Cu^{2+} cations according to the reactions

$$H_2O \longleftrightarrow H^+ + OH^- \quad \text{or} \quad 2H_2O \longleftrightarrow H_3O^+ + OH^- \quad (2)$$

and the formation of ion defects of two types at the chain ends. The conducting filaments are composed of molecules in two states localized near Cu atoms. Apparently, the chains involve some molecules in the first bound state, since σ does not change when n varies above 2.3×10^{21} cm^{-3}. It is simultaneous thermal removal of H_2O molecules from both bound states that leads to a decrease in $\sigma(n, T)$, probably as a result of chain breakage and decrease in the number of the conducting filaments.

The breakage of conducting filaments can also take place under the action of γ radiation. As is known [4], hydrated salts are stable with respect to decomposition under irradiation to a dose of $D \le 1.5$ MGy. The irradiation to small doses $D \le 150$ kGy, while not destroying the hydrate crystal lattice, stimulates the hydrolysis of crystallization water according to the reactions [5]

$$2H_2O^- \longrightarrow H_2 + 2OH^-, \quad (3)$$

$$2H_2O^+ \longrightarrow O_2 + 2H^+ + H_2 \quad (4)$$

with the formation of chain breaks and one defect (H^+ or OH^-) at the filament end.

Irradiation leads to a decrease in the microwave absorption and is analogous in this respect to the effect of thermal removal of H_2O molecules simultaneously from the first two bound states (Fig. 2). The samples of $CuSO_4 \cdot 5H_2O$ before irradiation and after exposure to a dose within 0.1–1 kGy exhibit a single absorption band with a maximum at $\omega = 10$ GHz (Fig. 2, curves *1* and *2*). In the dose range 10–50 kGy, there appear two resolved peaks separated by $\hbar\omega \approx 1 \times 10^{-6}$ eV. These peaks are observed at room temperature and grow in intensity with temperature (Fig. 2, curves *3* and *4*). The behavior of $\sigma(T) = C\exp(-E/kT)$ measured at the frequencies 9.5 and 11 GHz is described by the parameters $C = 4.1 \times 10^{-3}$ and 3.7×10^{-2} $(\Omega\,\text{cm})^{-1}$ and $E = 0.16$ and 0.09 eV, respectively. An increase in the radiation dose up to 150 kGy suppresses the microwave absorption and the growth of σ with temperature, which is evidence of the breakage of H_2O chains and the absence of proton transport (Fig. 2, curve *5*).

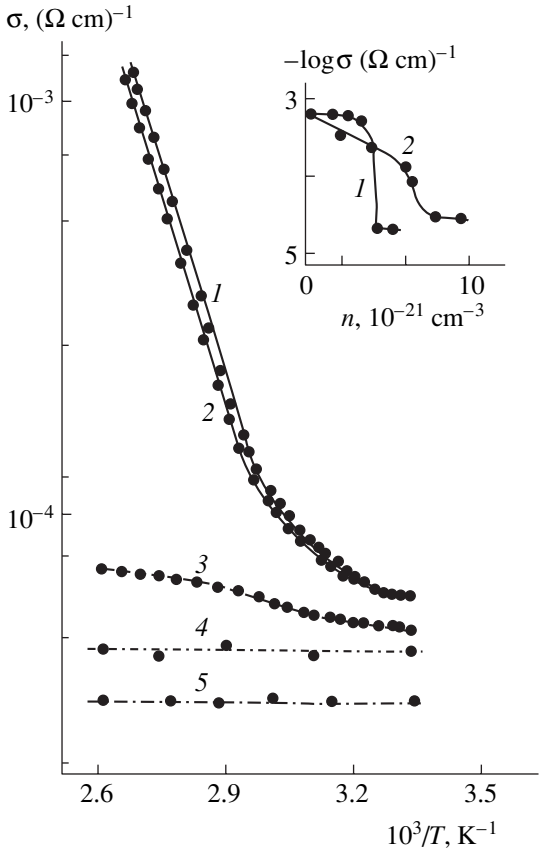

Fig. 1. Temperature dependences of the conductivity of crystalline copper sulfate hydrate: (*1–3*) $CuSO_4 \cdot 5H_2O$ before and after the thermal removal of (*1*) 8×10^{20} cm^{-3} and (*2*) 2.3×10^{21} cm^{-3} of H_2O molecules from the first bound state and (*3*) 6.5×10^{21} cm^{-3} of H_2O molecules from the first two bound states; (*4*) $CuSO_4 \cdot 3H_2O$; (*5*) $CuSO_4 \cdot H_2O$. The inset shows plots of the conductivity σ at $T = 82°C$ versus number n of H_2O molecules removed by annealing from (*1*) the first and (*2*) the second bound states.

The appearance of two peaks in γ-irradiated samples can be related to the formation of one ion type (H^+ or OH^-) at the chain ends and the presence of two kinds of chains by which either a positive or negative charge is transferred. In the initial samples, the ion defects of both types are localized at the chain ends and the trans-

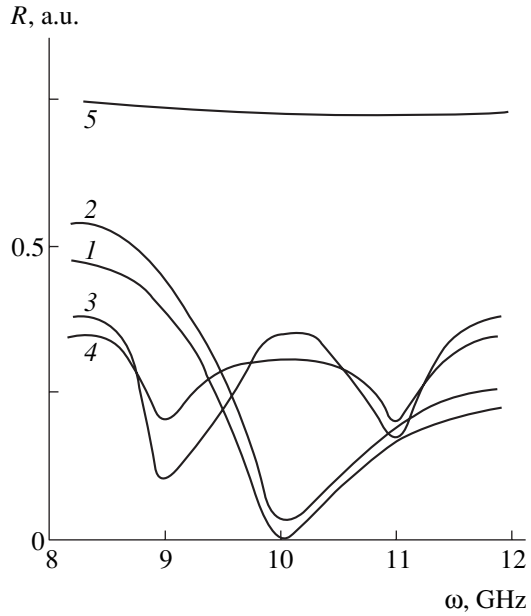

Fig. 2. Microwave reflection spectra of crystalline copper sulfate hydrate $CuSO_4 \cdot 5H_2O$ measured at 80°C after γ-irradiation to various doses (kGy): (*1*) 0.1; (*2*) 1; (*3*) 10; (*4*) 50; (*5*) 150.

port apparently involves only H^+ ions (possessing higher mobility) and only one kind of chains (transferring positive or negative charge).

The energy interval separating the absorption peaks is $\hbar\omega \ll kT$. Therefore, the energy differences due to various configurations of molecules in the chains and the width of the allowed energy band of protons involved in the transport are much smaller than kT. Thus, thermal oscillations of atoms and H_2O molecules in the crystal lattice apparently do not influence the energy spectrum of charge carriers in the conducting filaments. The growth of σ with temperature indicates that, in the interval of reversible variation of $\sigma(T)$, the chain structure is not broken when T increases. The increase in σ with the temperature may be related to the growing number of defects at the chain ends (due to increasing probability and yield of the dissociation reaction (2)) and the growing mobility of protons transported via the chain. According to the soliton model of proton transport via chains of stable configuration, the proton transfer rate is described by the relation

$$k_0 = \omega_0 \exp(-E_s/kT), \quad (5)$$

where ω_0 is a parameter dependent on the height of the intermolecular barrier and E_s is the soliton energy [1]. In this model, both the proton mobility and σ may increase with the temperature.

It should be noted that the observed behavior of $\sigma(T)$ can also be related to charge transfer via the Bjerrum orientation defects. This mechanism has an activation character and involves rotation of water molecules [1]. However, a relation of σ to migration of the orientation defects is unlikely, since rotations of water molecules in the crystal lattice of $CuSO_4 \cdot 5H_2O$ in the temperature interval 20–88°C are not observed [2].

In conclusion, the transport of ion defects via chains of water molecules in $CuSO_4 \cdot 5H_2O$ takes place provided that H_2O molecules in the crystal lattice of this hydrate occupy two nonequivalent interstitial sites near Cu atoms with a concentration of no less than 1.7×10^{21} cm^{-3} for each of the two bound states. The transport of ion defect increases with the temperature. The width of the energy spectrum of charges transferred via conducting filaments is apparently below 10^{-6} eV.

REFERENCES

1. V. Ya. Antonchenko, A. S. Davydov, and V. V. Il'in, *Foundations of Water Physics* (Naukova Dumka, Kiev, 1991) [in Russian].
2. G. E. Bacon and N. A. Curry, Proc. R. Soc. London, Ser. A **266** (1324), 95 (1962).
3. N. F. Mott and E. A. Davis, *Electronic Processes in Non-Crystalline Materials* (Clarendon Press, Oxford, 1971).
4. A. K. Pikaev, *Modern Radiation Chemistry. Solids and Polymers. Applied Aspects* (Nauka, Moscow, 1987) [in Russian].
5. E. J. Henley and E. R. Johnson, *The Chemistry and Physics of High Energy Reactions* (Washington Univ. Press, Washington, 1969).

Translated by P. Pozdeev

Technical Physics Letters, Vol. 30, No. 10, 2004, pp. 883–885. Translated from Pis'ma v Zhurnal Tekhnicheskoĭ Fiziki, Vol. 30, No. 20, 2004, pp. 90–95.

Use of a Ultrasonic Transducer Array for Measuring the Velocity and Attenuation of Leaky Acoustic Waves

S. A. Titov, R. G. Maev, and A. N. Bogachenkov

Emanuel Institute of Biochemical Physics, Russian Academy of Sciences, Moscow, 117977 Russia

e-mail: chembio@sky.chph.ras.ru

Received May 16, 2004

Abstract—We suggest a new method for measuring local values of the velocity and attenuation of leaky acoustic waves, which is based on wave field measurements using an immobile array of receiving ultrasonic transducers. In comparison to the methods using a single focused transducer mechanically scanned over a given region of the sample, the proposed technique is advantageous in having a higher operation speed due to the electronic switching of receiving channels in the array and in requiring no high-precision mechanical scanners. A ray model of the proposed measuring system comprising an array of ultrasonic transducers with an electronic scanning facility is described. Theoretical conclusions have been experimentally confirmed by tests on the samples with known properties. © *2004 MAIK "Nauka/Interperiodica".*

The existing ultrasonic systems of the immersion type intended for measuring the local values of elastic parameters of a probed object are based on the processing of spatiotemporal response signals obtained in the course of mechanical scanning of one or several focused transducers relative to the object. In quantitative acoustic microscopy, the most widely used method consists in moving a single focused transducer along the normal to the sample surface [1]. Recently, we have proposed and developed a scheme of measurements employing transmitting and receiving transducers focused into the sample plane, whereby the response signal is measured by moving the receiving transducer parallel to this plane [2, 3]. By processing the response signal measured in such a system in the spatiotemporal or spectral domain, it is possible to reconstruct the reflectance function of the incident ultrasonic wave as a function of the angle of incidence on the immersion liquid–sample interface and to determine local values of the phase velocity and attenuation coefficient of leaky acoustic waves such as the Rayleigh waves, Lamb waves, and skimming shear waves.

The common disadvantages of such measuring systems, related to the need in ensuring mechanical motion of the transducers, are manifested by a low speed of measurements and their relatively low accuracy limited by the mechanical devices. In this letter, we suggest a new ultrasonic immersion measuring system, in which the acoustic field of leaky waves is detected by an immobile array of ultrasonic transducers and the spatiotemporal response signal is formed by means of electronic switching of the receiving channels.

The proposed method of measurements can be described in terms of the ray model schematically depicted in Fig. 1. Consider an leaky acoustic wave excited by a transducer situated to the left on point B_1. The wave propagates along the surface of sample *1* by leaky (being reemitted) into the immersion liquid *2*, and is detected by a one-dimensional array of transducers *3* arranged with a spatial period $O_1O_2 = p$ on a line making an angle θ_0 with the sample plane. Let us determine the relative delay time Δt and the ratio of amplitude for the responses from two neighboring elements of the array positioned at the points O_1 and O_2. These response signals are excited by the acoustic rays B_1O_1 and B_2O_2 propagating at a critical angle θ_R.

Let us draw the line O_1E perpendicular to the B_2O_2 segment. Since the time required for the leaky wave to

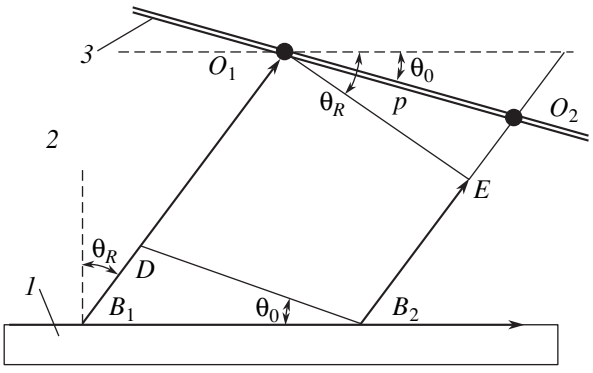

Fig. 1. Schematic diagram illustrating the ray model of the ultrasonic measuring system with a receiving transducer array (see the text for explanations).

1063-7850/04/3010-0883$26.00 © 2004 MAIK "Nauka/Interperiodica"

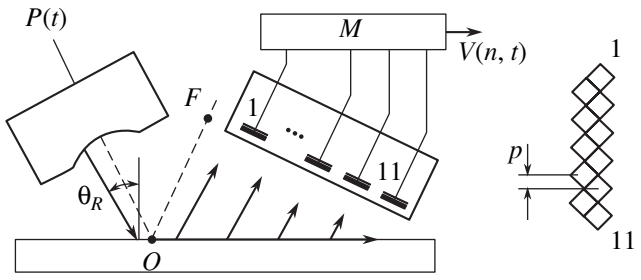

Fig. 2. Schematic diagram of the experimental ultrasonic measuring system comprising an array of receiving transducers with an electronic scanning facility (see the text for explanations).

reach the points O_1 and E is the same, the second response will be delayed relative to the first one by the time required for the wave to travel the EO_2 segment:

$$\Delta t = \frac{EO_2}{C} = \frac{p}{C}\sin(\theta_R - \vartheta_0), \quad (1)$$

where C is the wave velocity in the immersion liquid. By measuring the delay Δt between responses arriving at the neighboring elements of the array, one can determine the critical angle θ_R of the leaky wave and, hence, the wave velocity

$$C_R = \frac{C}{\sin\theta_R}. \quad (2)$$

The ratio of amplitudes A_2/A_1 of the harmonic responses in the neighboring elements is determined by the coefficients of attenuation of sound (α_w) and the leaky wave (α) in the immersion liquid:

$$\eta = \frac{A_2}{A_1} = \frac{\exp(-\alpha B_1B_2 - \alpha_w B_2O_2)}{\exp(-\alpha_w B_1O_1)}. \quad (3)$$

For the B_2D line parallel to O_1O_2 (Fig. 1), $B_1O_1 - B_2O_2 = B_1D$. The law of sines for the B_1B_2D triangle yields

$$\frac{B_1B_2}{\sin(\pi/2 - (\theta_0 - \theta_R))} = \frac{B_1D}{\sin\theta_0} = \frac{p}{\sin(\pi/2 - \theta_R)}. \quad (4)$$

Using this relation, we eventually obtain the following expression for the ratio of response amplitudes:

$$\eta = \exp\left\{(-\alpha\cos(\theta_0 - \theta_R) + \alpha_w\sin\theta_0)\frac{p}{\cos\theta_R}\right\}. \quad (5)$$

Thus, by measuring the ratio η and the critical angle θ_R and using the coefficient of sound attenuation α_w in the immersion liquid, we can determine the coefficient of attenuation α for the leaky wave.

Figure 2 shows a schematic diagram of the experimental system implementing the proposed principle. The probing ultrasonic wave is generated in the immersion liquid (water) by a focused transducer of the IS-HR-1/4-20 type (XACTEC Inc., USA) with a central frequency of 20 MHz, an aperture diameter of 6 mm, and a focal distance of 19 mm. The receiving array comprised 11 identical square transducers with a side length of 1.25 mm, arranged as depicted in the right-hand inset. This arrangement of elements in the array corresponded to a spatial period of $p = 0.884$ mm in the direction of detection of the leaky wave. The transducers were made of PZT-5 piezoelectric ceramics plates with a thickness corresponding to a central frequency of 20 MHz. The external surface of these piezoelements, covered by a common thin-film grounded electrode, occurred in direct contact with water, while the internal sides were connected to a matched acoustic attenuator so as to provide for a wide working band.

The focused transducer and the array were inclined at $\theta_0 = 27.0°$ relative to the vertical axis. The distances between the transducer, the array, and the sample were such that the mirror image of the focus F occurred in the immersion liquid to the left of the array (as depicted in Fig. 2). The ray OF (mirror reflected from the sample surface) bypassed the receiving elements, and the output signal taken from the array was determined entirely by responses due to the leaky wave.

The transmitting transducer was excited by single pulses $P(t)$ with an amplitude of about 150 V and a pulse width of 30 ns. The elements of the receiving array were sequentially connected via a multiplexer (M) to the input of a wideband (1–30 MHz) amplifier of a standard ultrasonic system. The time of acquisition of the complete data set $V(n, t)$ (where n = 1–11 is the channel number) did not exceed 100 ms.

In order to determine the velocity of the leaky wave, we measured the delay times of pulses detected in each channel and calculated the average Δt value. For determining the coefficient of attenuation of the leaky wave,

Comparison of the velocity and the attenuation coefficient of the leaky acoustic wave determined using the echo pulse technique (C_R^*, α^*) and the proposed transducer array (C_R, α)

Material	V_L, m/s	V_S, m/s	C_R^*, m/s	α^*, 1/mm (4 MHz)	C_R, m/s	α, 1/mm (4 MHz)
Fused quartz	5959	3767	3426	0.28	3430	0.30
Aluminum alloy	6393	3163	2960	0.24	2973	0.28

we performed spectral analysis of all responses $V(n, t)$ and calculated the average ratio η of amplitudes of the responses from neighboring elements at a certain frequency. Using these values, the wave velocity C_R and the attenuation coefficient of the leaky wave were calculated using formulas (1), (2), and (5).

For experimental verification of the proposed method, we have studied a series of materials with known acoustic properties determined by independent methods. The results of these tests are illustrated in the table by data for plane-parallel plates of fused quartz and an aluminum alloy. The velocities of longitudinal (V_L) and shear (V_S) were independently determined by the echo pulse technique [4] using V205 and V156 transducers (Panametrics, USA). Using these values of V_L and V_S and the known material density, we determined the poles of the coefficient of the plane wave reflection from the immersion liquid–sample interface and then calculated the velocity C_R^* and the attenuation coefficient α^* of the leaky Rayleigh wave using the real and imaginary parts of these poles [3]. A comparison of these values to the wave velocity C_R and the attenuation coefficient α measured using the above-described prototype system comprising an ultrasonic transducer array with an electronic scanning facility shows a quite satisfactory agreement, which can be considered as experimental verification of the proposed method.

REFERENCES

1. A. Briggs, *Acoustic Microscopy* (Clarendon Press, Oxford, 1992).
2. S. A. Titov, R. G. Maev, and A. N. Bogachenkov, Pis'ma Zh. Tekh. Fiz. **27** (4), 19 (2001) [Tech. Phys. Lett. **27**, 141 (2001)].
3. S. A. Titov, R. G. Maev, and A. N. Bogachenkov, IEEE Trans. Ultrason. Ferroelectr. Freq. Control **50**, 1046 (2003).
4. R. Truell, C. Elbaum, and B. B. Chick, *Ultrasonic Methods in Solid State Physics* (Academic Press, New York, 1969; Mir, Moscow, 1972).

Translated by P. Pozdeev